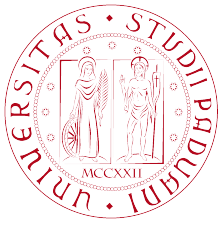

UNIVERSITÀ
DEGLI STUDI
DI PADOVA

Sede Amministrativa: Università degli Studi di Padova

Dipartimento di Ingegneria Idraulica, Marittima, Ambientale e Geotecnica

SCUOLA DI DOTTORATO DI RICERCA IN
SCIENZE DELL'INGEGNERIA CIVILE ED AMBIENTALE
CICLO XXIV

ON SOME ECOHYDROLOGICAL INTERACTIONS IN COASTAL ENVIRONMENTS

Direttore della Scuola: Prof. Stefano Lanzoni

Supervisore: Prof. Marco Marani

Dottoranda: Valeria Volpe

Ai miei genitori

Sí come il mangiare senza voglia fia dannoso alla salute,
cosí lo studio sanza desiderio guasta la memoria
e no' ritien cosa ch'ella pigli.
Leonardo Da Vinci

Abstract

The modeling of coupled processes of plant transpiration and photosynthesis together with soil moisture dynamics and morphology evolution is of key importance to study the fate of coastal areas, characterized by shallow waters and complex hydraulic regimes which regulate the sediment budget and salinity.

In this study, a novel approach to physically-based models which deal with water potential gradients is presented, based on plant stomatal optimization which aims to increase photosynthesis and minimize transpiration, for a cost parameter which depends on the local soil moisture. Such an approach allows to model hydraulic lift - that is water redistribution exerted by roots from wet to dry soil zones. Future possible scenarios of climate change, with increased values of ambient CO_2 concentration and air temperature, are explored in order to investigate the effects on plant adaptation.

Being salinity a stress factor in coastal areas, inhibiting photosynthesis both in salt-tolerant and salt-sensitive plants, a small-scale model for stomatal conductance is proposed. The optimality model here is revised to include the mesophyll conductance and its dependence on water salinity. The optimization problem of adjusting stomatal aperture for maximizing carbon gain at a given water loss is solved for both a non-linear and a linear biochemical demand function. The approaches here successfully describe gas-exchange measurements reported for olive trees (*Olea europea* L.) and spinach (*Spinacia oleracea* L.) in fresh water and in salt stressed conditions. From the results obtained, the photosynthetic capacity of the plant is directly reduced by $30 - 40\%$ under salt stress conditions. Hence, reductions in photosynthetic rates observed under increased salt stress are not only due to a limitation of CO_2 diffusion, but also caused by a direct salinity effect on the metabolic apparatus of the plant. An increase in salt stress causes also an increase in the cost of water parameter (or marginal water use efficiency)

exceeding 100%.

At a large scale, the effect of vegetation on sediment resuspension has been studied with application to coastal shallow waters by use of remote sensing and mathematical modeling in order to retrieve suspended sediment concentration maps. A simplified radiative transfer model has been applied to retrieve information from multispectral data from different sensors (LANDSAT, ASTER and ALOS AVNIR). Both the radiative transfer and the sediment transport models have been calibrated and validated with observations from a network of turbidity sensors in the Venice lagoon and the comparison of the suspended particulate matter (SPM) maps produced by satellite images and modelling allows to identify the magnitude of the stabilizing effect of benthic vegetation.

Sommario

La modellazione dei processi accoppiati di traspirazione e fotosintesi da parte delle piante con le dinamiche di umidità nel suolo e l'evoluzione morfologica è di grande importanza per lo studio dell'evoluzione degli ambienti costieri, caratterizzati da acque basse e regimi idraulici complessi che regolano il bilancio dei sedimenti e la salinità.

In questo lavoro viene presentato un approccio originale nell'ambito dei modelli che riguardano i potenziali idrici. Tale approccio è basato sull'ottimizzazione dell'apertura degli stomi da parte della pianta, che tende a massimizzare la fotosintesi e minimizzare la traspirazione, dato un parametro di costo che dipende dall'umidità de suolo locale. Tale approccio permette di descrivere l'*hydraulic lift*, ovvero la ridistribuzione di acqua da zone umide a zone più secche del suolo, esercitata da parte delle radici. Vengono inoltre esplorati futuri scenari di cambiamenti climatici, simulando aumenti della concentrazione di CO_2 in atmosfera e della temperatura dell'aria, per studiarne gli effetti sull'adattamento delle piante.

La salinità rappresenta un fattore di stress nelle aree costiere, inibendo la fotosintesi sia per le piante tolleranti al sale che per quelle sensibili. E' stato, quindi, sviluppato un modello a piccola scala per la conduttanza degli stomi. Il modello di ottimizzazione, ovvero l'adattamento dell'apertura degli stomi per massimizzare la fotosintesi per una fissata traspirazione, viene qui rivisitato al fine di includere la conduttanza dei mesofilli e la sua dipendenza dalla salinità nella rappresentazione del modello. Il problema di ottimizzazione è risolto sia per una domanda biochimica di ossigeno non lineare che per una lineare. Entrambi gli approcci riproducono alcune misure riportate in letteratura per ulivi (*Olea europea* L.) e spinaci (*Spinacia oleracea* L.), per condizioni di acqua d'irrigazione dolce o salata. Dai risultati ottenuti, risulta che la capacità fotosintetica della pianta è ridotta del $30 - 40\%$ in condizioni saline. Ne risulta che le riduzioni del tasso di fotosintesi che si

osservano in condizioni saline non sono dovute solamente ad una limitazione nella diffusione di CO_2, ma sono causate anche da un effetto diretto che la salinità stessa ha sull'apparato metabolico della pianta. Un aumento dello stress salino causa anche un aumento del parametro di costo dell'acqua (o efficienza di uso dell'acqua marginale) che eccede il 100%.

A grande scala, l'effetto della vegetazione sulla risospensione dei sedimenti è stato studiato con applicazione alle acque basse costiere attraverso il telerilevamento e la modellazione matematica, al fine di creare delle mappe della concentrazione dei solidi sospesi. E' stato applicato un modello di trasferimento radiativo semplificato per estrarre informazione da immagini multispettrali acquisite da diversi sensori (LANDSAT, ASTER and ALOS AVNIR). Sia il modello di trasferimento radiativo che il modello di trasporto sono stati calibrati e validati sulla base di dati misurati da una rete di torbidimetri nella laguna di Venezia, e il confronto tra le mappe di sedimento in sospensione create dalle immagini satellitari e dal modello permette di valutare l'entità dell'effetto di stabilizzazione esercitato dalla vegetazione bentica.

Acknowledgements

First, I would like to thank my advisor Marco Marani, who introduced me to the world of research and has been able to guide me, supporting and pushing when necessary, and inspiring me with his experience, knowledge, and enthusiasm. I would like to thank Gaby Katul, it has been a pleasure and a honor for me to work with him, but even more to know him: he is a great person first than a great scientist and teacher. I thank all the people I have worked with, and who taught me a lot spending time with me: Sonia Silvestri, Luca Carniello, Stefano Manzoni, Andrea Defina, Andrea D'Alpaos. Thanks to Professor John Albertson for giving me the opportunity to spend a year at Duke University working in his lab and to meet a lot of great scientists and people. They are too many to be listed here, but I am sure they know how much they are important for me.

Thanks to all my PhD colleagues and office mates! And thanks to Professor Stefano Lanzoni for heading this PhD School and to all the professors who taught the classes.

Finally, I would like to thank all the Institutions which provided the data I used; data collection and archiving is a time consuming and very important work: the Consorzio Venezia Nuova, Servizio Ambiente for providing turbidity data and reports of MELa2 Projects, to the Center for Forecast of Tide Level and High Water, Comune di Venezia for providing water level data, Dr. Alberotanza and Dr. Zibordi for providing CIMEL data as a part of the NASA AERONET Project, ESA for providing some of the satellite images, Servizio Informativo, Magistrato alle Acque di Venezia for providing some satellite images as well. I would also like to thank Fondazione Ing. Aldo Gini for the scholarship and the Istituto Veneto di Scienze Lettere ed Arti for the Summer Schools organized in these years.

Grazie Antonio per aver vissuto tutto questo con me!

Contents

List of Figures

List of Tables

Introduction

The evolution of natural ecosystems as a whole, from mountain regions to coastal areas, is strongly influenced by plants, which adapt to and shape their environment. Plant carbon uptake and transpiration, which depends and feeds back on soil moisture dynamics, is a key link between plant physiology and hydrologic processes. Climate change will affect current ecosystems equilibria to a great degree, and a more comprehensive understanding of plant adaptations to different environmental conditions is important to evaluate the possible eco-hydrological consequences.

The present thesis is in particular concerned with coastal and intertidal areas and their morphological and eco-hydrological dynamics. Coastal areas are, in fact, particularly exposed to climate changes in the sea level, nutrient dynamics, sediment transport processes and other plant stress factors, such as salt intrusion and soil salinization. Within this broad framework, this thesis will present some eco-hydrological and eco-morphological aspects of coastal areas at different spatial scales.

The first part of the thesis concerns the development of a soil-plant-atmosphere continuum model which can express plant transpiration and carbon exchange as a function of water potentials in the soil, within the plant, and in the atmosphere. The explicit dependence of the model on water potentials make it suitable for addressing the role of root water redistribution in the soil (hydraulic lift) and salinity effects on root water uptake. The model formulation also lends itself to the exploration of the role of dif-

ferent root biomass distributions on plant carbon assimilation efficiency and transpiration. The root-water-uptake model, after validation with field data collected in the Duke Forest (Durham, NC), is used to study water redistribution processes in the root zone and to simulate climate change scenarios.

In Chapter 2 the effects of salt stress on plant transpiration and photosynthesis are investigated at the leaf scale. In particular, a model of stomatal and mesophyll responses to elevated salinity based on an optimization theory is developed. The model is used to interpret existing observations of salinity stress in different crops. The stomatal/mesophyll conductance model, which accounts for salinity effects at the leaf level, can be incorporated in the soil-plant-atmosphere continuum model described in the previous Chapter, yielding a comprehensive description of plant subjected to salt stress.

In the last Chapter suspended sediment concentration in shallow tidal areas is studied using remote sensing and hydrodynamic modelling. Suspended sediment is of course a key player in tidal bio-morphodynamics. On one hand suspended sediment determines light penetration into the water column, thus influencing submerged vegetation development. On the other hand vegetation exerts a stabilizing action on bottom sediment, thereby affecting light availability and giving rise to a positive feedback, with significant consequences for the overall morphodynamic evolution of the system. Suspended sediment distribution is analyzed here using remote sensing, to overcome the spatial limitations of traditional *in situ* point observations. Remote sensing retrievals were then used to evaluate suspended sediment distributions produced by a shallow water hydrodynamic and transport model with application to the Venice lagoon. The importance of vegetation stabilization at the whole system scale is established in the process.

The models developed and applied in this thesis are able to describe the processes studied and to predict future scenarios at different scales, with the interesting possibility of being incorporated one into the other.

The stomatal optimization model which accounts for the salinity effect at the leaf level can be incorporated in the soil-plant-atmosphere continuum model, in which stomatal conductance is the main link between the plant and the atmosphere. Salinity can be accounted for in this approach in a direct manner by introducing an osmotic potential in the soil. Such a model at a large scale can be incorporated in mathematical models of sediment transport, which cannot neglect the effect of vegetation, as shown by the comparison with remote sensing maps.

Chapter 1

Soil-Plant Interactions

1.1 Plants: the water conduit from soil to atmosphere

Water movement from the soil to the atmosphere through plant transpiration is an important link in the hydrologic cycle and the study of the processes regulating the root water uptake is a very active field within several disciplines, such as hydrology, soil science, agroscience, and atmospheric science.

In this Chapter, the linkages between plant transpiration and soil moisture dynamics are explored through different root-water-uptake models. In analogy with electrical systems, the driving force of water movement from the soil to the atmosphere is the water potential gradient, to which the water flux is proportional through a series of conductances. In Figure 1.1 the water potentials of the soil (ψ_s), the xylem (ψ_x), the leaf (ψ_L), and the atmosphere (ψ_a) are indicated, as well as the conductances of the soil-root interface ($g_{s,r}$), of the xylem (g_x) and of the stomata (g_s).

The water potential in the soil is the sum of different contributions. In particular, the water potential is influenced by the matric potential given by soil moisture content, by the osmotic potential given by solutes, and the

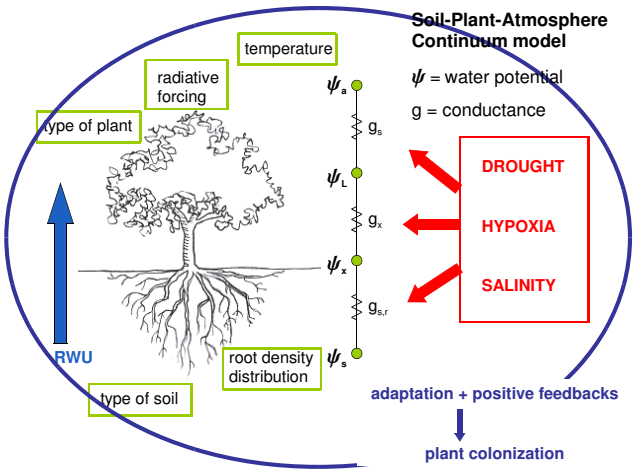

Figure 1.1: Root-water-uptake (RWU) by plant roots: schematization of pathway, influencing factors and stress conditions.

gravitational potential given by elevation (Gardner, 1965; Porporato et al., 2001).

The root water uptake depends on many factors, such as environmental conditions (temperature, light, atmospheric evaporative demand), the type of soil and the type of plant (displaying different root density distributions, active roots, xylem, stomatal, and root conductances).

Because water flow through a plant is driven by gradients in the total water potential, plant water uptake is affected by any change in water potentials along the pathway between the soil and the atmosphere. Therefore, plants adapt their physiology in order to maximize their carbon gain, i.e. stomatal opening, while limiting their water loss as influenced by several possible stress conditions,such as drought, anoxic/hypoxic conditions and water salinity.

Water transport in the plant occurs through three possible pathways: the apoplastic, the symplastic, and the transcellular pathways (Figure 1.2). The apoplast is the the part of the plant tissue located outside the cell membrane

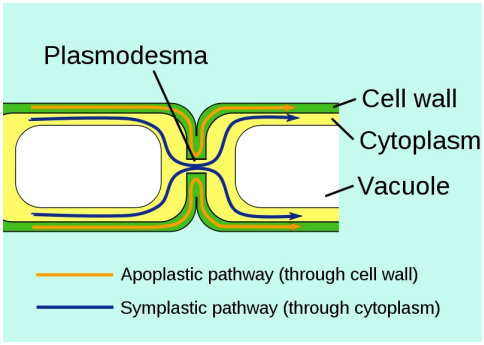

Figure 1.2: Schematization of water transport pathways in the roots (picture from Wikipedia.org).

and it includes both cell walls and intercellular spaces. The symplast is the inner side of the plasma membrane and allows direct cytoplasm-to-cytoplasm flow of water and of other nutrients along concentration gradients and it is used in the root systems to bring in nutrients from soil. The third pathway is transcellular: the water flows from cell to cell through the cell membranes. In plants the total water flux is a combination of these three pathways (Tyree, 2003).

A major driver of plant water uptake is water availability in the soil, mediated by the amount of roots in the soil. Interestingly, roots can significantly affect water availability in different soil layers by redistributing water at night: active roots can extract water from deeper and wetter soil layers and release water into the top dryer layers. This mechanism, known as hydraulic lift, has been studied in the last years both through models (Richards & Caldwell, 1987; Domec et al., 2010) and experiments. Evidence of hydraulic lift has been reported for shrub, grasses and tree species, and for temperate, tropical and desert ecosystems (Caldwell et al., 1998; Feddes et al., 2001; Doussan et al., 2006; Siqueira et al., 2008; Domec et al., 2010). Hydraulic lift can enhance transpiration in dry climates, where plant transpiration (and carbon uptake) could be limited by water stress conditions (Dawson, 1993; Caldwell et al., 1998; Feddes et al., 2001; Mendel et al.,

2002). In spite of the importance of this water redistribution mechanism, very few root models currently account for hydraulic lift in their formulations (Siqueira et al., 2008).

Root water uptake may represented mathematically as a sink term, $S(z,t)$, in the continuity equation (Lai & Katul, 2000; Siqueira et al., 2008) (written here in 1D):

$$\frac{\partial \theta(z,t)}{\partial t} = -\frac{\partial q(z,t)}{\partial z} - S(z,t) \tag{1.1}$$

where θ is the soil moisture, t is time, q is the water flux given by the Darcy's law $q = -K\frac{\partial h}{\partial z}$, K is the hydraulic conductivity, h is the total potential energy or pressure head $h = z + \psi$, ψ is the water potential and z is the elevation.

The actual evapotranspiration E_{act} is then computed as (Lai & Katul, 2000):

$$E_{act} = \int_0^{L_{root}} S(z,t)dz = \beta E_p, \tag{1.2}$$

where L_{root} is the root depth and E_p is the potential evapotranspiration. In this formulation it is clearly $0 < \beta < 1$.

In eq. (1.2) it is assumed that no water storage can occur within the plant and that the amount of water extracted by the roots is exactly balanced by transpiration by the leaves (Braud et al., 1995).

Root water uptake models typically fall within two main possible approaches (Braud et al., 2005; Varado et al., 2006):

- A microscopic (single-root) approach: the radial flow of water toward and into an individual root can be represented by an infinitely long cylinder of uniform radius and water absorbing properties. The information necessary to implement this approach is not easily available, especially at the large scale. Given the level of detail required by this

type of models and the limitations posed to the incorporation of such small-scale models in general eco-hydrological descriptions, they will not be treated here.

- A macroscopic (root-system) approach: root water extraction is incorporated as a sink term in the mass conservation equation. Two subgroups can be identified:

  - empirical approaches satisfying the water mass balance but not explicitly incorporating the water energy balance. The root water uptake is typically dependent on the effective root-density distribution, soil moisture content, atmospheric demand and hydraulic conductivity (Lai & Katul, 2000). These models do not require detailed information about the physical processes regulating root water uptake and their parameters are relatively easy to obtain. In the following I will refer to this type of models as "Potential evapotranspiration driven models".

  - physically-based approaches, considering root water uptake at each soil level to be proportional to the water potential gradient between the soil and the leaves according to a set of resistances (of the soil, of the soil-root interface and of the plant). Resistances to water transfer (e.g. stomatal conductance as dependent on possible stresses) must be specified to implement such models. These models explicitly satisfy both the water mass and energy balance equations and will in the following be called "Energy driven models".

1.2 Potential evapotranspiration-driven models

Potential evapotranspiration-driven models provide the simplest description of plant water uptake. We will take as an illustrative example of this type of approach the model proposed by Lai & Katul (2000), who express root water uptake in each soil layer as:

$$S(\theta, z, t) = \alpha(\theta) g(z) E_p(t), \tag{1.3}$$

where $0 < \alpha(\theta) < 1$ is the efficiency function, which depends on the local soil moisture θ, and $g(z)$ is the root density function. The factor $g(z)E_p(t)$ gives the maximum root water uptake when the soil moisture content is not limiting ($\alpha = 1$).

1.2.1 Efficiency function formulation

Different formulations can be found in the literature for the efficiency function $\alpha(\theta)$. It can be computed with empirical models which depend on the local soil moisture or pressure head. In the following, a brief review of methods widely used in the literature is given.

1) According to **Lai & Katul (2000)**:

$$\alpha(\theta) = \alpha_1(\theta)\alpha_2(\theta); \tag{1.4}$$

$$\alpha_1(\theta) = max\left\{ \frac{\theta}{\theta_s - \theta_w}; \frac{\int_0^z \theta_{(z)} dz}{\int_0^L \theta_{(z)} dz} \right\}; \tag{1.5}$$

$$\alpha_2(\theta) = \left(\frac{\theta - \theta_w}{\theta_s} \right)^{\gamma/(\theta - \theta_w)}. \tag{1.6}$$

The term α_1 gives the maximum efficiency when the soil moisture is not limiting and is given by the maximum between two possible uptake-efficiency limits, taking into account not only the local soil moisture content but also its vertical distribution. In fact, the first term is "local" and takes into account that top roots are predominant in the case of rapid soil wetting following a precipitation event, while the second term is "global" and becomes predominant when deeper roots are more efficient than top roots in the case of uniform soil moisture vertical distribution. Root water uptake

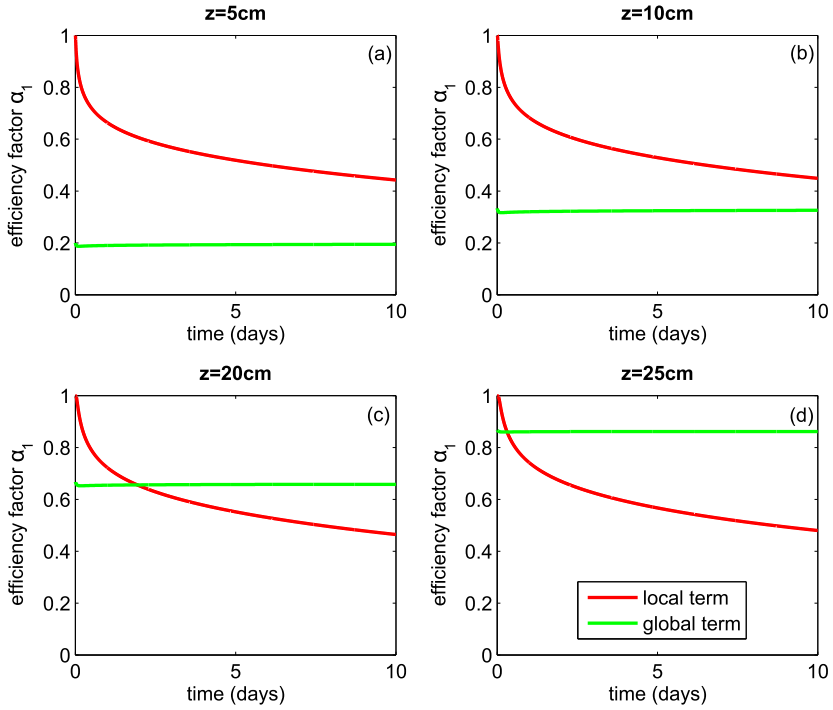

Figure 1.3: Representation of the local (red line) and global (green line) terms used in eq. (1.5) for different depths: (a) z=5 cm, (b) z=10 cm, (c) z=20 cm, (d) z=25 cm.

in each layer can, in fact, be turned on or off independently, as a result of the local water availability.

In Figure 1.3 the local and global terms are plotted for different layers (the root depth was here set to 30 cm). The local term (red line) only depends on the local soil moisture and in all cases it is close to unity at the beginning of the simulation, when soil moisture is close to saturation everywhere, and then declines as soil dries. On the contrary, the global term (green line) varies as a function of depth: it is low at the surface and it increases with depth, as deeper roots remain more moist over time and can thus uptake a greater amount of water.

The term α_2 is limiting when θ decreases (the root shut-down mechanism

occurring near the wilting point θ_w). α_2 varies between 0 (when soil moisture approaches wilting point) and 1 (when soil moisture approaches saturation). The rate at which α_2 approaches 0 is given by the parameter γ.

Braud et al. (2005) point out a problem in the formulation of the compensation function and propose to replace the first term of α_1 with

$$\frac{\theta - \theta_w}{\theta_s - \theta_w} \tag{1.7}$$

in order to prevent the actual transpiration from being higher than the potential value. They also show that the model proposed by Lai & Katul (2000) is quite sensitive to soil hydraulic properties, due to the formulation based on the volumetric water content rather than on the soil matric potential.

2) Collins & Bras (2007) replaced the term α_2 defined by Lai & Katul (2000) by another formulation derived by Rodriguez-Iturbe et al. (2001) which is more widely used and explicitly treats the two plant physiological parameters ψ_w and ψ^* corresponding to the volumetric water contents of θ_w and θ^*, respectively. They give

$$\alpha_2(\theta) = \begin{cases} 0 & \theta(z) \leq \theta_w \\ \frac{\theta(z)-\theta_w}{\theta^*-\theta_w} & \theta_w < \theta(z) \leq \theta^* \\ 1 & \theta^* < \theta(z) \end{cases}, \tag{1.8}$$

where θ^* is the saturation value at which uptake is equal to demand.

3) Laio et al. (2006) and Laio (2006) make this simplifying assumption: "plant uptake at a given layer is independent of the uptake occurring in the rest of the root zone. There is NO enhancement in water uptake from relatively wetter layers to compensate for the lower uptake from dryer layers. This choice is controversial, but it is in accordance with some of the most detailed uptake models available in literature." On the basis of these assumptions, they model $\alpha(\theta)$, the water stress parameter, as an increasing

function of soil moisture from the wilting point θ_w to field capacity θ_{fc}, both with a linear and a non linear relationships.

For the linear relation (see Porporato et al. (2004); Rodriguez-Iturbe & Porporato (2005)) they use

$$\alpha(\theta) = \frac{\theta - \theta_w}{\theta_{fc} - \theta_w}; \tag{1.9}$$

while for the non linear case they propose

$$\alpha(\theta) = \begin{cases} \frac{\theta - \theta_w}{\theta^* - \theta_w} & \theta < \theta^* \\ 1 & \theta^* < \theta < \theta_{fc} \end{cases}, \tag{1.10}$$

where θ^* is the soil moisture level above which plant stomata are completely opened.

4) Feddes et al. (1978) propose a dimensionless soil water availability factor as a function of pressure head described by:

$$\alpha(h) = \begin{cases} \frac{h - h_4}{h_3 - h_4} & h_3 > h > h_4 \\ 1 & h_2 \geq h \geq h_3 \\ \frac{h - h_1}{h_2 - h_1} & h_1 > h > h_2 \\ 0 & h \leq h_4 \; or \; h \geq h_1 \end{cases}. \tag{1.11}$$

In this model water uptake is reduced both at high and low water contents, for oxygen or water stress respectively. Uptake occurs at the potential rate when the pressure head is $h_3 \leq h \leq h_2$. It drops off linearly when $h > h_2$ or $h < h_3$, and becomes zero when $h \leq h_4$ or $h \geq h_1$. In general, the value of h_3 is expected to be a function of the evaporative demand (Figure 1.4).

Pressure head limits are species-specific and Table 1.1 reports some examples (Feddes & Raats, 2004).

The water stress function in eq. (1.11) has been widely used in the literature (Li et al., 2001; Homaee et al., 2002b; Skaggs et al., 2006). Interestingly,

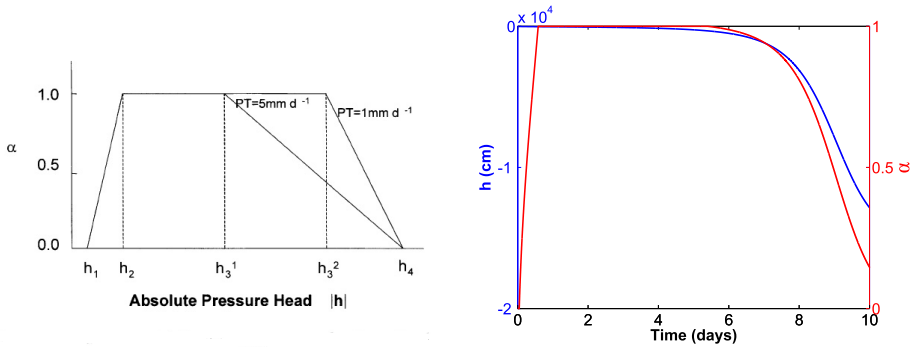

(a) (b)

Figure 1.4: Representation of the efficiency factor as the Feddes function. (a) Stress term α as a function of soil water pressure head (Feddes et al., 1978; Li et al., 2001). (b) Representation of the stress factor α (red line) and of water pressure head h (blue line) for a simulation of 10 days.

Table 1.1: Critical pressure-head values h (cm) of the sink-term function $\alpha(h)$ shown in Figure 1.4 and eq. (1.11) for some main agricultural crops (after Wesseling 1991, from Feddes & Raats (2004)).

Crop	h_1	h_2	$h_{3,high}$	$h_{3,low}$	h_4
Potatoes	-10	-25	-320	-600	-16000
Sugar beet	-10	-25	-320	-600	-16000
Wheat	0	-1	-500	-900	-16000
Pasture	-10	-25	-200	-800	-8000
Corn	-15	-30	-325	-600	-15000*

* after Veenhof and McBride (1994)

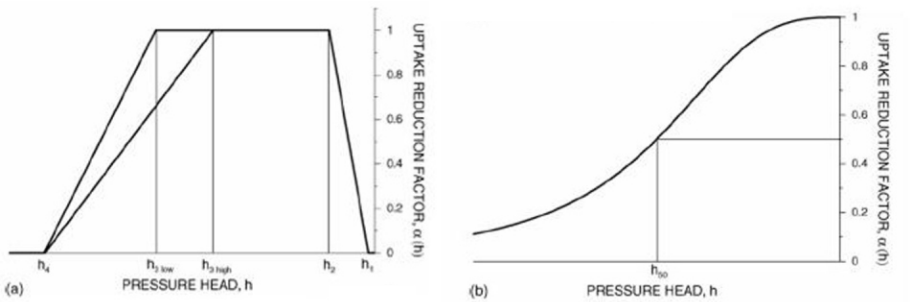

Figure 1.5: Plots of (a) the Feddes et al. (1978) reduction function (eq. (1.11)) and (b) the VanGenuchten (1987) function (eq. (1.12)) (From Skaggs et al. (2006)).

Homaee et al. (2002a), Homaee et al. (2002c), and Homaee & Schmidhalter (2008) propose a modification of this formulation, which includes a salinity stress function.

5) VanGenuchten (1987) proposes another stress function based on the pressure head h (also discussed in Homaee et al. (2002b); Skaggs et al. (2006)):

$$\alpha(h) = \frac{1}{1 + (\frac{h}{h_{50}})^p}, \tag{1.12}$$

where h_{50} and p are adjustable parameters (h_{50} is the soil water pressure head at which $\alpha(h)$ is reduced by 0.5).

Figure 1.5 shows the comparison between the Feddes and the VanGenuchten stress functions.

1.2.2 Root density distribution

Several root density distribution vertical profiles, which describe the amount of roots at each soil layer, are reported in the literature.

Jackson et al. (1996) propose the following equation:

$$Y = 1 - \beta^d \tag{1.13}$$

where d is the root depth and Y is the proportion of roots from the

surface to depth d (cumulative root fraction). β is a simple numerical index of rooting distribution dependent on vegetation type.

following Lai & Katul (2000) we will also consider here a linear root density distribution from Hoogland et al. (1981):

$$g(z) = \frac{2cz}{L^2} + \frac{1-c}{L}; \tag{1.14}$$

where c is a slope parameter (if $c = 0$ the linear distribution is obtained), z is the soil depth, and L is the root depth and the expression proposed by Jackson et al. (1996):

$$g(z) = -a^z ln(a), \tag{1.15}$$

where a is an empirical parameter.

Braud et al. (2005) use, instead, the expression:

$$g(z) = g_0 \frac{exp(-bz)[1.5 + 0.5exp(-bz)]}{1 + exp(-bz)}, \tag{1.16}$$

where g_o is the root density at the soil surface and b is a parameter characterizing the exponential decrease of the root density distribution.

In Collins & Bras (2007) the vertical root profile is described by the linear dose response (LDR) model (Schenk & Jackson, 2002):

$$Y(z) = \frac{1}{1 + (z/D_{50})^c}; \tag{1.17}$$

where $Y(z)$ is the cumulative fraction of total root mass between the soil surface and depth z; D_{50} is the depth above which 50% of the root mass is located and c is a shape parameter.

Hao et al. (2005) present six different root density distribution models.

Because the root vertical profile is likely not 'universal', but rather the result of responses to environmental forcings, some have attempted to infer it by solving some optimization problems. The underlying idea of this approach is that each plant develops the roots in order to maximize its

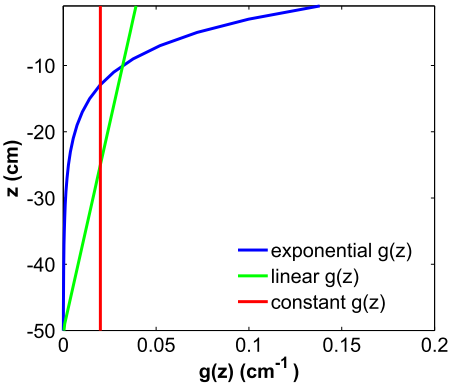

Figure 1.6: Root density distributions $g(z)$ used in the simulations: constant (red), linear (green) and exponential (blue) (the parameter values adopted are: root depth=50 cm; c=-1 (eq. (1.14)), and a=0.85 (eq. (1.15)).

growth, and thus transpiration, and minimize the possible stresses. According to this approach plants allocate an 'optimal' root profile as a function of climatic regime, and soil type. Collins & Bras (2007) and (Laio et al., 2006), for example, assume that an optimal vertical root profile should aim at maximizing mean annual transpiration.

In order to fully explore such assumptions it is useful to develop a root model, which can incorporate a generic vertical root distribution and provide a realistic description of root functioning, e.g. by including the role of roots in the redistribution of water from wetter to dryer soil layers or their response to salinization. With this aim in mind, I consider here three root vertical distributions to be used to develop and test such a model against existing observations and previous results: the uniform distribution (eq. (1.14)), the linear distribution (eq. (1.14)), and the exponential distribution (eq. (1.15)) (see Figure 1.6)

1.3 Energy driven models

The models expressing plant water uptake as linear function of the gradient of the water potential along the pathway from the soil, through the plant and to the atmosphere are based on a more realistic representation of physical processes, but require more a detailed specification of the parameters.

Several contributions in the literature refer to this type of approach. Guswa et al. (2002) expresses water uptake by plants using a model based on previous results by Gardner (1965). Plant uptake is proportional to the difference between the soil water potential at layer i, h_i, and the plant water potential, H_p, through two resistances in series: one associated with water movement through the root tissue (always at layer i), $r_{r,i}$, and one associated with water movement from the soil to the roots, $r_{s,i}$. The local uptake function is described mathematically by:

$$\sigma_i = \delta z_i \frac{h_i - H_p}{r_{s,i} + r_{r,i}}, \tag{1.18}$$

where δz_i is the thickness of the soil layer and the sink term of eq. (1.1) is given by

$$S = \sum_i \sigma_i. \tag{1.19}$$

The authors assume H_p to be constant. The two resistances are modeled as functions of the unsaturated hydraulic conductivity, the local root density, and of parameters that account for root diameter, geometry and arrangement (see Section 1.3.1).

Braud et al. (1995) propose a simple soil-plant-atmosphere transfer (SiSPAT) model in which root water uptake is also modeled using an electrical analogue scheme. The leaf water potential is calculated by assuming that the total moisture extraction equals the transpiration as calculated from the atmospheric conditions.

Siqueira et al. (2008, 2009) propose a soil-plant model in which the root water uptake is hydraulically controlled and is a function of the difference between local root water potential and local soil water potential at the root-soil interface. They decompose the 3D Richards' equation into two 1D directionally distinct coupled components: a radial component (scale of millimeters) and a vertical component (scale of meters).

The hydraulically controlled root water uptake q_r (m/s) is given by:

$$q_r(z) = K_r[\psi_r - z - \psi(r_r, z)], \tag{1.20}$$

where r and z are radial and vertical coordinates, K_r is the root membrane permeability, ψ_r is the root pressure referenced to ground level (this is the main link between the soil and the leaf system), ψ is soil water potential and r_r is the root radius.

1.3.1 A model for Root Water Uptake based on a water potential formulation

In this Section a new model of root-water-uptake based on water potential gradients will be developed. A water potential formulation has been chosen because it more closely represents the actual physical processes involved, and it allows to directly account for stress factors. In coastal areas, one of the main focus of the present Thesis, salinity is the main stress factor impairing plant growth, which can be easily incorporated in the model proposed here, by considering how it affects the osmotic, and thus the total, water potential. Depending on the type of plant, salt-tolerant or freshwater, salinity also changes the metabolic apparatus and the stomatal regulation, such that these effects must also be included in the soil-plant-atmosphere continuum model in order to obtain a consistent representation of plant responses to its main stressors. Chapter 2 will describe how these processes can be accounted for in the present framework. I describe below several

possible parametrizations to be included in the model, to be compared in Section 1.4.

The state and the water flux characterizing the soil-plant-atmosphere continuum may be defined in terms of (see Figure 1.7 for a representation which considers just two soil layers for simplicity, the general case being a straightforward extension):

- ψ_a = water potential in the atmosphere (cm);
- ψ_L = water potential within the leaf (cm);
- ψ_R = water potential in the xylem (cm);
- ψ_i = water potential in the soil at layer i (here we assume for simplicity $i = 1, 2$) (cm);
- g_s = stomatal conductance (s^{-1});
- g_x = conductance of the xylem (s^{-1});
- k_i = conductance of the soil-root interface at layer i (s^{-1}).

As shown in Figure 1.7, each layer is assumed to be directly linked to the xylem by the root biomass allocated in that specific layer. The soil-root conductance within the generic layer i is then assumed to be proportional to the amount of roots in that layer.

The transpiration rate (cm/s) is thus defined as

$$E = g_x(\psi_R - \psi_L); \tag{1.21}$$

and the flux of water (cm/s) from layer i to the xylem through the root biomass allocated in that layer (here $i = 1, 2$ as in Figure 1.7) is

$$q_1 = k_1(\psi_1 - \psi_R); \tag{1.22}$$

$$q_2 = k_2(\psi_2 - \psi_R). \tag{1.23}$$

For continuity it must be:

$$E = q_1 + q_2 = k_1(\psi_1 - \psi_R) + k_2(\psi_2 - \psi_R). \tag{1.24}$$

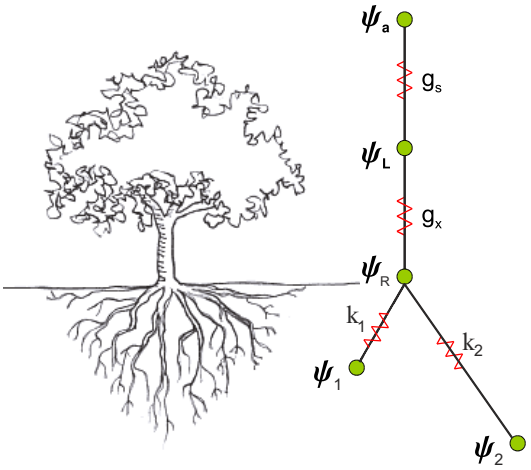

Figure 1.7: Schematic representation of a root system. The ψ's are water potentials, the k's represent conductances.

Rearranging eq. (1.21) ψ_R can be defined as:

$$\psi_R = \psi_L + \frac{E}{g_x} \tag{1.25}$$

Substitution in eq. (1.24) yields the following:

$$\begin{aligned} E &= k_1\left(-\psi_L - \frac{E}{g_x} + \psi_1\right) + k_2\left(-\psi_L - \frac{E}{g_x} + \psi_2\right) = \\ &= -k_1\psi_L - \frac{k_1}{g_x}E + k_1\psi_1 - k_2\psi_L - \frac{k_2}{g_x}E + k_2\psi_2; \\ E\left(1 + \frac{k_1}{g_x} + \frac{k_2}{g_x}\right) &= k_1\left(\psi_1 - \psi_L\right) + k_2\left(\psi_2 - \psi_L\right); \\ E &= \frac{\left[k_1\left(\psi_1 - \psi_L\right) + k_2\left(\psi_2 - \psi_L\right)\right] g_x}{g_x + k_1 + k_2}. \end{aligned}$$

Generalysing to the case of n layers, the following result is obtained:

$$E = \frac{\left[\sum_i k_i\left(\psi_i - \psi_L\right)\right] g_x}{g_x + \sum_i k_i}. \tag{1.26}$$

Eq. (1.26) gives the transpiration flux from a plant, taking into account the continuity equation in the root system. Similar formulations can be fund in the literature (Gardner, 1965; Braud et al., 1995; Sperry et al., 1998; Guswa et al., 2002; Siqueira et al., 2008; Nishida & Shiozawa, 2010), with different levels of approximations and different formulations of the closure for the leaf and xylem water potentials. Here I develop a model that will be suitable for repeated numerical integrations to address the root profile optimality problem. The water potential in the soil ψ_i at each layer i is given by soil properties (soil moisture and salinity) and can be computed from the soil water content θ by solving the Richards' equation (1.1). The xylem conductivity g_x depends on the type of plant and some typical values can be found in the literature; it typically depends on the leaf water potential. The soil-root conductivity k_i can be assumed to be proportional to the root density function; however, it also depends on the type of plant and its parametrization is one of the main uncertainties in this type of models.

Another important issue is the definition of the leaf water potential ψ_L. In some applications it is fixed, but this assumption is quite strong because, in reality, it depends on the soil water potential and the atmospheric demand. ψ_L is of key importance because it regulates the actual transpiration.

To close the problem, we must now also consider an atmospheric layer as shown in Figure 1.7, that is the atmosphere. In this manner, plant transpiration is not only governed by the soil water potential), but also by the evaporative atmospheric demand. The transpiration from eq. (1.26) must thus be equal to the evapotranspiration computed from the difference in the water vapour pressure between the leaf and the atmosphere. Several formulations can be used to model the vapour flux between the leaf and the atmosphere and the stomatal conductance, which will be briefly reviewed below. Now, we will discuss in some detail the parameters involved in the

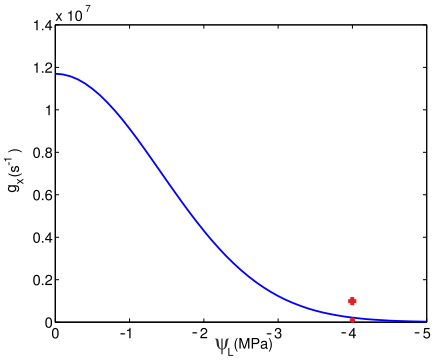

Figure 1.8: Xylem conductance vulnerability curve. The two points shown are measured values.

root model presented.

Xylem conductance

The xylem conductance g_x depends on the water potential in the plant: plant conductance decreases, because of cavitation, as the water potential decreases (Sperry et al., 1998).

The so called vulnerability curve (the vulnerability of xylem to cavitation) gives the value of g_x (per unit ground area) as a function of the leaf water potential ψ_L. Daly et al. (2004) give the following formulation:

$$g_x = g_{x,max} exp[-(-\psi_L/d)^c], \tag{1.27}$$

where $g_{x,max} = 11.7 \mu m\ MPa^{-1}\ s^{-1}$, $d = 2\ MPa$ and $c = 2$.

The xylem conductance is given here in $\mu m\ MPa^{-1}\ s^{-1}$ so in order to have units of $1/s$, MPa must be converted to m.

The relationship in eq. (1.27) is shown in Figure 1.8, and the two points shown are other xylem conductance values (assumed constant) found in literature (Siqueira et al., 2008; Braud et al., 1995).

Stomatal conductance

Several formulations have been proposed in literature for the stomatal conductance g_s, which is usually described by mechanistic models.

Here two classical formulations will be compared, one proposed by Siqueira et al. (2008), the other by Daly et al. (2004) (based on the Jarvis model). A third formulation based on a novel approach which uses optimization theories (Cowan & Farquhar, 1977; Berninger & Hari, 1993; Hari et al., 1986, 1999, 2000; Makela et al., 1996; Katul et al., 2009, 2010; Manzoni et al., 2011) will be also explored.

Siqueira et al. (2008) propose the following expression:

$$g_s = g_0 + (g_{max} - g_0)\ f_v, \tag{1.28}$$

with the reduction function f_v given by

$$f_{\psi_L}(\psi_L) = \frac{1 + exp(s_f \psi_f)}{1 + exp[s_f(\psi_f - \psi_L)]}, \tag{1.29}$$

where $s_f = 3.14\ 10^{-2} m^{-1}$, $\psi_f = -193m$, $g_0 = 4.8\ 10^{-4} mol/m^2 s$ and $g_{max} = 0.56 mol/m^2 s$.

The resulting g_s has the units of $mol/m^2 s$ and it has to be divided by the molar density of gases (41.4 $mol\ m^{-3}$ at a 20° C temperature and a pressure of 101.3 kPa) to obtain the units in mm/s. In this model the stomatal conductance is only dependent on the leaf water potential, while other environmental parameters (light, temperature...) are considered constant.

The model originally proposed by Jarvis and used in Daly et al. (2004), computes the stomatal conductance as the product between a maximum stomatal conductance value and several limiting functions:

$$g_s = g_{smax} f_\phi(\phi) f_T(T) f_{\psi_L}(\psi_L) f_{VPD}(VPD) f_{CO_2}(CO_2); \tag{1.30}$$

$$f_{\psi_L}(\psi_L) = \begin{cases} 0 & \psi_L < \psi_{L,0} \\ \frac{\psi_L - \psi_{L,0}}{\psi_{L,1} - \psi_{L,0}} & \psi_{L,0} \geq \psi_L \geq \psi_{L,1} \\ 1 & \psi_L > \psi_{L,1} \end{cases} . \tag{1.31}$$

where ϕ is the leaf available energy, T the temperature, ψ_L the leaf water potential, VPD the vapour pressure deficit and CO_2 the CO_2 concentration in air. Reduction functions for each of the parameters are given, but for simplicity the ambient conditions are here assumed to be fixed, such that the corresponding reduction functions are equal to 1. Only the reduction factor associated with the leaf water potential $f_{\psi_L}(\psi_L)$ is allowed to vary.

Vapor pressure deficit (VPD) is the difference between vapor pressure at saturation conditions p_{sat} and vapor pressure at ambient condition p_{amb}. Vapor pressure at saturation is computed using the Clausius-Clapeyron relation

$$p_{sat} = 0.611 e^{\frac{17.502T}{T+240.97}}, \tag{1.32}$$

where T is the temperature and $p_{amb} = p_{sat} * RH/100$.

Figure 1.9 shows the shape of the two reduction functions and of the resulting stomatal conductances as a function of the leaf water potential in the two cases.

Another approach to determine the stomatal conductance is based on optimization theories (see also Chapter 2), according to which plants regulate stomata aperture in order to maximize the carbon gain and minimize the water loss (Givnish & Vermeij, 1976; Cowan & Farquhar, 1977; Hari et al., 1986, 1999, 2000; Berninger & Hari, 1993; Arneth et al., 2002; Katul et al., 2009, 2010; Manzoni et al., 2011; Boer et al., 2011). In particular, eq. (14) from Katul et al. (2010) will be used in the present application :

$$g_s = \frac{a_1}{a_2 + sc_a} \left(-1 + \left(\frac{c_a}{a \, \lambda \, VPD} \right)^{1/2} \right), \tag{1.33}$$

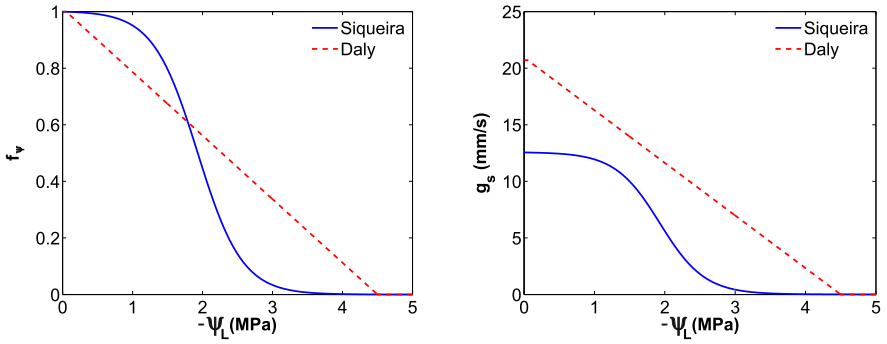

(a) (b)

Figure 1.9: Comparison between stomatal conductance models. (a) Leaf water potential reduction functions. (b) Stomatal conductance for the two models.

where a_1 and a_2 are photosynthetic parameters (see Chapter 2 for details), $s = 0.7$ is a model constant which allows to linearize the biochemical demand function, c_a is the CO_2 concentration in the atmosphere, $a = 1.6$ is the relative diffusivity of water vapour with respect to carbon dioxide, VPD is the vapour pressure deficit and λ is the cost parameter and the key parameter in the optimization (for details on the optimization function, please refer to Chapter 2 and to Katul et al. (2010)).

λ, the cost of water for the plant to complete the photosynthesis, depends on the leaf water potential ψ_L, and can be modeled with the following expression from Manzoni et al. (2011):

$$\lambda(\psi_L) = \lambda^*_{max} \frac{c_a}{c^*_a} exp\left[-\beta\left(\psi_L - \psi_{L,max}\right)^2\right], \tag{1.34}$$

where λ^*_{max} is the maximum λ at a reference $c_a = c^*_a = 400$ ppm, β is a fitting parameter and $\psi_{L,max}$ is the leaf water potential at λ^*_{max}. Manzoni et al. (2011) report the values of λ^*_{max}, β and λ^*_{max} as a function of different species and climates.

Root-soil conductances

The conductance at the soil-root interface is a parameter difficult to determine, which depends on both the type of soil and the type of plant, but also on amount of the available moisture. Several formulations are proposed in the literature, and a brief review is provided here, together with typical measured values.

Braud et al. (1995) calibrate the total resistance of the plant, R_p, and compare it to values from the literature (Abdul-Jabbar et al., 1984). R_p is defined as the serial resistance of the roots ($R_{r,tot}$) and of the xylem (R_x). According to the values reported in Braud et al. (1995) $R_p \approx 4 \cdot 10^8\ s$ for soybean, while according to Siqueira et al. (2008) $R_p \approx 1 \cdot 10^9\ s$ for a generic crop, exemplifying a typical range of variability.

$R_{r,tot}$ is derived from the parallel resistances of each layer $R_{r,i}$ as follows:

$$\frac{1}{R_{r,tot}} = \sum \frac{1}{R_{r,i}}. \tag{1.35}$$

Braud et al. (1995) also provide the value of the ratio $\frac{R_{r,tot}}{R_p} = 0.758$ (also used by Nishida & Shiozawa (2010)), so from simple algebra one obtains $R_{r,tot} = 3 \cdot 10^8\ s$. Since $R_p = R_{r,tot} + R_x$ one obtains $R_x = 1 \cdot 10^8\ s$.

The resistance of the roots for layer i, $R_{r,i}$, is usually a function of the root density distribution function g_i only, while the resistance of the soil layers, $R_{s,i}$, also depends on the hydraulic conductivity K_i Gardner (1965); Guswa et al. (2002); Braud et al. (2005); Nishida & Shiozawa (2010).

According to Guswa et al. (2002):

$$R_{r,i} = \frac{C_r}{g_i}, \tag{1.36}$$

with $C_r \approx 4 \cdot 10^9\ s/cm$.

According to Braud et al. (1995); Nishida & Shiozawa (2010):

$$R_{r,i} = \frac{R_{r,tot}}{RDF_i}, \tag{1.37}$$

where RDF_i is the root density function at layer i and the relationship between RDF and root density distribution $g(z)$ is $g(z) \cdot dz = RDF(z)$, if dz is the thickness of the soil layer in the model discretization. In fact, it must be that $\sum_i RDF_i = 1$ and $\int g dz = 1$.

Guswa et al. (2002), similarly to other authors, defines the soil resistance as:

$$R_{s,i} = \frac{C_s}{g_i \cdot K_i}, \tag{1.38}$$

where C_s is an empirical parameter.

Gardner (1965); Braud et al. (1995); Nishida & Shiozawa (2010) use

$$R_{s,i} = \frac{1}{K_i \; g_i}. \tag{1.39}$$

For the simulations performed for this work, the following relationships are used, which are a combination of the previous ones, after verifying that the resulting conductances are comparable to the values reported in literature and that the resulting potential evapotranspiration is close to the measured values. They are given in terms of conductances ($k = 1/R$) rather than resistances (R) to be coherent with the model description provided previously.

$$k_{s,i} = 5 \; K_i \; g_i; \tag{1.40}$$

$$k_{r,i} = \frac{g_i \; dz}{3 \cdot 10^8}. \tag{1.41}$$

The soil-root conductance $k_{s,r,i}$ for the layer i is then computed considering the series of two conductances:

$$k_{s,r,i} = \frac{k_{s,i}\ k_{r,i}}{k_{s,i} + k_{r,i}}. \tag{1.42}$$

Determination of the leaf water potential

To close the problem described in Section 1.3.1, the calculation of the leaf water potential ψ_L is required. To this purpose, the transpiration rate given by eq. (1.21) is equated to the transpiration estimate derived from one of the classical micrometeorological formulations.

Transpiration can be computed according to the Pennman-Monteith formulation, e.g. (Daly et al., 2004):

$$E = \frac{(\lambda_w \gamma_w g_{ba} \rho VPD + S\phi) g_s LAI}{\rho_w \lambda_w [\gamma_w (g_{ba} + g_s LAI) + g_s LAIS]}, \tag{1.43}$$

where λ_w is the latent heat of water vaporization, $\gamma_w = (p_a c_p)/(0.622\lambda_w)$ is the psychrometric constant, VPD is the potential saturation deficit of the air, S is the slope of curve relating saturation vapor pressure to temperature, ϕ is the leaf available energy, g_s is the stomatal conductance (per unit leaf area), and g_{ba} (per unit ground area) is the series between the conductance of the leaf boundary layer g_b (per unit leaf area) and of the atmospheric boundary layer g_a (per unit ground area). LAI is the leaf area index.

A similar formulation is given in (Siqueira et al., 2008):

$$E = \frac{M_w}{\rho_w R_g} g_s \left(\frac{h_v e_{sv}}{T_{sv}} - \frac{e_{av}}{T_{av}} \right), \tag{1.44}$$

where R_g is the universal gas constant, M_w and ρ_w are the water molecular weight and density, respectively, T_{sv} and e_{sv} are leaf temperature and saturation vapor pressure at leaf temperature, respectively, T_{av} and e_{av} are temperature and vapor pressure of the air surrounding the leaves, h_v is fractional relative humidity in the leaf intercellular spaces, and g_s is the stomatal conductance.

Another simple and intuitive formulation, which expresses E with the same physical process of eq. (1.44), based on stomatal conductance and pressure gradients, is given by:

$$E = a\ g_s\ VPD; \tag{1.45}$$

where $a = 1.6$ is the relative diffusivity of water vapour with respect to carbon dioxide, g_s is the stomatal conductance and VPD is always the vapour pressure deficit.

Since g_s decreases with the absolute value of ψ_L (stomata close when water starts to be scarce), transpiration computed with eq.'s (1.43), (1.44) and (1.45) decreases with $|\psi_L|$. On the contrary, E computed with eq. (1.21) increases with $|\psi_L|$ and so the intersection between the two curves give the value of the leaf water potential and the evapotranspiration at the equilibrium between atmospheric demand and soil water availability.

This is a non-linear set of equations, which must be solved numerically, and a correct parametrization is crucial.

Figure 1.10 shows the shapes of the evapotranspiration fluxes computed in the different ways with eqq. 1.21 (red), 1.43 and 1.44 (blue), assuming $VPD = 1\ KPa$ and different values of the stomatal conductance as modeled in eqq. (1.28) and (1.30).

In the following, both eq. (1.43) and eq. (1.45) will be used and the results will be compared.

Soil properties

Two different soil types are considered in the analyses performed here, corresponding to sand and clay. Soil retention curves, which link the soil water content θ to hydraulic parameters, are taken from Clapp & Hornberger (1978) and are given by

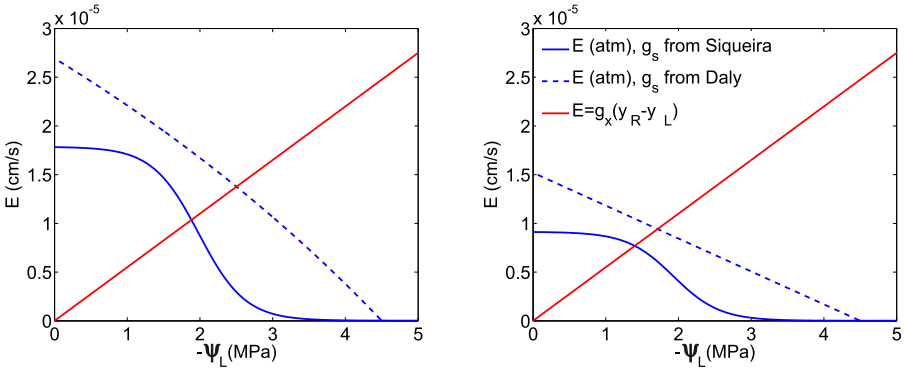

(a) $E(atm) = \frac{(\lambda_w \gamma_w g_{ba} \rho VPD + S\phi) g_s L_{AI}}{\rho_w \lambda_w [\gamma_w (g_{ba} + g_s L_{AI}) + g_s L_{AI} S]}$. (b) $E(atm) = \frac{M_w}{\rho_w R_g} g_s \left(\frac{h_v e_{sv}}{T_{sv}} - \frac{e_{av}}{T_{av}} \right)$.

Figure 1.10: Comparison between evapotranspiration fluxes. The intersections of the curves represents the equilibrium between evapotranspiration computed "from the bottom" (E) and evapotranspiration computed "from the atmosphere" (E_{atm}).

Table 1.2: Soil hydraulic properties for the two soil types used (Clapp & Hornberger, 1978).

Parameter	θ_s	b	K_s (cm/min)	ψ_s (cm)
SAND	0.395	4.05	1.056	12.1
CLAY	0.482	11.4	0.0077	40.5

$$\psi(\theta) = \psi_s \left(\frac{\theta}{\theta_s} \right)^{-b}; \tag{1.46}$$

$$K(\theta) = K_s \left(\frac{\theta}{\theta_s} \right)^{2b+3}; \tag{1.47}$$

where ψ is the soil water potential, K is the hydraulic conductivity, ψ_s is called saturation suction, K_s is the saturated hydraulic conductivity, θ_s is the soil moisture at saturation and b is an empirical parameter. Such soil-dependent parameters are taken from Clapp & Hornberger (1978) and are summarized in Table 1.2.

The shapes of the curves for the two types of soils are given in Figure 1.11.

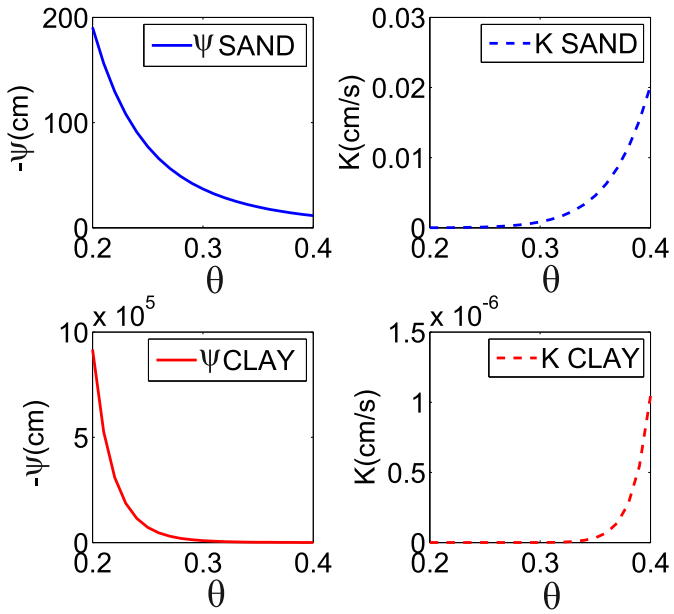

Figure 1.11: Soil water retention and hydraulic conductivity functions for the two soils considered in this study.

The model has been solved with a forward finite difference scheme (or explicit Euler method, see Gambolati (2002)) in time and space, and the soil hydraulic conductivity has been computed for each soil layer as the harmonic mean of the two K of the upper and lower nodes computing K_{avg} as

$$K_{avg} = 2\frac{K_i\ K_{i-1}}{K_i + K_{i-1}}. \tag{1.48}$$

1.4 Results

1.4.1 Results for the potential evapotranspiration driven models

In this Section, model results from with the formulation based on reduction functions of the potential evapotranspiration will be presented, particularly in relation to the models of Lai & Katul (2000) (eqq. (1.4), (1.5) and (1.6))

and Feddes et al. (1978) (eq. (1.11)).

Clayey soil is considered in the simulation (parameters in Table 1.2, wilting point: θ_w=0.1). The parameter γ in eq. (1.6) is set to 0.1, according to Lai & Katul (2000) and the parameters a (eq. (1.15)) and c (eq. (1.14)) describing the shape and the slope of the root density distributions functions are set to 0.85 and -1, respectively. The root depth is set to 50 cm.

For the solution of the 1D Richards' equation, the length of the soil domain is 1 m and the spatial discretization is 2 cm. The simulation length is 10 days and the time step is 1 minute. The initial condition for the soil moisture is set to 70% of the saturation conditions, uniformly along the vertical direction. The boundary condition at the top is zero flux (no infiltration), while the bounday condition at the bottom is free gravitatiional drainage. For these first model evaluations potential transpiration is set to a constant 5 mm/d during the day and during the night.

For the Feddes formulations, values reported in Table 1.1 for the crop are used as critical pressure-head limits (where $h_3 = h_{3,high}$).

Figure 1.12 shows the soil moisture vertical distribution evolution in time for the three different root density distributions and for the Lai&Katul efficiency function formulation. Water uptake depends on the amount of roots in each soil layer and the effect of the vertical root profile on the resulting soil moisture distribution is clearly evidenced. The soil is drying throughout the simulation (colors from red to blue). The soil preferentially dries in the upper layers for the linear and the exponential distributions. Similar results are obtained when the Feddes efficiency function is used (Figure 1.13).

Transpiration, that is computed as the sum of the local root-water-uptake at the different soil layers, also depends on the local amount of roots and is greater for the constant root profile and lower for the exponential one (Fig.s 1.14, 1.15). The Feddes formulation induces a greater differ-

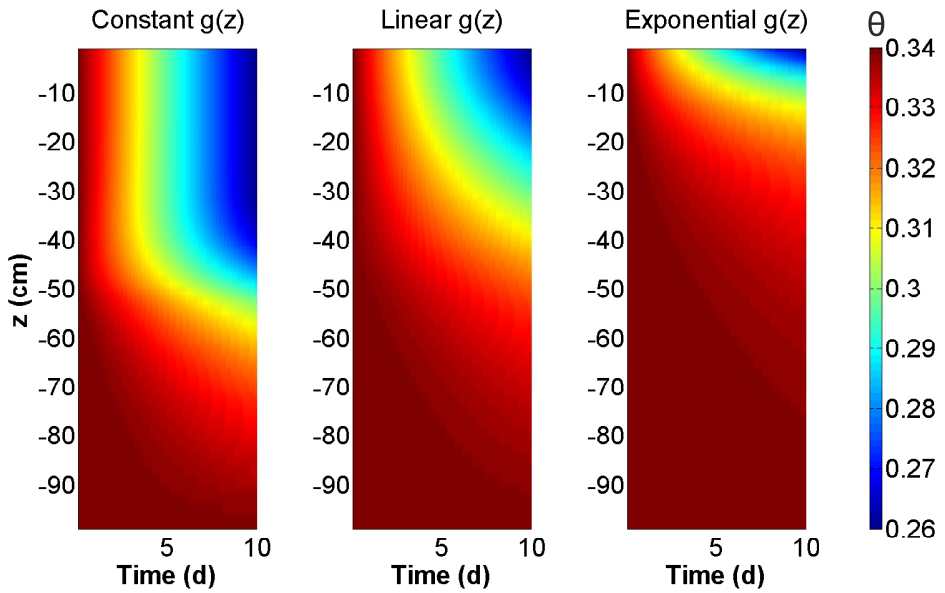

Figure 1.12: Soil moisture vertical distribution evolution in time for the constant, linear, and exponential root profile computed using the Lai&Katul efficiency function model.

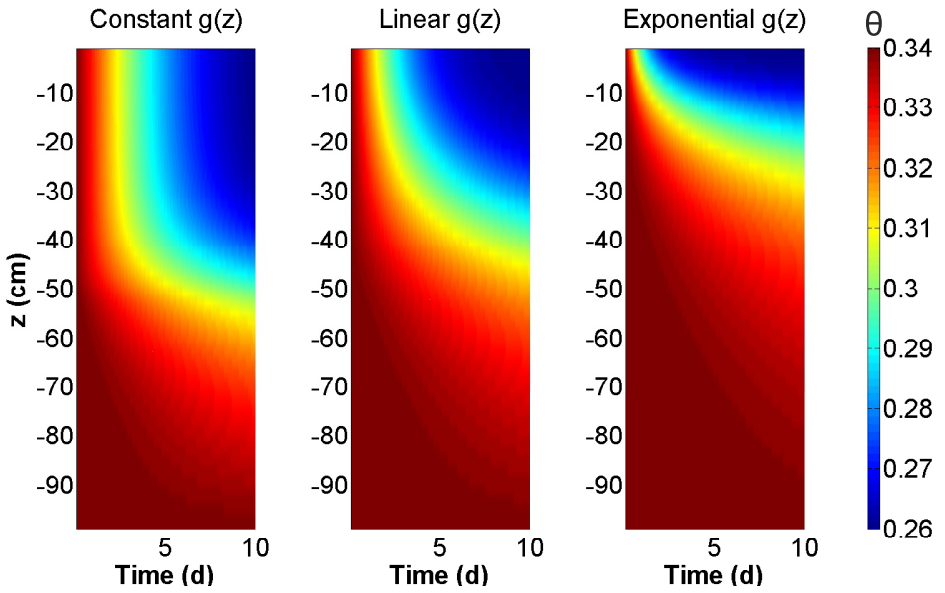

Figure 1.13: Soil moisture vertical distribution evolution in time for the constant, linear, and exponential root profile computed using the Feddes efficiency function model.

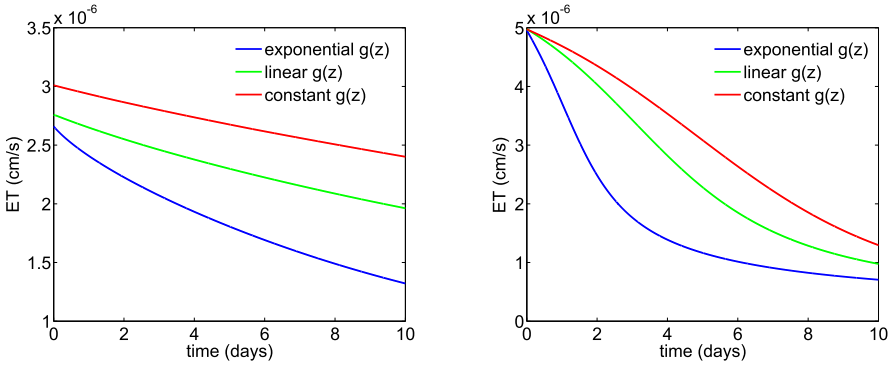

(a) Lai&Katul formulation.

(b) Feddes formulation.

Figure 1.14: Evapotranspiration as a function of time for the three root distributions modeled with the Lai&Katul (a) and the Feddes (b) functions.

ence between the exponential root profile and the remaining two. These results suggest the constant root profile to be most efficient in promoting the amount of water transpired by the plant. This is somewhat in contrast with the results of some global analyses of root distributions (Jackson et al., 1996; Schenk & Jackson, 2002)indicating that the exponential and the power-law root distributions as the most common in nature. It must be noticed, however, that these preliminary numerical evaluation assume simplified conditions. For example, no infiltration is considered, and the exponential root distribution may well be the most efficient in capturing the water infiltrating from the upper layers. Moreover, no competition among different species is accounted for: also in this case, a plant with roots concentrated in the upper layers would likely have competitive advantages with respect to plants with a constant root profile. However preliminary, these results indicate that the model developed can be used to tackle the significant problem of root optimality, as a result of more realistic forcings.

Figure 1.16 shows root-water-uptake for different soil layers and time steps for the Lai&Katul formulation. At the beginning of the simulation, when the soil moisture distribution is constant, the uptake is proportional

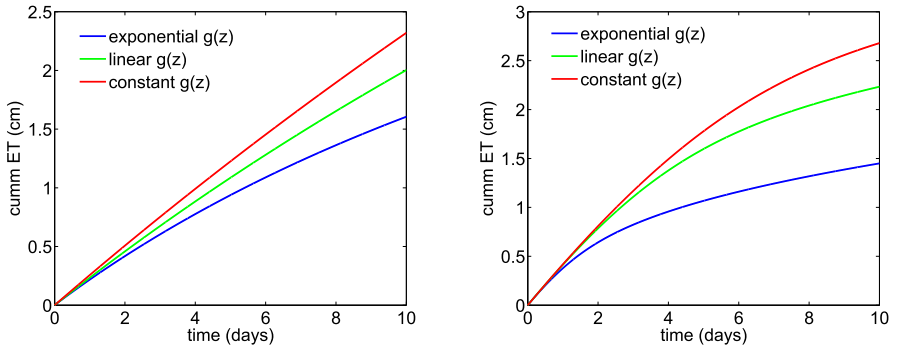

(a) Lai&Katul formulation.

(b) Feddes formulation.

Figure 1.15: Cumulative Evapotranspiration as a function of time for the three root distributions modeled with the Lai&Katul (a) and the Feddes (b) functions.

to the vertical root distribution, but when water becomes scarce in the upper layers, the uptake from deeper roots becomes important. This effect is particularly important for the constant root profile, which allocates the larges amount of roots in the deeper layers. This explains why evapotranspiration with a constant root profile is always larger than for the remaining profiles. Figure 1.17 shows the same results for the Feddes formulation. In this case the uptake depends only on a local factor, which is proportional to the pressure head at each soil layers according to eq. (1.11).

For all the simulations mass conservation was verified, by comparing the variation of the soil moisture in time (or water storage, $\Delta(\theta)$ in Figure 1.18) and the sum of the water lost through drainage and evapotranspiration. The results (Figure 1.18) show the good agreement of the mass balance.

1.4.2 Results with precipitation

The Root-water-uptake model with the Lai&Katul efficiency function formulation has been also applied to the case with precipitation. In this scenario, rain is a source of water and the top boundary condition changes over time as a function of the current moisture content. In particular, the Dunnian

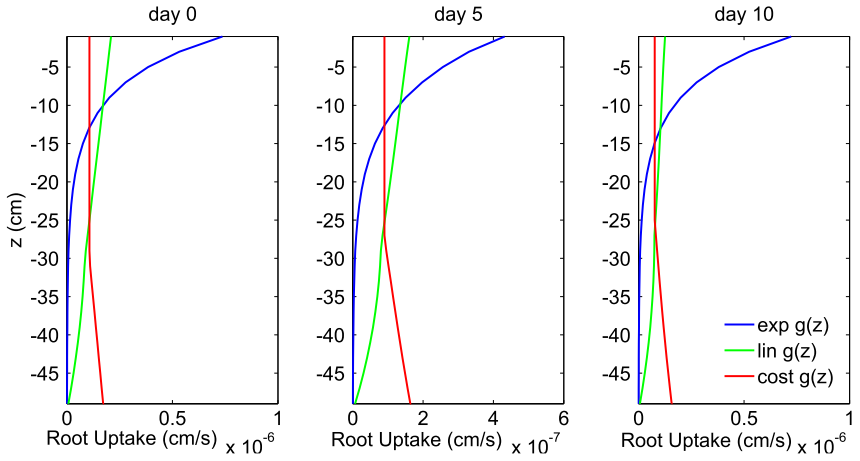

Figure 1.16: Root-water-uptake vertical distribution for the three root distribution functions, for the Lai&Katul formulation. The three panels refers to different times: 0, 5, and 10 days after the beginning of the simulation.

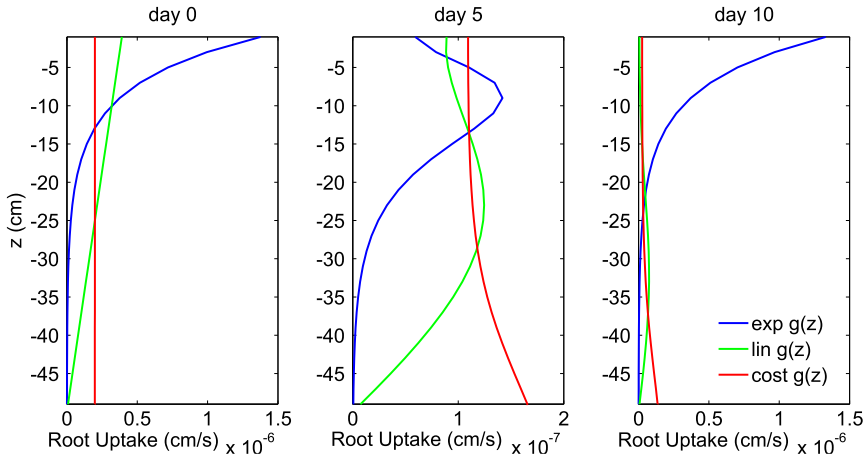

Figure 1.17: Root-water-uptake vertical distribution for the three root distribution functions, for the Feddes formulation. The three panels refers to different times: 0, 5, and 10 days after the beginning of the simulation.

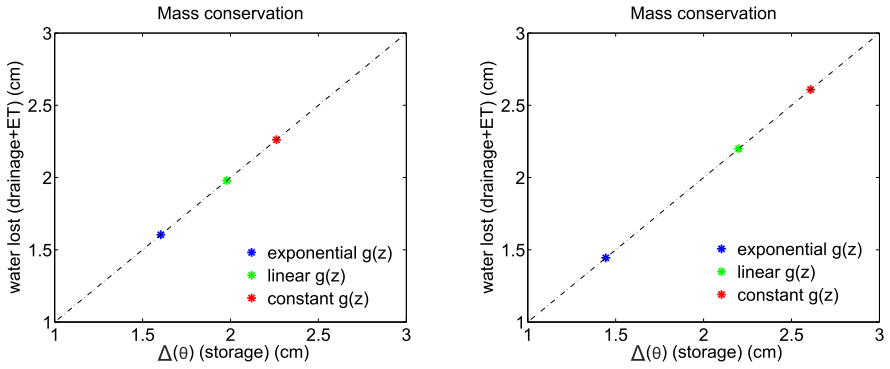

(a) Lai&Katul formulation.

(b) Feddes formulation.

Figure 1.18: Mass conservation check for the Lai&Katul (a) and the Feddes (b) functions.

control on infiltration is imposed as a top boundary condition setting the infiltration to zero when the soil moisture reaches the saturation value. When the soil moisture is lower than saturation, the Hortonian mechanism controls the amount of rainfall that infiltrates into the soil: if the precipitation flux is lower than the hydraulic conductivity, then all the rain infiltrates into the soil, while if the precipitation flux is greater than the hydraulic conductivity, then infiltration is equal to the hydraulic conductivity.

During rainfall water uptake by the plant roots is set to zero.

The results for a sandy soil, with a time step of 10 s and a constant initial soil moisture, equal to 50% of the saturation value, are shown and discussed in the following.

The dynamics of the soil moisture vertical distribution does not exhibit significant differences among the constant, linear, and exponential root profiles (Figure 1.19). In all three cases the plots show the increased soil moisture as a result of rainfall.

The transpiration and the cumulative transpiration (Figures 1.20 (a) and (b)) show higher values for the constant root profile and lower values for the exponential one, as in the case without precipitation. It can be seen here

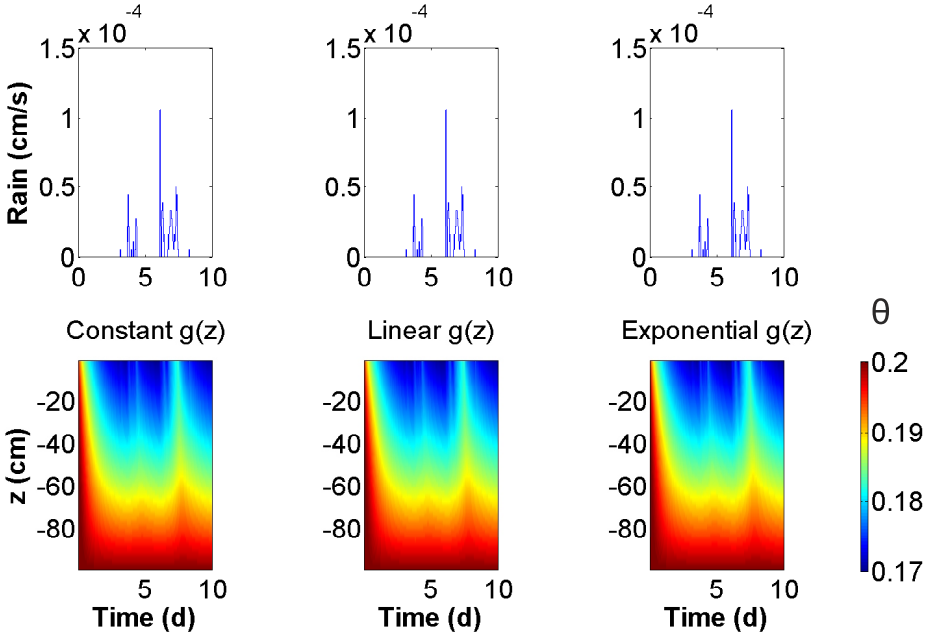

Figure 1.19: Soil moisture vertical distribution evolution in time for the constant, linear, and exponential root profiles computed using the Lai&Katul efficiency function model with precipitation. Top panels show the rainfall distribution.

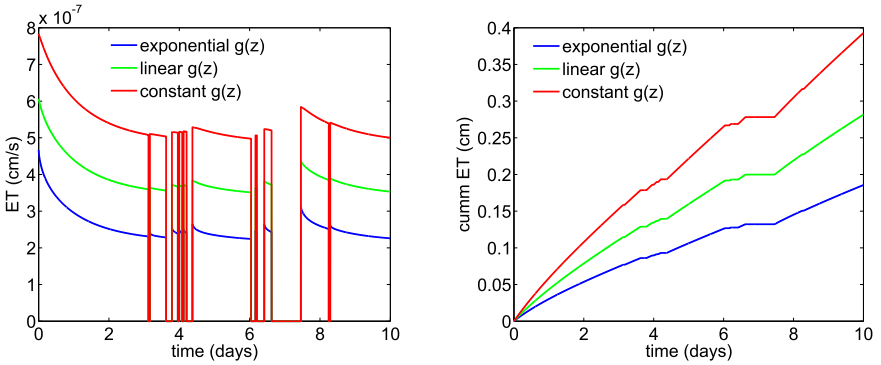

(a) (b)

Figure 1.20: Transpiration (a) and Cumulative transpiration (b) with precipitation as a function of time for the three root distributions.

that the root water uptake is zero while raining: in Figure 1.20(a) the fluxes drop to zero, while in 1.20(b) the cumulative flux remains constant while raining.

Figure 1.21 shows the root water uptake vertical profile at three times, which is seen to be a function of both the root distribution and the local soil moisture, as in the previous results (Figure 1.16).

1.4.3 Results for the Energy-driven model

The model described in Section 1.3.1 has also been implemented and the main results obtained from its application will be presented in this Section.

First, the formulations of stomatal conductance based on a reduction function (eqq. (1.28) and (1.29)) and eqq. (1.43) for the evapotranspiration are used. For simplicity, the vapor pressure deficit VPD is assumed to be constant during the day ($VPD = 0.01$KPa), while the leaf area index is set to $LAI = 3$. Eq. (1.27) was used for the xylem conductance. A clayey soil is assumed in the simulations. The length of the roots is set to 50 cm and the initial soil moisture condition is uniformly set to 70% of the saturation water content.

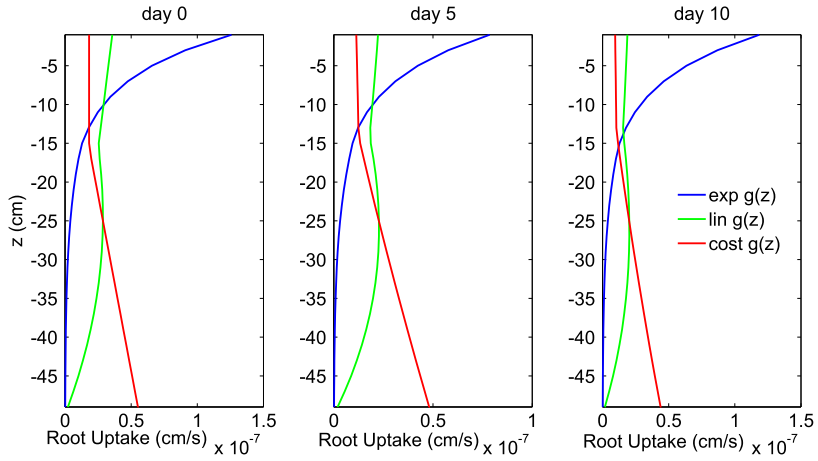

Figure 1.21: Root-water-uptake vertical distribution with precipitation for the three root distribution functions, for the Lai&Katul formulation. The three panels refer to different time: 0, 5, and 10 days after the beginning of the simulation.

The results are quite similar to those obtained for the potential evapotranspiration driven models, especially for the Feddes formulation (Section 1.4.1), both in terms of the time change of the soil moisture vertical distribution (Figure 1.22) and the transpiration (Figure 1.23).

The root water uptake vertical distribution (Figure 1.24) indicates that also in this formulation the uptake depends not only on the amount of roots, but also on the local soil moisture availability. The root-uptake flux is positive in all cases: this means that no water redistribution is occurring because water flows from the soil to the plant at all times.

Finally, Figure 1.25 shows the resulting leaf water potential ψ_L as a function of time while soil dries and the verification of the mass balance.

1.4.4 Results for the Energy driven model using stomatal conductance optimization theories

In this Section, a new approach to close the problem of determining the leaf water potential will be presented. The stomatal conductance is modeled using the optimization approach described in Section 1.3.1 and in Chapter

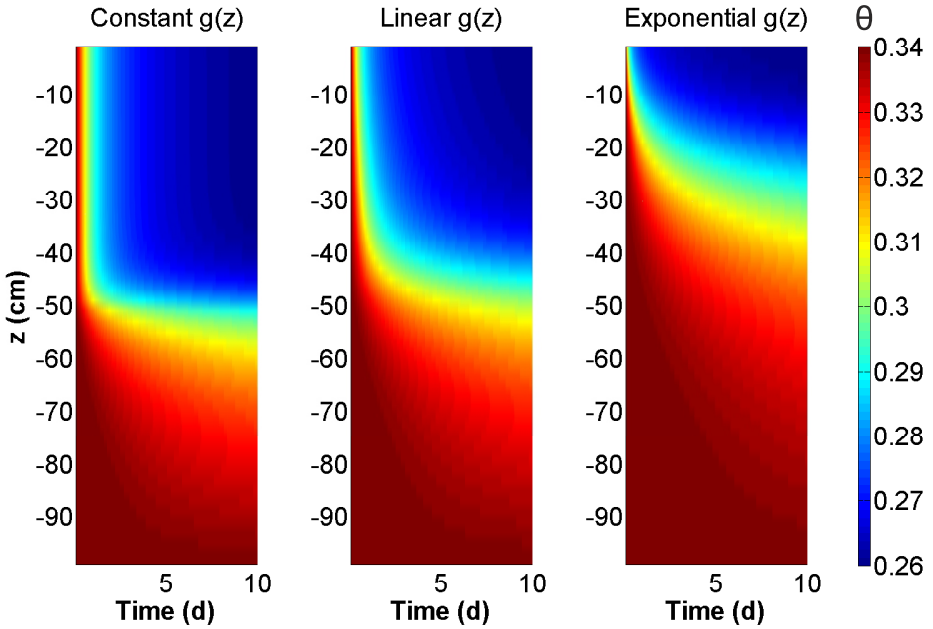

Figure 1.22: Soil moisture vertical distribution evolution in time for the constant, linear, and exponential root profile obtained from a water potential gradient formulation.

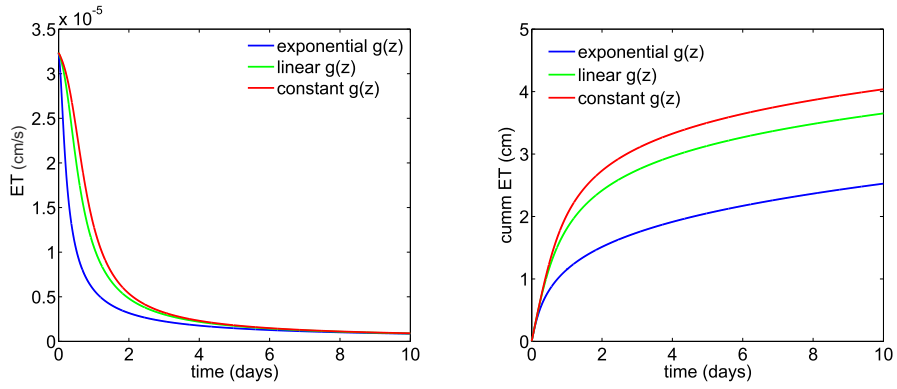

(a) (b)

Figure 1.23: Transpiration (a) and Cumulative Transpiration (b) for the energy driven model as a function of time for the three root distributions.

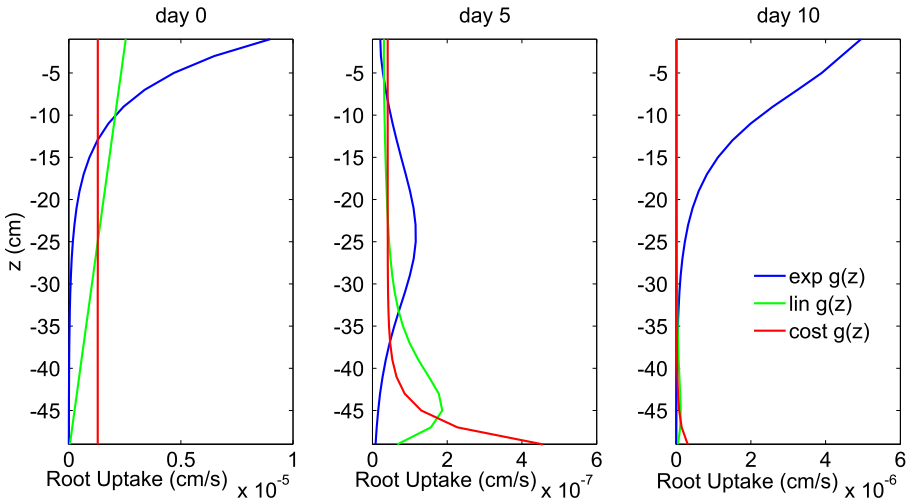

Figure 1.24: Root-water-uptake vertical distribution for the energy driven model for the three root distribution functions. The three panels refer to different times: 0, 5, and 10 days after the beginning of the simulation.

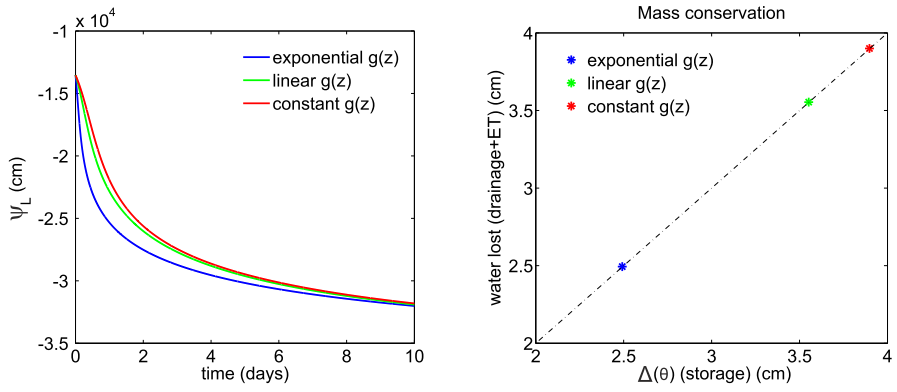

(a) (b)

Figure 1.25: Leaf water potential (a) and mass balance (b) for the energy driven model.

2. Plant transpiration is then computed using eq. (1.45).

Vapor pressure deficit (VPD) is computed as described before (eq. (1.32)).

Being light attenuation the largest non-linearity at the atmospheric level, a multilayer model for the canopy has been adopted. Canopy height is set to 60 cm with a spatial discretization step of 1 cm.

The cost parameter λ is computed with eq. (1.34) with parameters reported for forbs and grasses and wet climates by Manzoni et al. (2011) ($\lambda^*_{max} = 5970$, $\beta = 1.16$, and $\psi_{L,max} = -1.32$). To avoid oscillations in the cost parameter λ, the leaf water potential used in this expression is computed as the mean leaf water potential of the previous 24 hours.

λ is the key parameter in the optimization theory, and it represents the cost of water for the plant to carry out photosynthesis, which regulates the opening of the stomata as a function of water available in the soil, and possible other stress factors (see Chapter 2). As a consequence, λ increases with soil moisture deficit, as verified in measured data in the Duke forest (Figure 1.26). Concurrent measured data of evapotranspiration and soil moisture are used to calculate first the value of stomatal conductance g_s by expliciting eq. (1.45) and then to calculate λ expliciting eq. (1.34). The inferred value of λ is then related to the value of the soil moisture averaged on the depth and the results are reported in Figure 1.26.

Stomatal conductance for unit leaf area and for each layer in the canopy is modeled with eq. (1.33). The photosynthetic parameters a_1 and a_2 are chosen, for each layer in the canopy, among light-limited or rubisco-limited conditions by comparing the photosynthesis in the two cases and selecting the lower (limiting) one. Assuming rubisco limitation $a_1 = V_{cmax}$ and $a_2 = K_c(1 + C_{o,a}/K_o)$, where V_{cmax} is the maximum carboxylation capacity (V_{cmax} at 25°C=81.3μmol m^{-2} s^{-1} according to Novick et al. (2004), data for grasses in the Duke Forest.), K_c and K_o are the Michaelis constants for CO_2 fixation and oxygen inhibition, and C_{oa} is the oxygen concentration

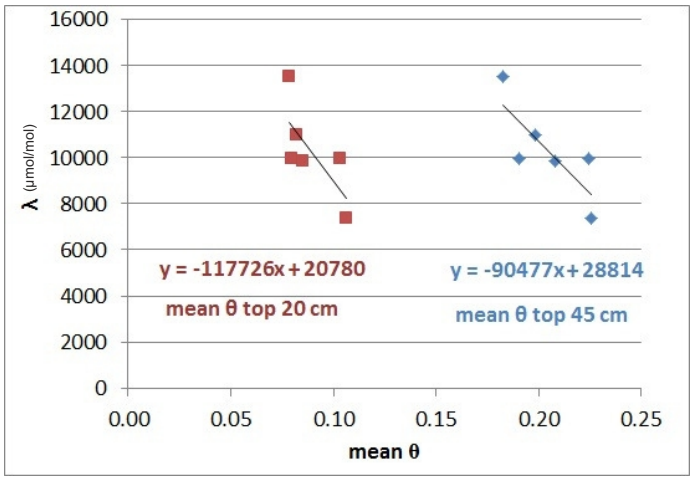

Figure 1.26: $\lambda - \theta$ relationship retrieved from measured data. Red points refer to soil moisture vertically averaged over the top 20 cm, blue points refers to soil moisture averaged over top 45 cm.

in the atmosphere. Assuming light limitation, $a_1 = \alpha_p e_m Q_p = \gamma Q_p$ and $a_2 = 2c_p$, where α_p is the leaf absorptivity of photosynthetically active radiation, e_m is the maximum quantum efficiency of leaves, γ is the apparent quantum yield determined from empirical light-response curves, and c_p is the CO_2 compensation point. Parameters are taken from Farquhar et al. (1980) and adjusted for temperature according to Campbell & Norman (1998).

Photosynthesis at each canopy layer is then computed with the total biochemical demand as (Farquhar et al., 1980)

$$A_{leaf} = \frac{a_1(c_i - c_p)}{a_2 + c_i}, \tag{1.49}$$

where c_i is the internal CO_2 concentration. The total photosynthesis A is the sum of all the contributions in the canopy height.

The internal CO_2 concentration c_i is computed at each time step as a function of the actual stomatal conductance and the photosynthesis by expliciting the Fickian equation

$$A = g_s(c_a - c_i), \tag{1.50}$$

where c_a is the CO_2 concentration in the atmosphere (assumed equal to 380 ppm).

All the photosynthetic parameters, relative to the unit leaf, are referenced to the ground area by using the leaf area index (LAI=3).

Potential evapotranspiration PET is computed using the Priestley-Taylor model (Fisher et al., 2005)

$$PET = \frac{\alpha \Delta An}{\Delta + \gamma}, \tag{1.51}$$

where Δ is the derivative of saturated vapor pressure versus temperature, An is total available energy (net radiation minus soil heat flux), and γ is the psychrometric constant. Δ and γ are functions of air temperature. α is an empirical parameter function of soil moisture, it ranges from 1.26 for well-watered vegetated and water surfaces to 1.74 for arid climates and for the model application is here set to 1.5.

The model has been first validated on soil moisture measurements taken in the Duke Forest and reported in Lai & Katul (2000). The period chosen for the model validation is one with no precipitation (3-17 July 1997) and the measured temperature, relative humidity, photosynthetic active radiation and the resulting vapor pressure deficit are reported in Figure 1.27.

The vegetation is grass and the soil is stratified as shown in Table 1.3.

The model can reproduce in a quite satisfactory way the soil moisture vertical profile evolution (Figure 1.28 (a)) and the evapotranspiration as a function of time (Figure 1.28 (b)).

After validation, the model has been employed to investigate possible differences with other types of models. Clay homogeneous soil has been used, with initial soil moisture conditions equal to 90% of saturation.

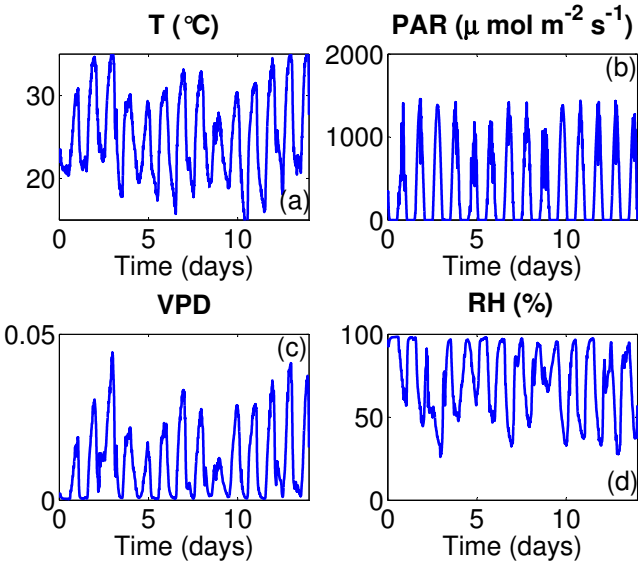

Figure 1.27: Measured temperature T, relative humidity RH, photosynthetic active radiation PAR in the Duke Forest, and the resulting vapor pressure deficit VPD.

Table 1.3: Soil hydraulic properties in the Duke forest (Lai & Katul, 2000).

Depth (cm)	Soil texture	K_s (cm/d)	θ_s	ψ_s (cm)	b
0-16	Silt loam	15.1	0.30	32.0	4.0
17-22	Loam	5.1	0.38	10.0	4.5
24-33	Silt clay loam	5.5	0.45	62.6	6.5
34-37	Silt clay	3.5	0.56	20.0	7.0
38-45	Clay	1.5	0.63	30.0	10.6

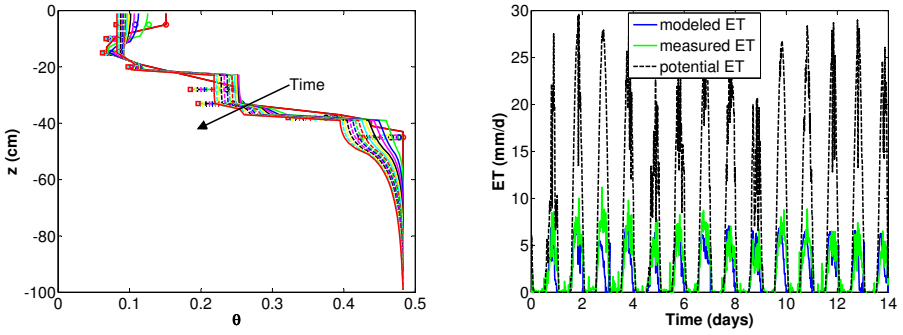

(a) (b)

Figure 1.28: Validation of the model with measures in the Duke Forest. (a) Soil moisture vertical profile: lines represent model, dots represent observations, the arrow shows the direction in which time is passing. (b) Evapotranspiration modeled (blue line), measured (green line), and potential evapotranspiration modeled (black dashed line).

Climatic forcings are assumed periodical and the values of temperature T, relative humidity RH and photosynthetic active radiation (PAR) are reported in Figure 1.29. They are obtained by interpolating measured values in the Duke Forest (Durham, North Carolina, USA).

Figure 1.30 shows the soil moisture vertical distribution evolution in time. Results are similar to those obtained previously, but for the diurnal oscillations due to periodical environmental forcings.

The evapotranspiration flux and the cumulative evapotranspiration (Figures 1.31 (a) and (b)) consistently show higher values for the constant root profile and lower values for the exponential one.

From the local root water uptake contributions (Figure 1.32), a compensation mechanism can be noticed: indeed, according to the local soil moisture and the water available at different soil layers, in some cases there are negative values of the local uptake. In these cases, roots are not extracting water from the soil, but rather water is exiting from the roots to the soil

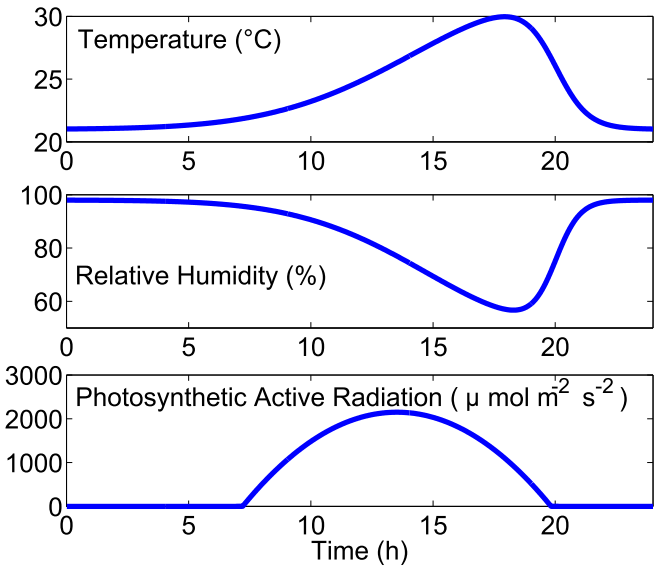

Figure 1.29: Climatic forcings used for the simulations: temperature, relative humidity and PAR.

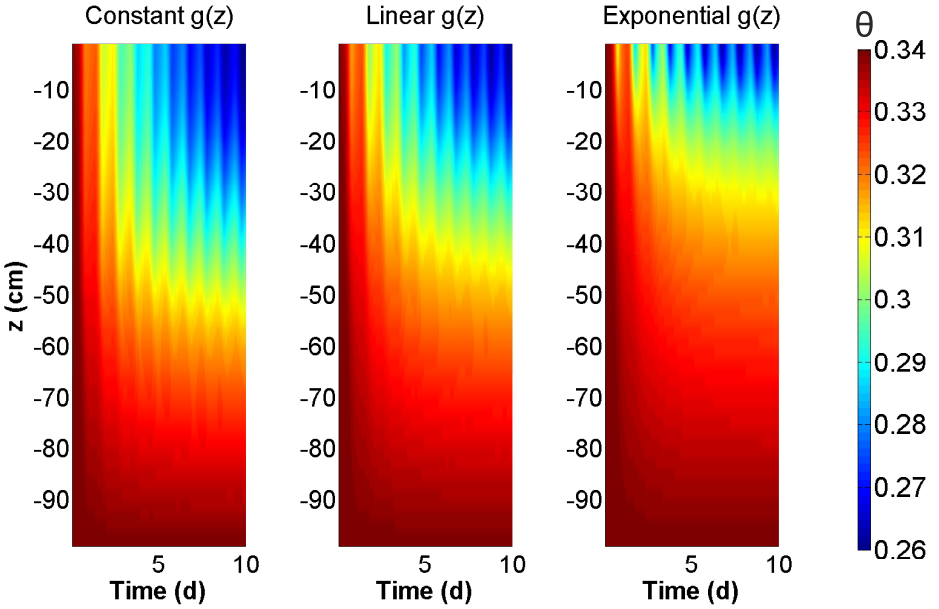

Figure 1.30: Soil moisture vertical distribution evolution in time for the constant, linear, and exponential root profile computing using optimal stomatal conductance formulation.

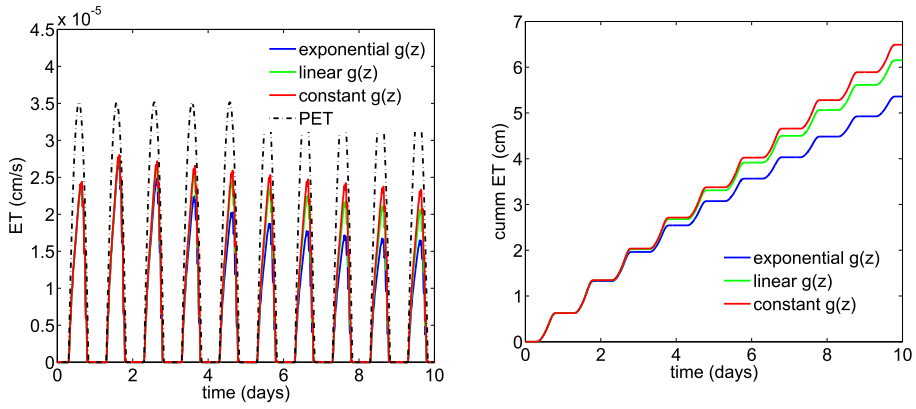

(a) (b)

Figure 1.31: Evapotranspiration (a) and Cumulative Evapotranspiration (b) for the optimal stomatal conductance formulation as a function of time for the three root distributions. Potential evapotranspiration (PET) is also reported.

where it is particularly dry. This mechanism, known as hydraulic lift, can enhance plant photosynthesis by water redistribution in the soil column.

Figure 1.33 shows the computed leaf water potential ψ_L and the mass balance, which is satisfied for the three root profiles.

Figure 1.34 shows the computed cost parameter λ (a), the stomatal conductance g_s (b), the ratio among internal and atmospheric CO_2 concentration c_c/c_a (c) and the photosynthesis A (d). λ in the first day has been fixed to a starting guess value, and after that it has been calculated as explained above, by using eq. (1.34) and using the mean leaf water potential of the previous 24 hours. λ increases with simulation time, because the cost of water increases as soil dries. As a consequence, plants close their stomata, and this is reflected in the reduction in g_s (Figure 1.34 (b)). The internal CO_2 concentration, as well as photosynthesis, remains almost constant in time for the exponential root profile, while it decreases in the other cases (Figure 1.34 (c) and (d)).

The approach developed is particularly convenient because it allows

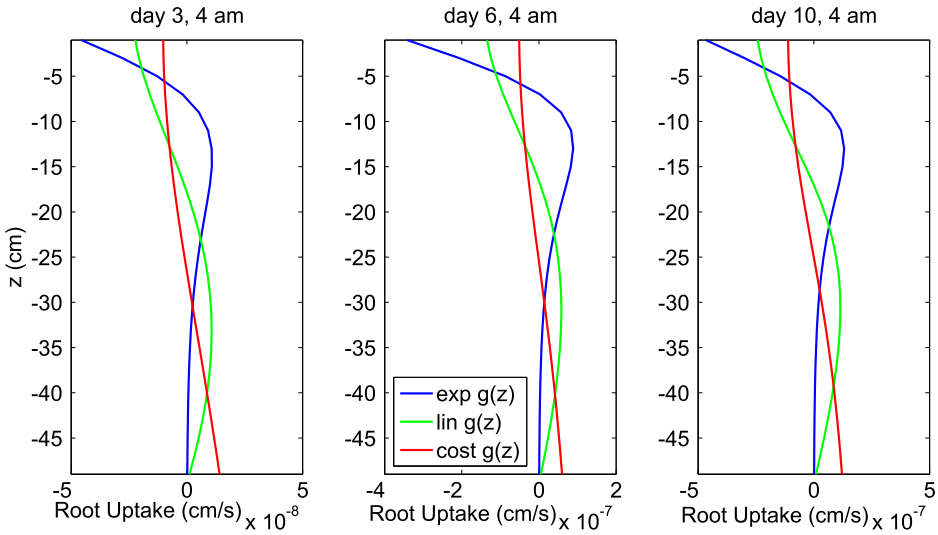

Figure 1.32: Root-water-uptake vertical distribution for the optimal stomatal conductance formulation for the three root distribution functions. The three panels refers to different time: 0, 5, and 10 days after simulation starts. Negative values indicate water flux from the plant to the soil.

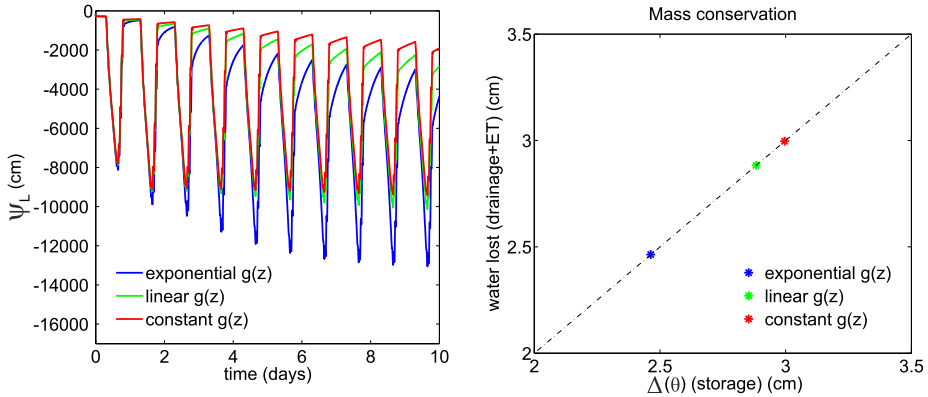

(a) (b)

Figure 1.33: Leaf water potential (a) and mass balance (b) for the optimal stomatal conductance formulation.

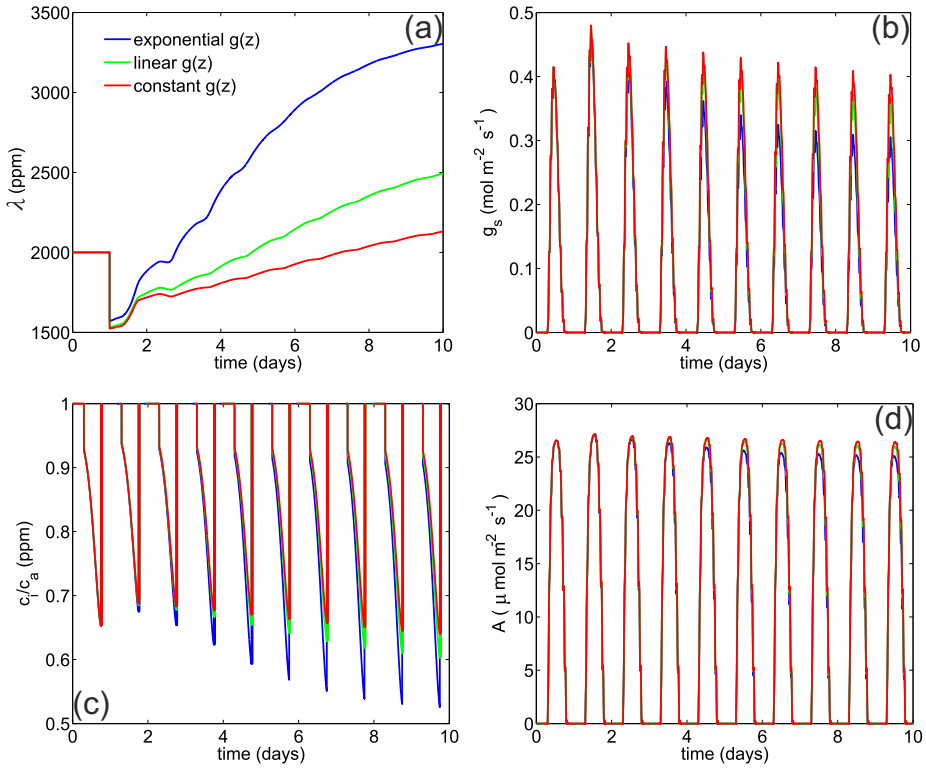

Figure 1.34: Modeled λ (a), stomatal conductance (b), ratio between CO_2 concentration in the plant and in the atmosphere (c) and photosynthesis (d) for the optimal stomatal conductance formulation and for the three root distribution functions.

to model both evapotranspiration and photosynthesis, which are of course linked one to the other through the cost parameter λ and are both regulated by the value of the stomatal conductance.

The model has been then used to simulate evapotranspiration and photosynthesis for different climate change scenarios. In particular, results will be presented for the clay soil type with linear root distribution, with initial conditions at 90% of saturation and for a simulation length of 30 days. The reference scenario ("REF") will be compared to an elevated ambient CO_2 scenario ("+CO_2") and to an elevated temperature scenario ("+T"). For the "+CO_2" scenario, the ambient CO_2 concentration is increased by 200 ppm, resulting in $c_a = 580$ ppm. For the "+T" scenario, the ambient temperature is increased by 4°C.

The results are shown in Figure 1.35, as a function of the mean soil moisture for the upper 60 cm of soil. All the values have been averaged on a daily basis, to obtain a representative daily value and to avoid all diurnal oscillations. Evapotranspiration (Panel (a)) increases with soil moisture for all scenarios, as expected, and has higher values when temperature increases. Under increasing ambient CO_2 concentration evapotranspiration is lower than the reference scenario. On the contrary, photosynthesis (Panel (b)) significantly increases under high CO_2: this is an expected result because the CO_2 in the atmosphere available for photosynthesis increases. Water use efficiency (WUE) is defined as the ratio among photosynthesis and evapotranspiration. The higher is this value, the more efficient is the plant in assimilating CO_2 and in limiting water loss. The results shown in Panel (c) clearly show that plant efficiency increases with CO_2, while it decreases with temperature; in all scenarios WUE declines with soil moisture, because evapotranspiration, which is at the denominator, becomes more important with respect to photosynthesis. Hydraulic lift (HL) has been computed adding all the negative contributions of the root-water-uptake. A negative flux means

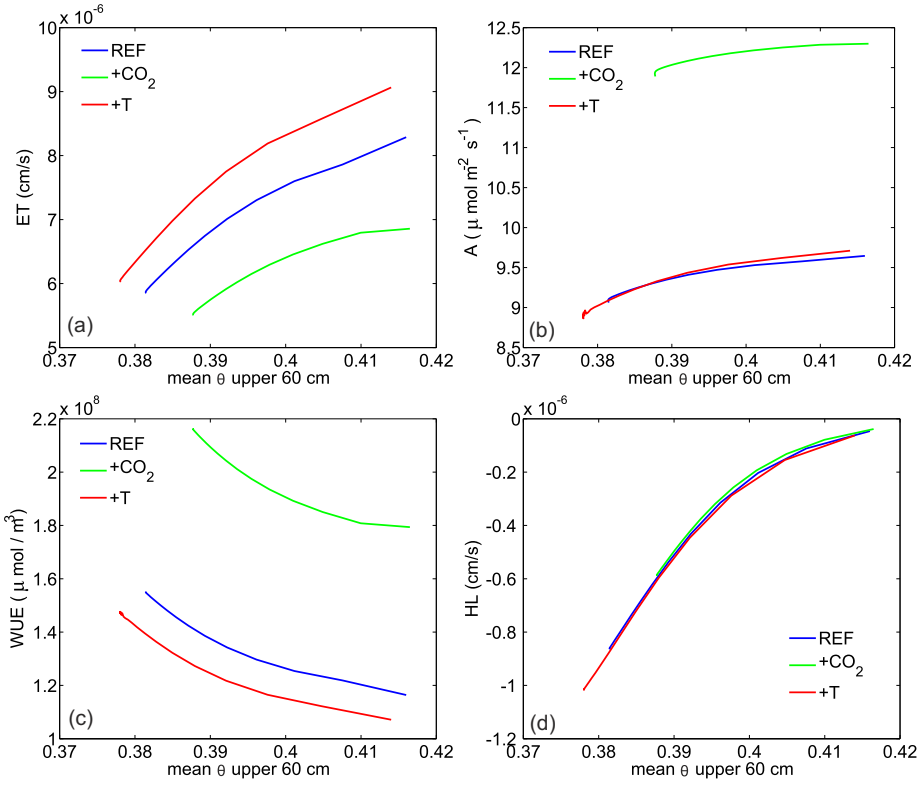

Figure 1.35: Effect of increasing atmospheric CO_2 concentration (green line) and temperature (red line) with respect to a reference scenario (blue line) on evapotranspiration (a), photosynthesis (b), water use efficiency (c), and hydraulic lift (d), as a function of vertically averaged soil moisture θ.

that the water is flowing in the direction from the roots to the soil. Panel (d) shows the very negligible effects of atmospheric CO_2 and temperature on hydraulic lift, while it is clear that HL increases with increasing available soil water content.

1.5 Discussion

The linkages between plant transpiration and water movement in the soil have been explored with a multi-layer soil plant model by using different root water uptake functions. Water movement in the soil has been modeled

with the 1D Richards' equation and plant water uptake has been represented with a sink term.

First, simpler empirical models have been implemented, in which plant uptake depends on the local amount of water in the soil and on the root distribution. The results obtained are consistent with known experimental behaviours, and the two different models give similar results. In all cases, the constant root profile maximizes plant evapotranspiration for simulations of 10 days when the soil is allowed to dry with no rainfall. This result is relatively unexpected since there is observational evidence in that the most common root distributions in nature are the exponential and the power-law distributions. However, many influencing factors are neglected in this application, such as rainfall, competitions among different species, and stress conditions. The empirical root water uptake formulations can account for some compensation mechanisms, according to which the local water uptake is dependent not only on the local soil moisture, but also on the global soil moisture profile, and thus the total evapotranspiration can proceed at higher rates. The results of this study confirm such behaviour, however any water redistribution mechanism happened: water never goes from roots to soil, but the direction is always entering in the plant.

The results of numerical experiments including rainfall and infiltration are quite similar to the previous ones, except for the soil wetting from the top. The uniform distribution maximizes transpiration also under this experimental setting.

As a second step, a physically-based model has been developed and implemented. Root water uptake is here dependent on the water potential gradient between the soil and the atmosphere and the modeled evapotranspiration, which now depends on the leaf stomatal conductance, can be related to the photosynthesis. After a literature review regarding plant physiology for model parametrization (to determine xylem, stomatal, root-soil

interface conductances), three different models for the stomatal conductance have been compared, using a multi-layer canopy model for light attenuation. The novelty here is to use an optimization approach to model the stomatal conductance; such application has been tested with field data for a stratified soil, where the model was shown to reproduce soil moisture dynamics and transpiration rates.

The results of the physically-based model showed that the constant root profile still maximizes transpiration, but with a smaller difference with respect to other root distributions. Moreover, results provide evidence of the hydraulic lift, that is water redistribution in the soil from wet to dry layers.

The model has been also used to explore how elevated ambient CO_2 concentration and air temperature affect canopy level photosynthesis, transpiration, and water use efficiency, soil moisture, and hydraulic redistribution.

The model developed has interesting further applications as it links in a physically-based manner soil moisture dynamics, plant transpiration and photosynthesis, giving the opportunity to study possible future scenarios to investigate the effect of climate change (as it has been done here for CO_2 and air temperature) on plant growth and soil properties.

Chapter 2

Leaf conductance and carbon gain under salt stressed conditions

2.1 Why Salinity?

In this Chapter, the salinity effects on plant photosynthesis and transpiration will be studied by developing an extension of a stomatal conductance model. Salinity issues are, indeed, important in several fields of application.

Salt stress adversely impacts plant growth, development, and yield, and has been the subject of extensive research over the past decades (e.g. Lunin & Gallatin (1965); Brady & Weil (2002)). Recovery of crop yield following rapid deterioration of soil fertility due to salt pollution is an important research priority in agricultural areas where irrigation water is saline and rainfall is limited, or in areas subject to recently intensified tsunami activities (Maas & Hoffman, 1977; Brady & Weil, 2002; FAO, 2005; Munns & Tester, 2008).

Saline water intrusion associated with sea level rise in coastal areas is

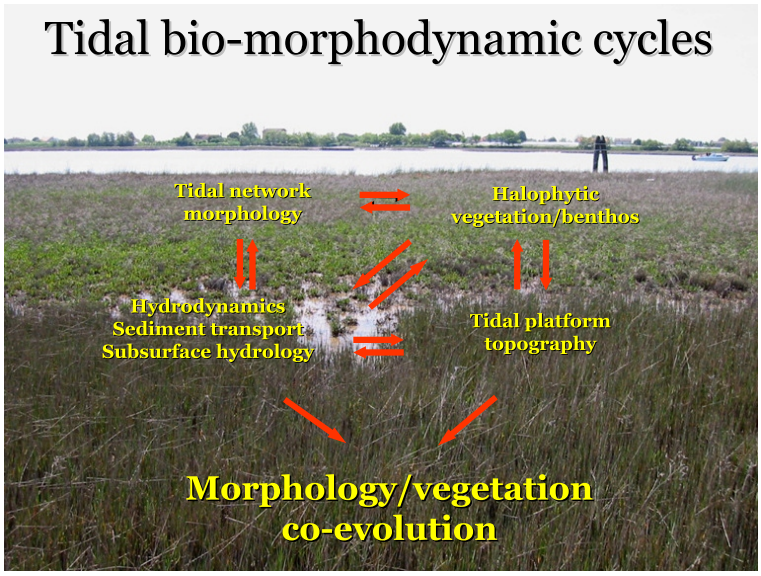

Figure 2.1: Eco-geomorphological interactions of halophytes in coastal environments.

also adversely impacting agricultural production and ecosystem services at an alarming rate (Larcher, 2003; Paranychianakisa & Chartzoulakisb, 2005; Chaves et al., 2009; Geissler et al., 2009; Runyan & D'Odorico, 2010; Gran et al., 2011). Additionally, the dynamics of coastal bio-geomorphic systems such as estuaries and lagoons worldwide depends on halophytic vegetation responses to salt and water-logging stresses (Fig. 2.1), further contributing to the global relevance of understanding salinity effects on plant functioning (Marani et al., 2007a; Gedan et al., 2009).

Exposure to salt stress involves complex changes in plant morphology, physiology, and metabolism (Fig. 2.2) and a large number of studies have focused on salt stress effects on plant growth, leaf photosynthetic rates, CO_2 fixation capacity, and leaf stomatal conductance (Yeo et al., 1985; Chaves et al., 2009). In this Chapter an optimization model to address how salt stress impacts the linkages between leaf photosynthesis, conductance, and transpiration rates will be developed. More specifically, the trade-offs be-

tween leaf carbon gains and water losses are explored when salt stress is increased.

Models describing leaf photosynthesis and water uptake under water limitations and, to a lesser extent, salt stresses, are numerous but can be grouped into three main categories. The first category includes detailed hydro-mechanical descriptions of stomatal movement (Dewar, 2002; Buckley et al., 2003), requiring the specification of a set of parameters rarely accessible in practical hydrologic and biogeochemical applications. The second category is composed of semi-empirical models that reduce stomatal conductance according to a stress level (Jarvis, 1976), or relate stomatal conductance to photosynthesis through a humidity index (Collatz et al., 1991; Leuning, 1995). The third category, which is extended here to the case of salinity stress, retains the key physiological mechanisms employed by the previous two model categories, but replaces precise hydraulic and biochemical descriptions of stomatal aperture with an optimization hypothesis (Givnish & Vermeij, 1976; Cowan & Farquhar, 1977; Hari et al., 1986).

The implications of increased salt stress on CO_2 uptake and water vapor exchange rates, especially under elevated atmospheric CO_2, has resisted an exhaustive theoretical treatment. While the effects of increased salinity on stomatal conductance are established (Downton et al., 1985; Delfine et al., 1999; Loreto et al., 2003; Flexas et al., 2004; Parida et al., 2004; Geissler et al., 2009), its effects on mesophyll conductance are typically not accounted for in existing models and have been less extensively studied (Ball & Farquhar, 1984; Brugnoli & Lauteri, 1991; Centritto et al., 2003). This knowledge gap is partly due to the frequent use of conventional gas exchange measurements that do not resolve chloroplast CO_2 concentration (c_c) and assume it to be identical to the intercellular CO_2 concentration (c_i). However, recent experiments unambiguously point to the fact that the mesophyll conductance in some plants is significantly modified by morpho-

logical changes brought about by increased salinity (Longstreth et al., 1984; Bongi & Loreto, 1989; Delfine et al., 1998; Parida et al., 2003).

This evidence is often interpreted by looking at the leaf-level CO_2 flux (f_c) vs. c_i (and c_c when inferred separately from c_i). For the $f_c - c_i$ relationship, the initial slope is significantly affected by salinity, whereas in the $f_c - c_c$ case, the initial slope does not seem to exhibit any change (Ball & Farquhar, 1984; Brugnoli & Lauteri, 1991; Delfine et al., 1998). Moreover, the c_c/c_i is relatively invariant to increasing f_c in control leaves, while it decreases with increasing f_c in salt-stress conditions. This decline in c_c/c_i emphasizes the role of reduced mesophyll conductance in saline conditions. Changes in the stomatal and mesophyll conductances, rather than in the stomatal conductance alone, are thus jointly responsible for changes in f_c and c_c (Figure 2.3).

The possible compound effects of salinity and elevated ambient CO_2 concentrations on gas exchange rates have not been extensively explored in earlier studies. Nicolas et al. (1993) and Geissler et al. (2009) do report some experimental results, which suggest a positive compensation effect with elevated atmospheric CO_2 concentrations with respect to salt stress. The quantification of the magnitude of such compensation mechanism is clearly of interest for climate change scenarios in saline environments.

The direct effects of salt stress on the photosynthetic machinery are also not fully established and are seldom included in plant-atmosphere gas exchange models (Flexas et al., 2004; Geissler et al., 2009), even though some studies do point out to significant changes in the photosynthetic capacity (Ball & Farquhar, 1984; Seemann & Sharkey, 1986; Bongi & Loreto, 1989; Paranychianakisa & Chartzoulakisb, 2005) associated with increased salinity. Hence, salt stress simultaneously affects stomatal and mesophyll conductances as well as photosynthetic efficiency, and their interrelations must be accounted for in quantitative models of plant responses to salinity.

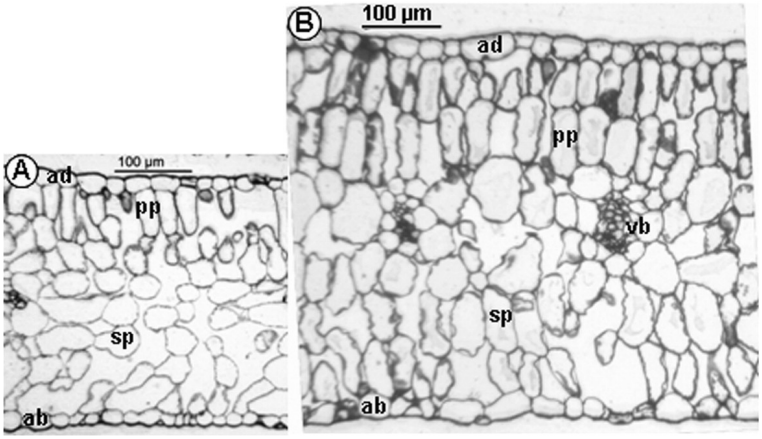

(a)

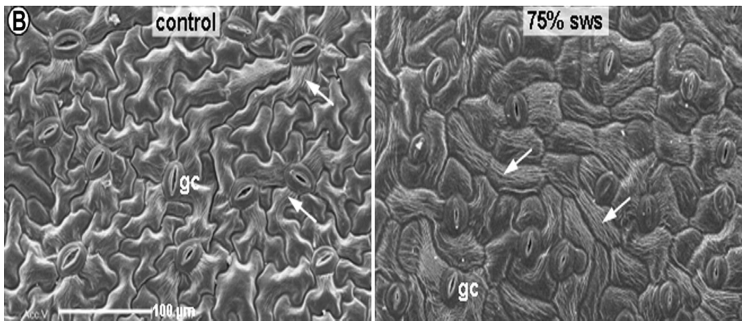

(b)

Figure 2.2: Effect of NaCl salinity on photosynthesis in *Aster ripolium L.* (a): Cross-sections of leaves, control on left panel, 75% sws (seawater salinity) on right panel. (b): Stomata of controls and of plants grown at 75% sws. From Geissler et al. (2009)

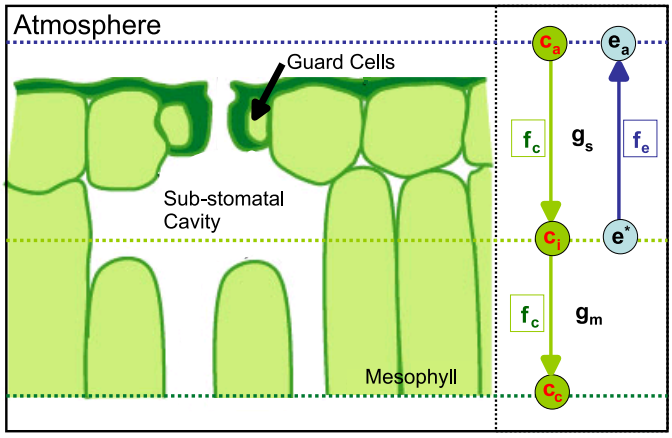

Figure 2.3: Schematic representation of mass exchange between the leaf and the atmosphere. The mesophyll and intercellular cavity are shown, and CO_2 and water vapor fluxes (f_c and f_e) are indicated on the right side.

It is these inter-relationships and how they may be accounted for in quantitative models that frames the scope of the present work. To progress on these issues, this work addresses three inter-related questions:

1) What are the effects of saline stress on photosynthesis and how can these effects be partitioned among stomatal conductance, mesophyll conductance, and photosynthetic capacity if the stomatal aperture is regulated so as to maximize carbon gain at a given water loss?

2) Is this proposed model able to describe gas exchange experiments in general and the relationship between stomatal and mesophyll conductances in particular?

3) What hypotheses can be generated from such a model about the joint effects of salinity and elevated atmospheric CO_2 on photosynthesis and stomatal conductance?

To address these questions, a stomatal optimization approach that maximizes carbon gain at a given water loss to describe stomatal operation under saline conditions is extended by accounting for the mesophyll con-

ductance. The resulting model explicitly predicts the functional relationship between stomatal and mesophyll conductances in response to changes in salinity thereby allowing direct evaluation against published data sets. The findings from this work can be imminently incorporated into soil-plant-atmosphere models dealing with salinity effects on land-surface fluxes of CO_2 and water vapor.

2.2 Methods

Basic definitions employed in stomatal optimization theories that maximize carbon gain for a given water vapor loss are first reviewed. Next, I describe how salt stress modifies this conventional picture. Published gas exchange experiments on two C_3 species with mild to intermediate salt tolerance are then used to explore the proposed modifications. The overall aim here is to disentangle salinity effects on photosynthetic properties versus gas diffusional limitations arising from reduced stomatal and mesophyll conductances.

2.2.1 Extending Stomatal Optimization Theories to Saline Environments

The bulk transfer rates of CO_2 and water vapor across the leaf stomata are given as:

$$f_c = g_s(c_a - c_i) \tag{2.1}$$

$$f_e = a g_s VPD \tag{2.2}$$

where f_c (μmol m^{-2} s^{-1}) and f_e (mol m^{-2} s^{-1} kPa) are the leaf-level CO_2 and water vapor fluxes, g_s is the CO_2 stomatal conductance (mol m^{-2} s^{-1}), c_a and c_i are the ambient and the intercellular CO_2 concentrations (μmol

mol^{-1} or ppm), respectively, $a = 1.6$ is the relative molecular diffusivity of water vapor with respect to carbon dioxide, $VPD = e^*(T_a)(1 - RH)$ is the vapor pressure deficit (kPa) assuming the leaf is well coupled to the atmosphere (as is the case for virtually all gas-exchange measurements), $e^*(T_a)$ is the saturation vapour pressure (a function of air temperature, T_a, given by the Clausius-Clapeyron equation), and RH is the mean air relative humidity (expressed as a fraction). The VPD can also be expressed as dimensionless fraction when normalized by the atmospheric pressure. In this dimensionless representation for VPD, the units of f_e are altered accordingly.

In the conventional stomatal optimization theory originally proposed by Givnish & Vermeij (1976) and Cowan & Farquhar (1977) and subsequently employed in other studies (Hari et al., 1986, 1999, 2000; Berninger & Hari, 1993; Arneth et al., 2002; Katul et al., 2009, 2010; Manzoni et al., 2011; Boer et al., 2011), a leaf autonomously maximizes the rate of carbon uptake subject to a constraint (or cost) imposed by the concurrent water vapor loss. Hence, the stomatal conductance (or, more precisely, the stomatal aperture) adjusts so as to maximize an objective function given as:

$$F = f_c - \lambda f_e. \tag{2.3}$$

The cost parameter, λ, is conventionally labeled as the marginal water use efficiency. With respect to the conventional definition of water use efficiency WUE $= f_c/f_e$, the marginal water use efficiency refers to the variations of the fluxes with respect to the variation in stomatal conductance (marginal WUE $= \lambda = \frac{\partial f_c/\partial g_s}{\partial f_e/\partial g_s}$).

When these expressions are combined with the photosynthetic demand function given by the Farquhar photosynthesis model (Ball & Farquhar, 1984), the maximization of equation (2.3) leads to a parsimonious formulation for the stomatal conductance (Hari et al., 1986, 1999, 2000; Berninger & Hari, 1993; Lloyd & Farquhar, 1994; Arneth et al., 2002; Katul et al.,

2009, 2010; Manzoni et al., 2011; Boer et al., 2011). This formulation is particularly convenient for use in large-scale hydrological and climate models, where several coupled phenomena are typically considered (e.g., mass and energy transport in the atmosphere and in the soil).

This formulation must now be modified to account for salt stress and, in particular, for the changes induced by salinity to the mesophyll conductance as well as to the photosynthetic efficiency (Volpe et al., 2011b). Because f_c occurs inside the chloroplast, eq. (2.1) describing the CO_2 flux must be revised to explicitly consider c_c and the mesophyll conductance, g_m, characterizing CO_2 transport from the intercellular space to the chloroplast (Figure 2.3). The effective conductance, g_{eff}, associated with the series of conductances, g_m and g_s, leading from the chloroplast to the atmosphere as shown in Figure 2.3 is given by

$$g_{eff} = \frac{g_s\, g_m}{g_s + g_m}. \tag{2.4}$$

The rate of CO_2 uptake in eq. (2.1) is now modified as

$$f_c = g_{eff}(c_a - c_c). \tag{2.5}$$

When leaf respiration is small compared to f_c, f_c can be approximated as the total biochemical demand for CO_2 occurring in the chloroplast, which can be expressed as (Farquhar et al., 1980)

$$f_c = \frac{a_1(c_c - c_p)}{a_2 + c_c}, \tag{2.6}$$

where c_p is the CO_2 compensation point and a_1 and a_2 are physiological parameters depending on whether the photosynthetic rate is restricted by electron transport or by Rubisco. Under light-saturated conditions, $a_1 = V_{cmax}$, the maximum carboxylation capacity of Rubisco, and $a_2 = K_c(1 + C_{oa}/K_o)$, where K_c and K_o are the Michaelis constants for CO_2 fixation and

oxygen inhibition, and C_{oa} is the oxygen concentration in the atmosphere. When light is limiting, $a_1 = \alpha_p e_m Q_p = \gamma Q_p$ and $a_2 = 2c_p$, where α_p is the leaf absorptivity of photosynthetically active radiation ($= Q_p$), e_m is the maximum quantum efficiency of leaves and γ is the apparent quantum yield determined from empirical light-response curves. The parameters necessary to compute c_p and a_2 were taken from Farquhar et al. (1980) and adjusted for temperature according to Campbell & Norman (1998) (eq. 14.26 and following, pages $240 - 241$).

By equating the transport rate of CO_2 given by eq. (2.5) to the biochemical demand in eq. (2.6), an expression for the ratio (c_c/c_a) can be derived and is given as

$$\frac{c_c}{c_a} = \frac{1}{2} + \frac{-a_1 - g_{eff}a_2 + \sqrt{\left[a_1 + g_{eff}(a_2 - c_a)\right]^2 + 4g_{eff}(a_1 c_p + g_{eff}c_a a_2)}}{2g_{eff}c_a}. \tag{2.7}$$

When substituted back into eq. 2.5, an expression for f_c is obtained,

$$f_c = \frac{1}{2}\left[a_1 + g_{eff}(a_2 + c_a) - \sqrt{\left[a_1 + g_{eff}(a_2 - c_a)\right]^2 + 4g_{eff}(a_1 c_p + g_{eff}c_a a_2)}\right]. \tag{2.8}$$

Using expressions (2.8) and (2.2), the objective function to be maximized with respect to stomatal conductance can be re-formulated (F from eq. (2.3)). This maximization condition results in

$$\frac{\partial F}{\partial g_s} = \frac{1}{2}\left[(a_2 + c_a)\frac{g_m^2}{(g_s + g_m)^2} - 2\lambda a VPD + \frac{\frac{g_m^2}{(g_s+g_m)^2}a_1(-2c_p + c_a - a_2) - \frac{g_m g_s}{(g_s+g_m)}\frac{g_m^2}{(g_s+g_m)^2}(a_2 + c_a)^2}{\sqrt{\left[a_1 + g_{eff}(a_2 - c_a)\right]^2 + 4g_{eff}(a_1 c_p + g_{eff}c_a a_2)}}\right] = 0, \tag{2.9}$$

This equation can be readily solved numerically to obtain g_s and, hereafter, this solution will be called the non-linear model, because it accounts

Table 2.1: List of symbols. Non-stressed and salt-stressed plants are indicated by subscripts ns and s, respectively. Note that when dividing f_e by the atmospheric pressure (in kPa), the usual units of mol m^{-2} s^{-1} are recovered.

Symbol	Description	Units
f_c	Net CO_2 assimilation	μmol m^{-2} s^{-1}
f_e	Rate of transpiration	mol m^{-2} s^{-1} kPa
g_s	Stomatal conductance to CO_2	mol m^{-2} s^{-1}
g_m	Mesophyll conductance to CO_2	mol m^{-2} s^{-1}
c_a	Atmospheric CO_2 concentration	μmol mol^{-1}
c_i	Intercellular CO_2 concentration	μmol mol^{-1}
c_c	Chloroplast CO_2 concentration	μmol mol^{-1}
a	Ratio of H_2O to CO_2 diffusivities (= 1.6)	-
VPD	Vapour pressure deficit	kPa
λ	Cost parameter	μmol mol^{-1} kPa^{-1}
a_1	Kinetic constant for photosynthesis	μmol m^{-2} s^{-1}
a_2	Half saturation constant for photosynthesis	μmol mol^{-1}
c_p	Compensation point	μmol mol^{-1}

for all the non-linearities in the biochemical demand function.

2.2.2 A linearized model

For more immediate interpretations of published gas exchange measurements, and for simpler implementations in eco-hydrologic models, a linearized analytical expression for conductance and photosynthesis is also developed here and compared with the non-linear model. This simpler analytical expression for g_s can be obtained by simplifying the denominator of the biochemical demand function (eq. (2.6)) as:

$$a_2 + c_c = a_2 + \left(\frac{c_c}{c_a}\right) c_a = a_2 + s c_a, \tag{2.10}$$

where the variability in $s = c_c/c_a$ is assumed to be small compared to the magnitude of a_2 such that s can be treated as approximately constant (Katul et al., 2000, 2010). It must be emphasized here that s is treated as a model constant only in eq. (2.10), i.e. in the denominator of eq. (2.6) while in eq. (2.5) describing the rate of CO_2 uptake, c_c/c_a is allowed to vary. The premise here is that a_2 is usually larger than sc_a and variations introduced by s do not significantly impact their sum. This linearized biochemical demand is now given as

$$f_c = \frac{a_1(c_c - c_p)}{a_2 + sc_a}, \tag{2.11}$$

where, despite the linearization, f_c retains the saturating behavior with increasing c_a. By combining the rate of CO_2 uptake (eq. (2.5)) and the linearized biochemical demand function (eq. (2.11)), the chloroplast concentration is given as

$$c_c = \frac{a_1 c_p + g_{eff} c_a (a_2 + sc_a)}{a_1 + g_{eff}(a_2 + sc_a)}, \tag{2.12}$$

and by substituting into eq. (2.5), f_c is readily expressed as

$$f_c = \frac{g_{eff} a_1 (c_a - c_p)}{a_1 + g_{eff}(a_2 + sc_a)}, \tag{2.13}$$

which can now be used in defining the objective function F (eq. (2.3)).

Upon differentiation with respect to g_s and by setting $\frac{\partial F}{\partial g_s} = 0$, an analytical solution for g_s can be derived as

$$g_s = \frac{a_1 g_m}{a_1 + g_m(a_2 + sc_a)} \left(-1 + \sqrt{\frac{c_a - c_p}{a\lambda VPD}} \right). \tag{2.14}$$

By combining eq. (2.14) with eq. (2.13), an expression for the photosynthetic rate as a function of the mesophyll conductance is obtained,

$$f_c = \frac{a_1 g_m (c_a - c_p)}{a_1 + g_m(a_2 + sc_a)} \left(1 - \sqrt{\frac{a\lambda VPD}{c_a - c_p}} \right). \tag{2.15}$$

Finally, rearranging eq. (2.14) and eq. (2.15) yields an explicit expression for the CO_2 flux,

$$f_c = g_s\sqrt{a\lambda VPD(c_a - c_p)}. \tag{2.16}$$

Hereafter, this solution will be labeled as the linear model.

The use of eqs. (2.9) and (2.14) clearly requires either calibrating λ based on measurements (later described) or adopting independent estimates. Atmospheric CO_2 concentration has been shown to affect the value of λ. A linear dependence may be assumed (Katul et al., 2010; Manzoni et al., 2011),

$$\lambda = \lambda_o c_a/c_o, \tag{2.17}$$

where c_o is a reference CO_2 concentration for which $\lambda = \lambda_o$ is known. If this linear expression for λ is adopted, and upon neglecting variations in c_p compared to c_a, the canonical form of the g_s versus f_c relationship reduces to

$$g_s \approx m_1(f_c/c_a)(VPD)^{-1/2}. \tag{2.18}$$

This mathematical form is virtually identical to the Ball-Berry and Leuning semi-empirical models (Collatz et al., 1991; Leuning, 1995) with three exceptions: (1) this canonical form is an *emergent property* of the linear optimality model, not *a priori* assumed as was the case in the Ball-Berry and Leuning models (Collatz et al., 1991; Leuning, 1995); (2) the $VPD^{-1/2}$ reduction function is also an *emergent property* of the optimization theory and is not empirically assumed as noted elsewhere (Hari et al., 1986; Katul et al., 2009); and (3) the stomatal sensitivity parameter $m_1 = \sqrt{c_o/(a\lambda_o)}$ can be explicitly related to the marginal water use efficiency λ_o reflecting CO_2 conditions during plant growth.

2.2.3 Data

Both the non-linear and the linear optimality models are used to interpret published gas exchange measurements for salt stressed plants. After a literature review, two studies were identified involving simultaneous measurements of the CO_2 flux and stomatal and mesophyll conductances for controlled and salt-stressed conditions.

The first dataset, published by Loreto et al. (2003) and digitized by us for this work, refers to experiments in which olive trees (*Olea europea*) were irrigated with water while gradually increasing salinity (up to 200 mM, resulting in a water electrical conductivity of 24.6 dS m^{-1}). Simultaneous gas-exchange and fluorescence field measurements were carried out on six different cultivars known to have moderate salt tolerance. The measurements were performed between 40 and 45 days after the beginning of the salt treatment and included stomatal conductance, photosynthesis and chlorophyll fluorescence under ambient air temperature (28-30° C), light intensity (800-1000 μmol photons $m^{-2}s^{-1}$, corresponding to saturating light conditions (Bongi & Loreto, 1989)), and VPD (< 2 kPa).

The second dataset (Delfine et al., 1998, 1999) refers to irrigation experiments performed on spinach plants (*Spinacia oleracea*), displaying intermediate sensitivity to salt stress. The control setup was irrigation with freshwater, while a subset of the plants were irrigated with saline water (1% NaCl w/v= 200 mM). Plants were grown in a greenhouse under controlled temperature and light conditions. Sampling commenced 13 days after the first saline irrigation and continued once a week until flowering. The mean leaf temperature was 25° C and the light intensity was 1200 μmol quanta $m^{-2}s^{-1}$, also in this case close to light saturation conditions (Calatayud et al., 2003; Yamori et al., 2005).

The gas exchange measurements considered here were performed well after the start of the salt treatment. It is safe to assume that the salt

concentration in the tissues in all cases exceeded a threshold beyond which salinity induced significant physiological responses. The behavior of the two contrasting end-members sets (non-stressed and salt-stressed plants, indicated by subscripts ns and s, respectively) are considered for simplicity. Mesophyll conductances and chloroplast concentrations were retrieved using methods described elsewhere (Loreto et al., 1992; Harley et al., 1992). Since both *S. oleracea* and *O. europea* are C_3 species (Schnarrenberger et al., 1980; Camin et al., 2010), eq. (2.6) can be used to model the biochemical demand for CO_2. Light-saturated conditions were assumed in all cases, noting the high light intensity measured in the two experiments.

2.3 Results

2.3.1 Comparison between linear and non linear models

In this section the two models are compared. Fig.s 2.4 and 2.5 show the shape of the objective function F (eq. (2.3)) and its derivative with respect to g_s for two different values of the mesophyll conductance g_m for $\lambda = 0.1c_a$ (with $c_a = 380\ ppm$). It can be noticed that, in both cases, the value of g_s for which the derivative of the objective function is zero, is different for the original model and its linearized version.

Fig. 2.6 shows the behaviour of the two models. For fixed values of the mesophyll conductance, g_m, the stomatal conductance, g_s, is obtained numerically for the non linear model and analytically with eq. 2.14 for the linearized version. Again, the difference between the two is quite clear.

Therefore, it seems that the values of λ are not equal for the original model (λ_{nl}) and for the linearized one (λ_{lin}). Fig. 2.7 shows the λ_{lin} values obtained by fixing the λ_{nl} and by imposing the stomatal conductance derived from the linearized model to be equal to the one obtained from the non linear one, for fixed g_m values. This was performed for different g_m values and for

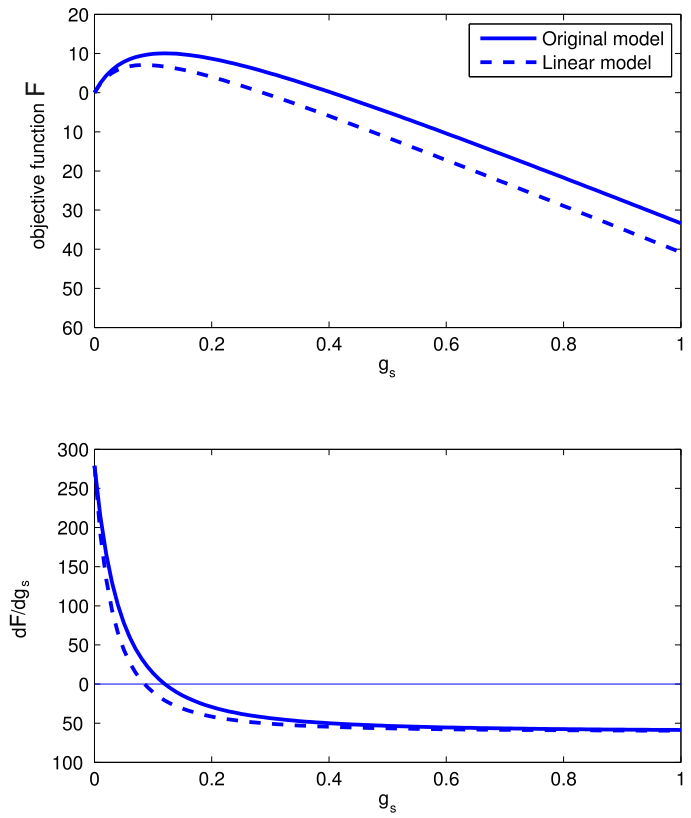

Figure 2.4: Objective functions and their derivatives for $gm = 0.1\ mol/m^2 s$

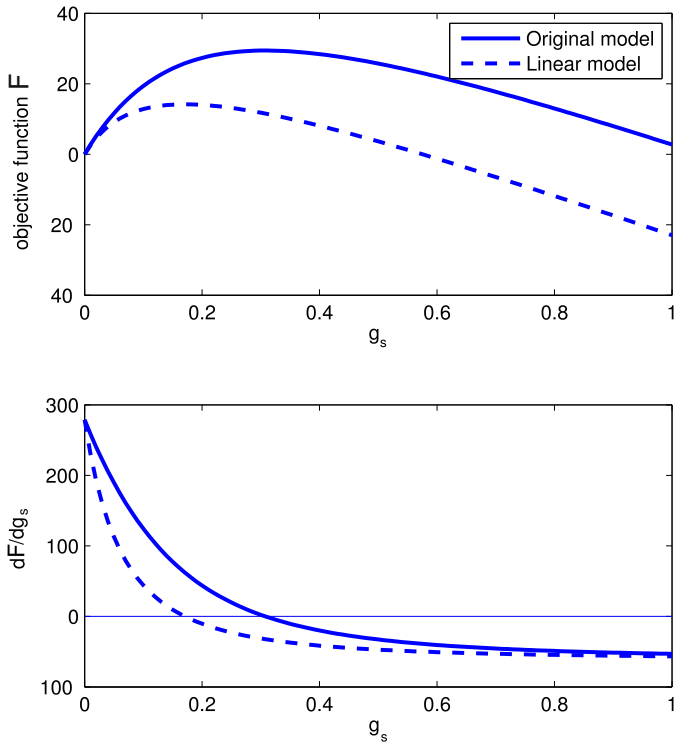

Figure 2.5: Objective functions and their derivatives for $gm = 0.5\ mol/m^2s$

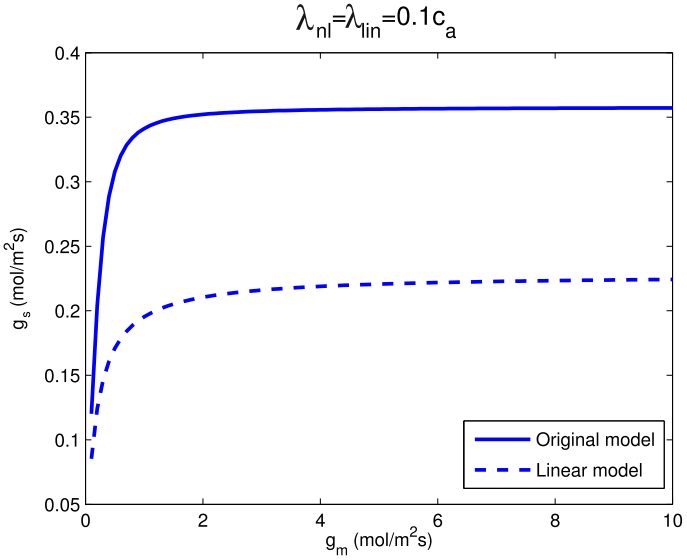

Figure 2.6: Comparison between g_s obtained with the original model and the linearized one for $\lambda = 0.1c_a$.

a range of $\lambda_{nl} = 0 - 380\ \mu mol/mol\ KPa$.

In Fig. 2.8 the relationship between λ_{lin} and λ_{nl} is shown. Values of λ between $0 - 100\ \mu mol/mol\ KPa$ are considered, as commonly found in the literature, and g_m between $0.1 - 5\ mol/m^2 s$ for the same reason. From a least squares regression with intercept equal to zero, one finds:

$$\lambda_{lin} = 0.5563\lambda_{nl}. \tag{2.19}$$

The application of 2.19 to the previous graphs yields the results showed in figg. 2.9, 2.10 and 2.11.

The sensitivity of λ to salinity is also confirmed by other analyses performed. Indeed, rearranging the results from the linear model (Section 2.2.2), the following expression is obtained:

$$\frac{c_i}{c_a} = \frac{c_p}{c_a} + \frac{(c_a - c_p)}{c_a}\left[1 - \sqrt{\frac{a\lambda\ VPD}{c_a - c_p}}\right]. \tag{2.20}$$

Isolating λ allows to investigate its variations with increasing salinity:

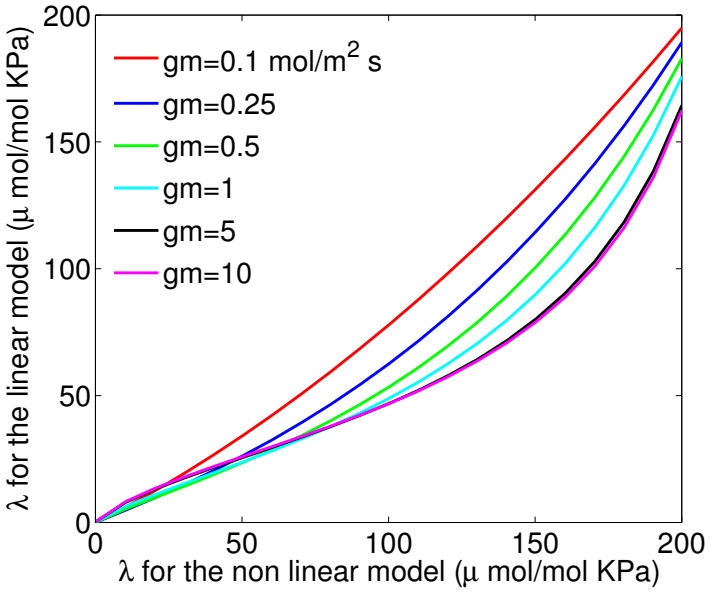

Figure 2.7: λ_{nl} versus λ_{lin} for different g_m values.

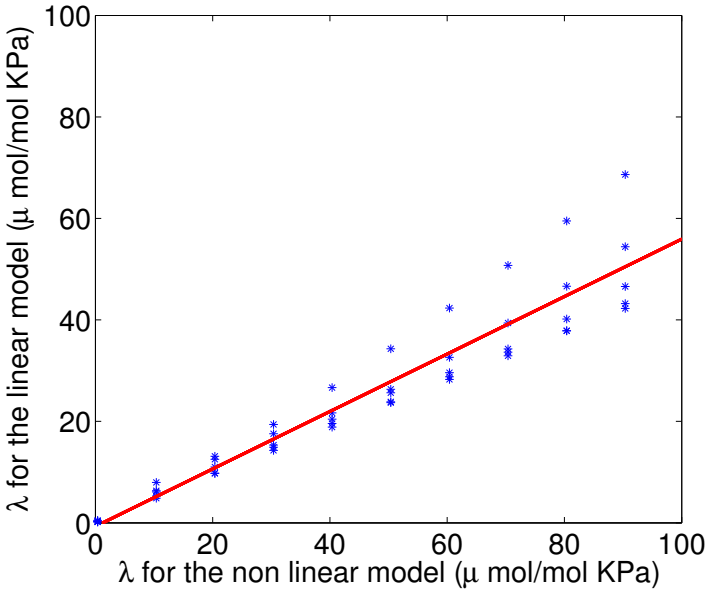

Figure 2.8: Relationship between λ_{nl} and λ_{lin}.

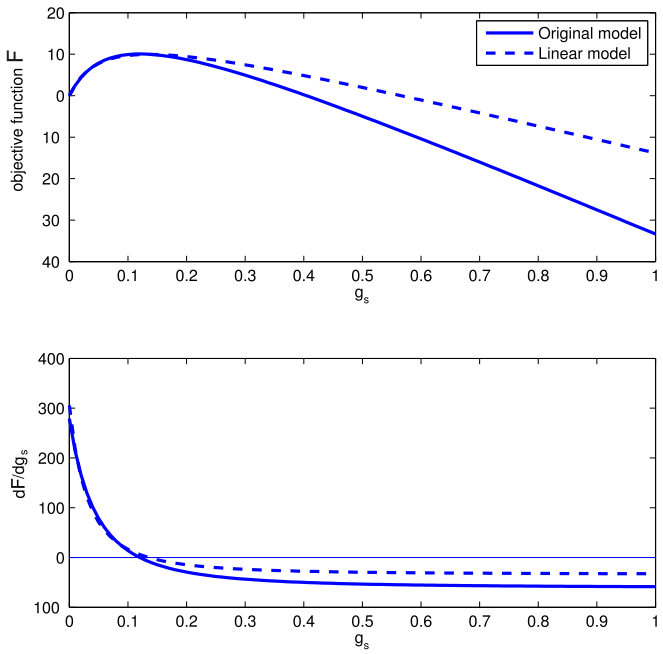

Figure 2.9: Corrected objective functions and their derivatives for $gm = 0.1\ mol/m^2 s$

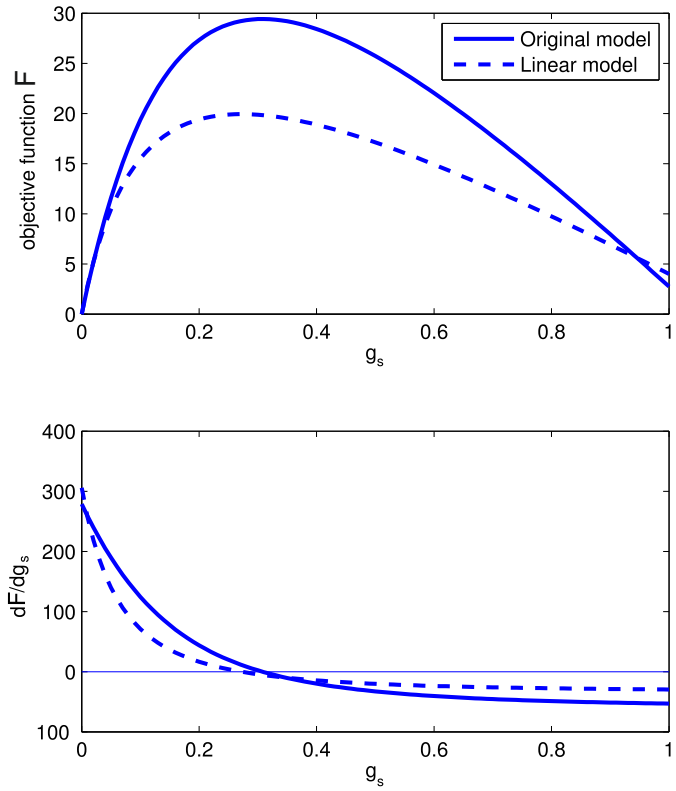

Figure 2.10: Corrected objective functions and their derivatives for $gm = 0.5\ mol/m^2 s$

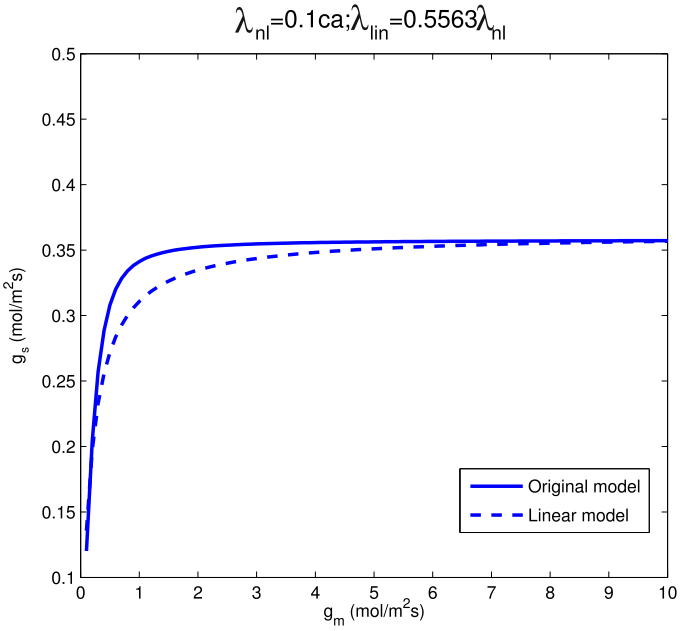

Figure 2.11: Comparison between g_s obtained with the original model and the linearized one by correcting λ_{lin} with eq. 2.19.

$$\lambda = \frac{(c_a - c_i)^2}{(c_a - c_p)a\ VPD}. \tag{2.21}$$

The results for two types of plants with different salt tolerance are shown in Figure 2.12. Fig. 2.12(a) shows the results for olive plants (Bongi & Loreto, 1989), for two different measured VPD values (10 and 30 mPa/Pa), while Fig. 2.12(b) shows the results for the more tolerant mangroves (Ball & Farquhar, 1984). λ increases with salinity for all VPD values in the olive case, while it exhibits negligible changes in the case of the salt-tolerant mangroves.

A conventional sensitivity analysis was also performed on the model parameters in eq. (2.14) (a_1, a_2, λ and c_p). The stomatal conductance in reference conditions was first computed. We then increased/decreased the value of each of the 4 parameters, one at a time, by $\pm 50\%$. The variation of the resulting value of stomatal conductance was then explored. Such

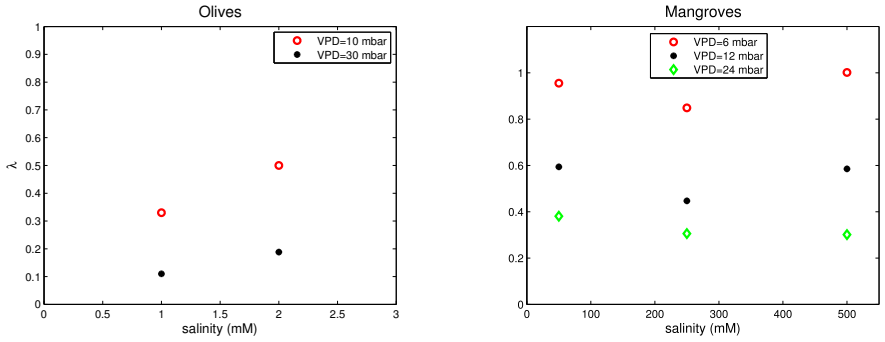

(a) (b)

Figure 2.12: Relationship between λ and salinity for olives (a) and mangroves (b).

variation was evaluated by the Condition Number (CN):

$$CN = \frac{g_s - \hat{g}_s}{\hat{g}_s} \frac{1}{0.5}, \tag{2.22}$$

where g_s is the stomatal conductance value after the parameter's variation, $\hat{g}_s$ is the reference value and 0.5 is the variation applied (50% in this case). The results clearly show that the model is far more sensitive to the parameters a_1 and λ (Figure 2.13).

These results are in agreement with what is reported in previous literature, which suggests that the compensation point c_p is not affected by salinity (Ball & Farquhar, 1984; Longstreth et al., 1984).

2.3.2 Model calibration

Following the sensitivity analysis described in the previous Section, two parameters (a_1 and λ) were identified as most significantly controlling the behaviour of the non-linear and linear optimality models and serve as logical candidates for assessing how salinity affects their values. Any salt stress effect on a_1 is here interpreted as impacting the photosynthetic efficiency of the plant, while salinity effects on λ are interpreted as impacting the stomatal regulation. Both parameters have been computed through non-

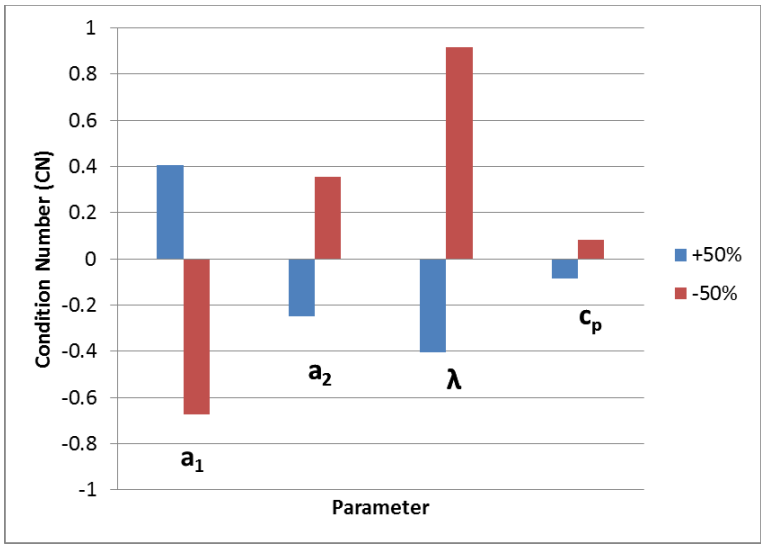

Figure 2.13: Result of the sensitivity analysis.

linear fitting to the data of the linearized and nonlinear model equations developed in Section 2.2, as discussed next.

In the nonlinear model, a_1 was computed by fitting the non linear model for f_c (eq. (2.8)) to the simultaneously measured values of f_c, g_s, and g_m (the latter two are always combined in g_{eff}) using a Root Mean Square Error (RMSE) minimization between modeled and observed values of f_c, which provided a satisfactory agreement both for the freshwater and the salt-stressed cases and for both datasets.

Figures 2.14(a) and 2.14(b) show measured versus modelled photosynthetic rates (eq. (2.8)), and a satisfactory agreement is obtained both for the freshwater and salt-stressed cases and for both datasets, providing confidence in the ability of the model to describe the plants' physiological responses in the presence and absence of salt stress.

For the olive trees dataset, the optimized values for a_1 in non-saline and in salt-stressed conditions were respectively $a_{1,ns} = 61.55$ μmol m^{-2}s^{-1} and $a_{1,s} = 38.21$ μmol m^{-2}s^{-1} (recall subscripts ns and s indicate unstressed control and salt-stressed plants). Hence, salt stress reduced a_1 by some 40%

from its non-saline value. In the case of the spinach dataset, the results of the calibration were: $a_{1,ns} = 127.25$ μmol $m^{-2}s^{-1}$ and $a_{1,s} = 87.36$ μmol $m^{-2}s^{-1}$, again suggestive of some 30% reduction due to salt stress. Hence, these model calculations show that the photosynthetic efficiency is significantly reduced by salt stress in both cases.

Using a numerical procedure based on the combination of two algorithms (the simplex search method of Lagarias et al. (1998) and the trust-region-reflective algorithm described in Coleman & Li (1994, 1996)) to iteratively solve the non-linear objective function (eq. (2.9)), the value of λ was determined by minimizing the RMSE between measured and modeled g_s. Figures 2.14(c) and 2.14(d) compare measured and modelled stomatal conductance values, again showing a good agreement. For the olive trees dataset, the computed λ for the non-saline and the salt-stressed condition, were respectively: $\lambda_{ns} = 1.64$ ppm/kPa and $\lambda_s = 8.07$ ppm/kPa. For the spinach dataset, $\lambda_{ns} = 8.00$ ppm/kPa and $\lambda_s = 14.35$ ppm/kPa. Again, in all cases, the results appear consistent with intuitive expectations: λ increases with increased salt stress, indicating that the cost per unit mass of water transpired increased with increased salinity (analogous to worsening plant water status during soil moisture stress). Figure 2.15 illustrates the dependence of f_c on g_s and g_m using the observed values for g_m, the values of g_s obtained from the optimality model (eq. (2.9)), and the values of f_c determined from eq. (2.8). The shape of the modelled relationships are remarkably consistent with the dataset considered for g_m. The relationship between f_c and g_s is almost linear for olives and spinach, while f_c exhibits a nonlinear dependence on g_m with an asymptotic behavior.

While the non-linear model retains all the non-linearities of the biochemical demand function, it lacks the analytical tractability of the linearized model and does not allow an immediate understanding of the scaling relationships between fluxes and biological and environmental parameters. The

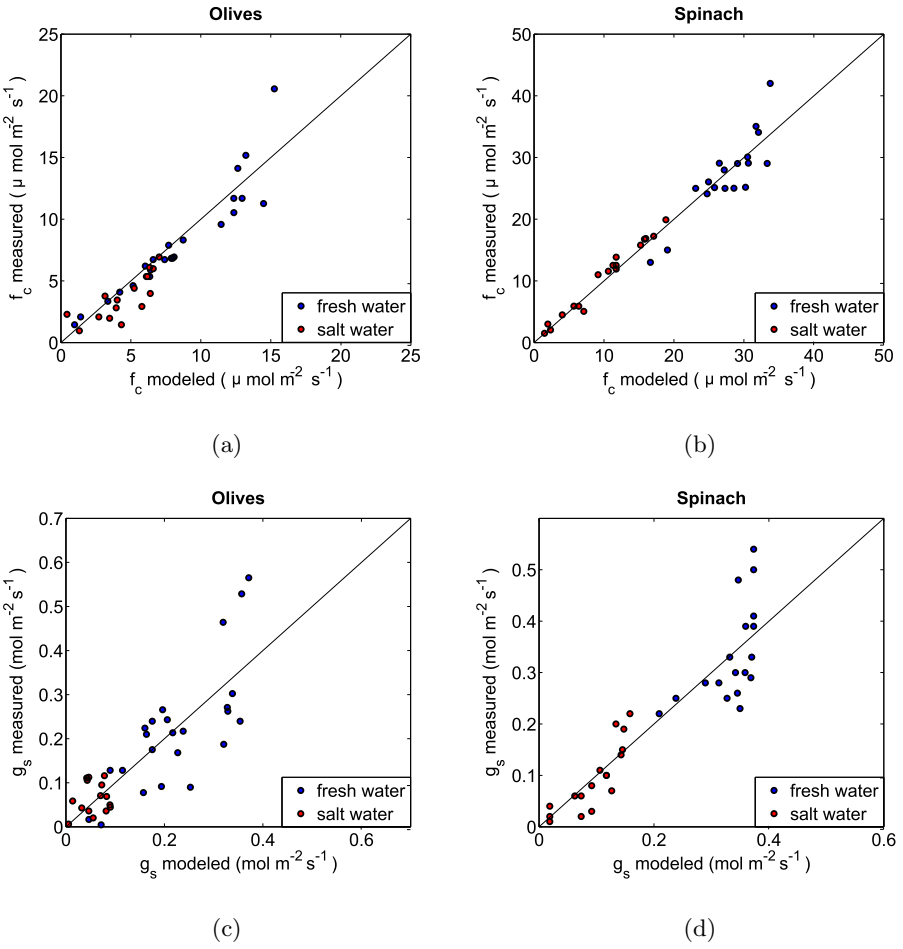

Figure 2.14: Comparison between measured and modeled photosynthesis and stomatal conductance using the non linear model for the olive trees and spinach plants. The solid line is the bisector of the axes.

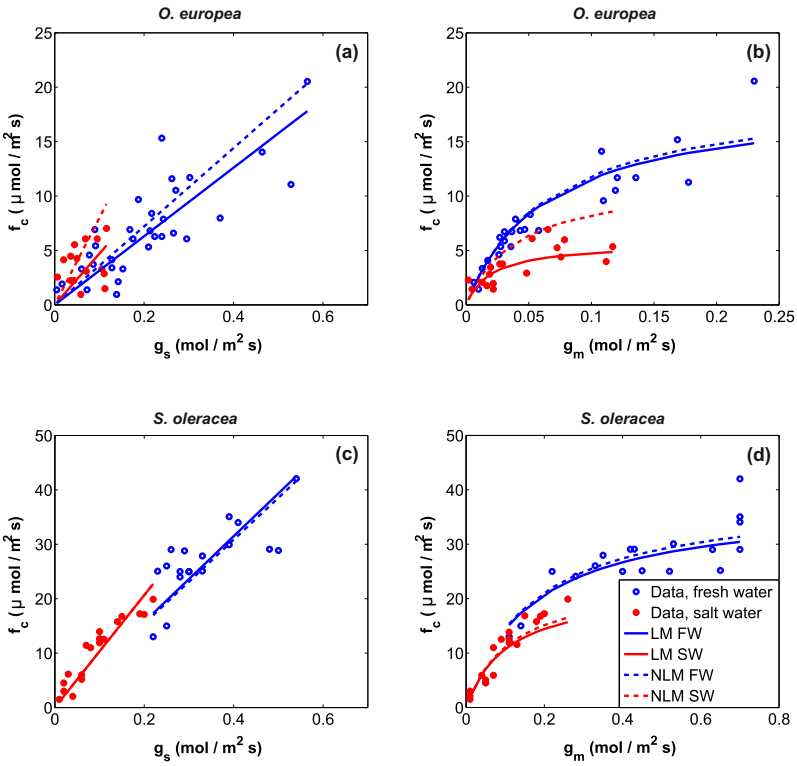

Figure 2.15: Comparison between measured and modeled f_c vs g_s (a) and (c) and f_c vs g_m (b) and (d) using the non-linear (NLM, dashed line) and linear (LM, solid line) models for the *O. europea* and *S. oleracea* data sets. Dots represent measurements, lines represent the model for the reference case (FW, blue) and for the salt-stressed case (SW, red).

linear model is also attractive for the estimation of a_1 and λ, as discussed next.

The value of $s = c_c/c_a$ employed in the linearization of the biochemical demand function (eqs. (2.10) and (2.11)), was retrieved for the two datasets from mean values of measured c_c and c_a. The inferred s from these data is higher for non-saline conditions (due to decreased g_m), ranging from 0.6 (non-saline) and 0.2 (salt-stress) for *S. oleracea* to 0.7 (non-saline) and 0.4 (salt-stress) for *O. europea*.

The calibration of λ for the linearized model is performed by minimizing the RMSE for f_c using the solution of eq. (2.16) (Figure 2.15). As noted earlier, the modelled relationship between f_c and g_s is approximately linear and consistent with the measurements, resulting in $\lambda_{ns} = 1.25$ ppm/kPa for the olive trees, and $\lambda_{ns} = 8.33$ ppm/kPa for spinach. As in the case of the non-linear model, the values of λ increase with salinity in both cases ($\lambda_s = 2.8$ ppm/kPa, for olive trees, and $\lambda_s = 14.34$ ppm/kPa for spinach).

Subsequently, using the expression for the photosynthetic rate as a function of the mesophyll conductance obtained from the linearized model (eq. (2.15)), the value of a_1 using the now determined value of λ was obtained. The resulting values of a_1 also decreased with salinity for the olive trees ($a_{1,ns} = 59.33$ μmol m^{-2}s^{-1}, $a_{1,s} = 18.80$ μmol m^{-2}s^{-1}) and the spinach plants ($a_{1,ns} = 122.60$ μmol m^{-2}s^{-1}, $a_{1,s} = 81.01$ μmol m^{-2}s^{-1}). The modelled relations between f_c and g_m (Figure 2.15) captured the observed patterns as well as the non-linear model.

The results of the model calibration are summarized in Table 2.2.

2.3.3 Parameter uncertainty

The values of a_1 and λ estimated using the linear and non-linear models are comparable for both species in the reference non-stressed cases. In the salt stress case, however, the values of λ and a_1 vary between the two models for

Table 2.2: Results of model calibration for non-saline and saline conditions, linear and non-linear models and both datasets.

	O. europea		***S. oleracea***	
	non-linear	**linear**	**non-linear**	**linear**
		NON-SALINE		
λ_{ns} (mol mol^{-1} kPa^{-1})	1.64	1.25	8.00	8.33
$a_{1,ns}$ (μmol m^{-2} s^{-1})	61.55	59.33	127.25	122.60
		SALT-STRESSED		
λ_s (mol mol^{-1} kPa^{-1})	8.07	2.80	14.35	14.34
$a_{1,s}$ (μmol m^{-2} s^{-1})	38.21	18.80	87.36	81.01

O. europea, possibly because of the narrow range covered by experimental values, which do not constrain the regression parameters as well as in the other cases (Figure 2.15(a) and (b)).

It is relevant to determine whether the differences in the parameters obtained in the salt-stress and non-stressed conditions are significant with respect to the population of possible parameter values arising from the observational scatter. To this end, a bootstrap resampling technique (Efron, 1979) was employed to retrieve the frequency distribution of the parameters involved in the calibration of both models. The bootstrap procedure is based on randomly selecting data from the original dataset (with replacement, i.e., potentially allowing the selection of the same data value multiple times), thereby generating a large number of new synthetic samples (here equal to 10,000) with the same size as the original one. The larger the number of resamplings, the more precise is the frequency distribution obtained, but this choice must allow reasonable computational time. The model is then calibrated for each synthetic sample, thus providing numerous estimates (10,000 in our case) of the parameters and allowing the construction of their frequency distribution in a non-parametric manner. The obtained

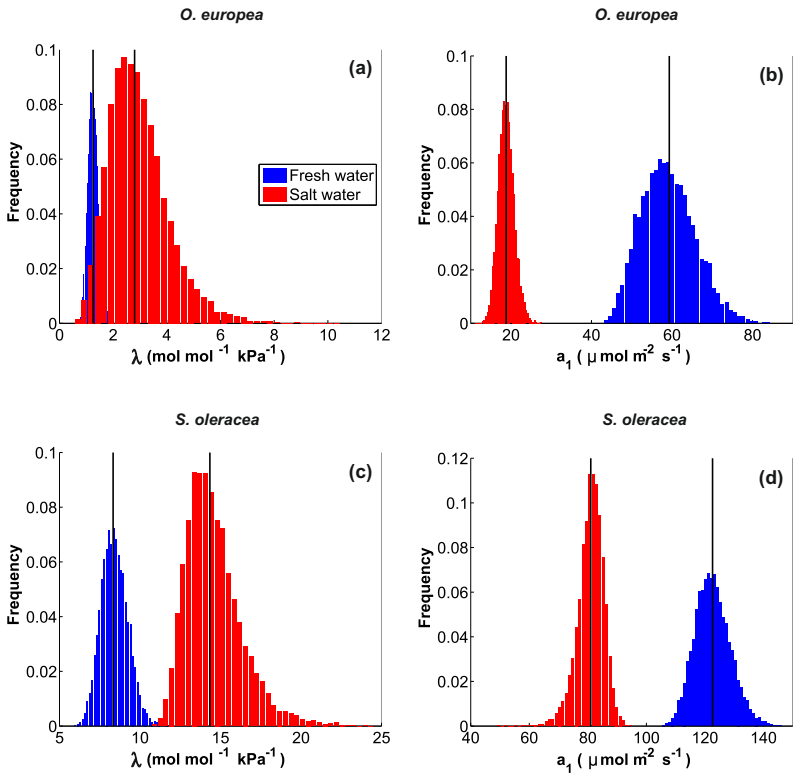

Figure 2.16: Frequency distributions of the calibrated parameters λ ((a) and (c)) and a_1 ((b) and (d)) derived with the *bootstrap* technique for the linearized model both for *O. europea* and *S. oleracea* datasets, and for fresh water (blue) and salt-stressed (red) case. Black bars indicate the calibrated values.

distributions (see Figure 2.16) display a marked separation, showing that indeed the differences between the values for control and salt-stressed treatments are statistically significant. The mean values of the distributions and the 95 % confidence intervals for both the linear and non-linear models are shown in Table 2.3.

A model validation was also performed using a Leave-One-Out Cross-Validation technique (Wilks, 2006). Validation could not be obtained by using two independent datasets (one for calibration and one for validation), be-

Table 2.3: Results of the model calibration for non-saline and saline conditions, linear and non-linear models and both datasets analyzed. The mean value of the derived frequency distribution and the 95% confidence intervals are also presented. [λ] in mol mol^{-1} kPa^{-1} and [a_1] inμmol m^{-2} s^{-1}.

		O. europea						***S. oleracea***					
		non-linear			**linear**			**non-linear**			**linear**		
		Model	Mean	95 % CI	Model	Mean	95 % CI	Model	Mean	95 % CI	Model	Mean	95 % CI
NON-SALINE	λ_{ns}	1.64	1.68	[1.29-2.13]	1.25	1.27	[0.98-1.61]	8.00	8.05	[6.90-9.31]	8.33	8.42	[7.17-9.79]
	$a_{1,ns}$	61.55	61.38	[50.13-74.04]	59.33	59.14	[49.32-70.24]	127.25	127.26	[116.49-139.08]	122.60	122.60	[113.51-132.82]
SALT-STRESSED	λ_s	8.07	8.21	[5.12-11.72]	2.80	3.01	[1.54-5.03]	14.35	14.60	[11.94-18.01]	14.34	14.66	[12.42-17.79]
	$a_{1,s}$	38.21	36.49	[5.58-72.58]	18.80	18.86	[15.74-22.19]	87.36	91.74	[22.6-134.08]	81.01	80.78	[73.16-87.06]

cause it would require two identical experiments employing the same plants and subjecting them to the same external conditions, meteorological forcings, and salinity levels. One possibility is dividing the data set into two smaller datasets, but the available data are not numerous enough to allow a meaningful comparison.

The limitations posed by dataset size can be partially overcome by the Leave-One-Out Cross-Validation technique. This procedure calibrates the model with all available data points but one, and uses the excluded value to validate the model in a predictive mode. This selection is repeated so that each observation in the sample is used once for validation.

The Leave-One-Out procedure has been performed for both *O. europea* and *S. oleracea*, for the non linear (equations (2.8) and (2.9)) and linear models (equations (2.15) and (2.16)), for the non-saline and the salt-stressed cases, and for the cost parameter λ and the efficiency parameter a_1.

The scatterplots comparing estimated and observed photosynthesis and stomatal conductance values from the Leave-One-Out procedure (Figure 2.17 for *O. europea* and Figure 2.18 for *S. oleracea*) show the absence of a significant estimation bias and the relatively modest dispersion between predicted and observed values, both for the non linear and the linear models.

Table 2.4 and 2.5 list the mean and standard deviation of the estimation errors (i.e. the absolute difference between the observed and the estimated values) computed for each validation point, for *O. europea* and *S. oleracea*. The parameter λ for the non linear model has been calibrated using eq. (2.9) and thus reflects errors in the stomatal conductance, and not photosynthetic rates. To normalize the results, a relative error is computed, defined by the ratio of the estimation error and the standard deviation of the observed values. The mean relative errors can now be directly compared to evaluate the predictive performances of the non linear and linear models.

For both *O. europea* and *S. oleracea*, the estimation errors in the non-

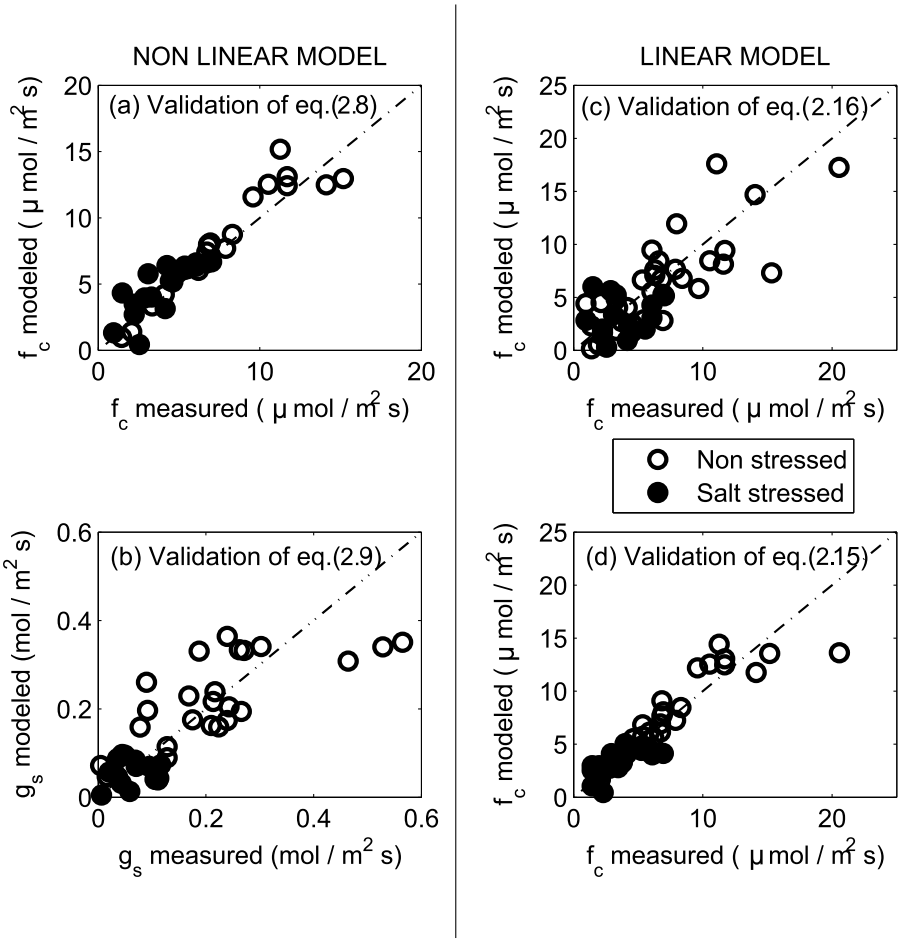

Figure 2.17: Scatterplots of estimated and observed photosynthesis and stomatal conductance values obtained from the Leave-One-Out procedure for *O. europea*. Left panels refer to the non linear model, right panels to the linear model. Filled circles are for salt-stressed conditions, open circles are for fresh water. Equations used are also listed.

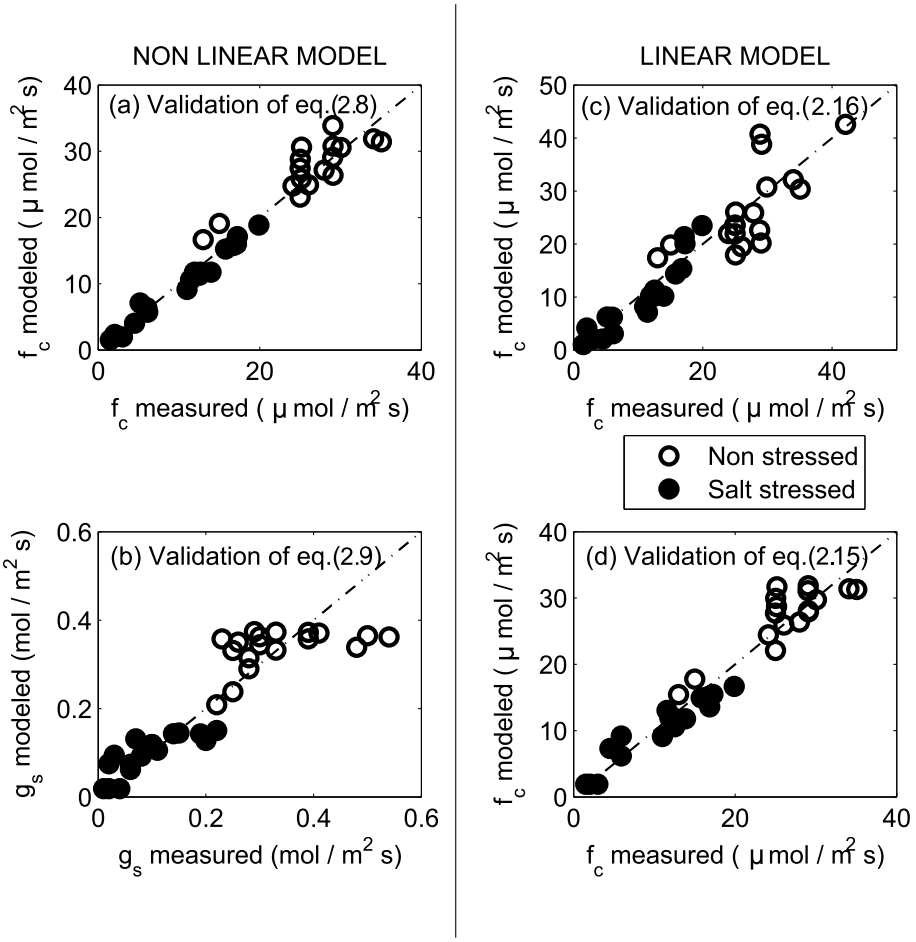

Figure 2.18: Same as Figure 2.17 but for *S. oleracea*.

Table 2.4: Statistics of the absolute and relative errors for the non linear (NLM) and linear (LM) models for *O. europea*.

	Non Stressed			**Salt Stressed**		
	Abs. Error		**Rel. Error**	**Abs. Error**		**Rel. Error**
	Mean	St.Dev.	Mean	Mean	St.Dev.	Mean
eq. (8) NLM	0.23	1.91	0.05	-0.69	1.90	-0.38
eq. (9) NLM	0.01	0.10	0.02	-0.01	0.04	0.23
eq. (15) LM	0.22	1.99	0.05	-0.32	1.21	-0.19
eq. (16) LM	-0.38	2.81	-0.09	-0.66	2.45	-0.36

Table 2.5: Same as Table 2.4 but for *S. oleracea*.

	Non Stressed			**Salt Stressed**		
	Abs. Error		**Rel. Error**	**Abs. Error**		**Rel. Error**
	Mean	St.Dev.	Mean	Mean	St.Dev.	Mean
eq. (8) NLM	0.34	3.62	0.05	-0.57	0.92	-0.10
eq. (9) NLM	<0.01	0.08	0.01	0.01	0.04	0.05
eq. (15) LM	0.19	4.03	0.03	-0.44	1.93	-0.08
eq. (16) LM	-0.67	5.58	-0.10	-0.67	2.52	-0.11

stressed case are lower, because of the wider data range. There is no significant difference between errors for the linear and the non linear models, thus indicating that the two models perform equally well in predicting photosynthesis and stomatal conductance in fresh-water and salt-stress conditions.

2.3.4 The relative role of stomatal and mesophyll limitations

The relative importance of the stomatal versus the mesophyll conductance in the overall effective conductance is presented in Figures 2.19(a) and 2.19(c), where measured and modeled (eq. (2.14)) conductances are compared. The Figures show that mesophyll conductance is far from infinite but rather comparable to the stomatal conductance, thus reinforcing the importance of accounting for mesophyll conductance in saline environments. Moreover, for

a fixed g_m, g_s is larger in the fresh water case than in salt stress conditions, suggestive that stomata can open more freely, in response to environmental factors such as light, temperature and humidity, when they are not stressed by salinity.

The same relationship can be explored in terms of resistances, $r = 1/g$, with the advantage of being able to more clearly separate stomatal and mesophyll effects in an additive manner, as $r_{eff} = r_s + r_m$ (Figures 2.19(b) and 2.19(d)). The r_s and r_m give similar contributions to r_{eff} in the case of spinach plants. For olive trees, the stomatal resistance is always lower than the mesophyll resistance in the freshwater case, but r_s and r_m become comparable in salt-stressed conditions.

Figures 2.20(a) and 2.20(b) report the $f_c - c_i$ and $f_c - c_c$ curves published in Delfine et al. (1998). Blue points are relative to fresh water while salt water is represented in red. The initial slope (CO_2 concentration < 100 ppm) of the relations is calculated and the results are shown in the Figure. The initial slope of the $f_c - c_i$ curve is affected by salinity, but this is not the case for the initial slope of the $f_c - c_c$ curve. This result is confirmed by other authors (Ball & Farquhar, 1984; Brugnoli & Lauteri, 1991; Delfine et al., 1998).

Moreover, the ratio among chloroplast and intercellular CO_2 concentration is constant with photosynthesis for the fresh water case, while it is smaller and decreases with photosynthesis in the salt-stress case (Fig. 2.20(c)). This emphasizes the importance of accounting for mesophyll conductance in saline conditions, and the error committed when assuming the intercellular CO_2 concentration to be equal to the one inside the cells.

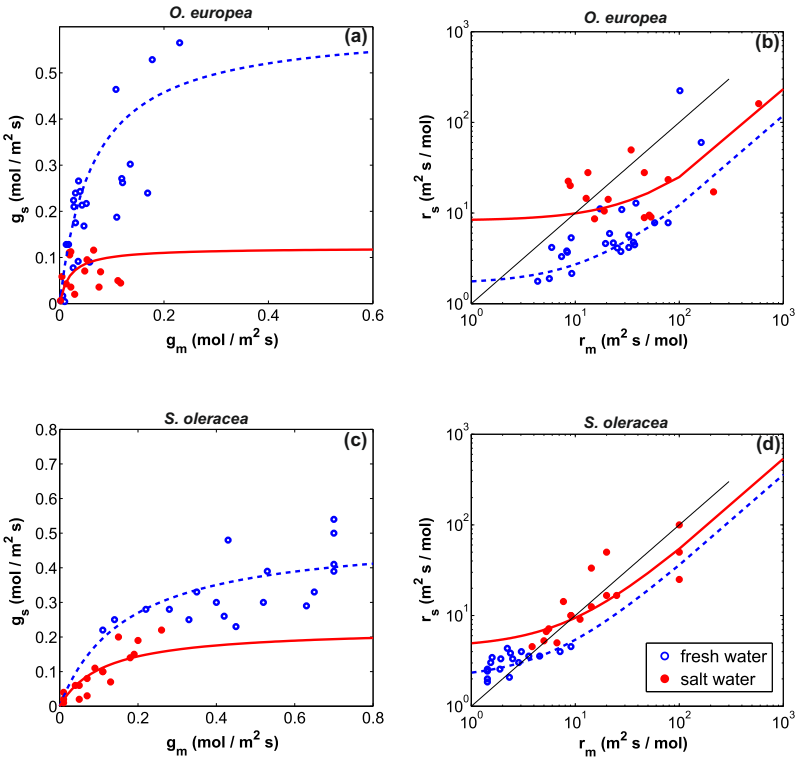

Figure 2.19: Stomatal conductance as a function of mesophyll conductance ((a) and (c)) and a log-log relationship between mesophyll and stomatal resistances ((b) and (d)) for both datasets. Legend as previous.

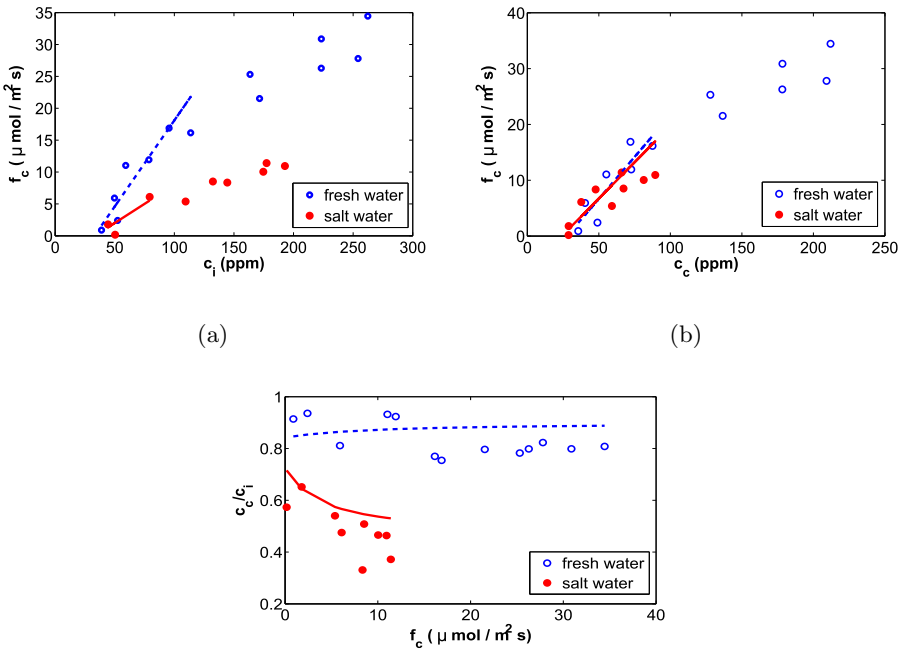

Figure 2.20: $f_c - c_i$ (a) and $f_c - c_c$ relationships (b) for the spinach dataset. Solid lines represent the initial slope of the curves for fresh water ($f_c = 0.27c_i - 8.90$ and $f_c = 0.30c_c - 8.32$) and dashed lines for salt water ($f_c = 0.12c_i - 3.99$ and $f_c = 0.26c_c - 6.28$) cases. (c): Relationship between c_c/c_i ratio and f_c for fresh and salt water for the spinach dataset. Dots represent measurements, lines represent the initial slope relationships showed in Panels (a) and (b) for the non-salt case (dashed, blue) and for the salt case (solid, red).

2.3.5 Effect of elevated atmospheric CO_2 concentration on gas exchange

The model in eq. (2.15), calibrated for the olive tree case, is now used to investigate the compound effect of salinity stress and elevated atmospheric CO_2 concentration.

While in trees a_1 can be assumed to be independent of ambient c_a (Ainsworth & Rogers, 2007; Ellsworth et al., 2011), the effects of CO_2 concentration are accounted for by linearly scaling the value of the cost parameter λ, as described in eq. (2.17) (where the reference ambient CO_2 concentration was set to $c_{a,0}$=380 ppm).

As previously discussed, salinity affects the cost parameter, the photosynthetic efficiency, a_1, and the mesophyll conductance.

As a first approximation, it could be assumed that λ increases linearly with leaf Na content, Na (expressed as a % of total leaf dry weight), and using the mean salinity values in Loreto et al. (2003) to derive $\lambda_0(Na) = 7.75 \cdot Na + 1.25$ μmol mol^{-1} kPa^{-1}, one finds the expression of $\lambda(c_a, Na)$:

$$\lambda(c_a, N_a) = \lambda_0(Na) c_a c_{a,0}^{-1}. \tag{2.23}$$

where the reference $c_{a,0}$=380 ppm.

Similarly, it is sensible to assume a_1 to decrease linearly with Na concentration according to $a_1 = -189.55Na + 59.33$ μmol m^{-2} s^{-1}, derived from model calibration and Na values reported in Loreto et al. (2003), while a_1 is independent of ambient CO_2 concentration c_a, as previosly noticed.

The representation of the dependence of mesophyll conductance on leaf Na content is somewhat more difficult to obtain on the basis of the available measurements. The saline and non-saline cases are thus represented using two contrasting typical values of g_m derived from Loreto et al. (2003). Namely, g_m=0.1170 mol m^{-2} s^{-1} is adopted for the salt-stress case, and g_m=0.23 mol m^{-2} s^{-1} for the fresh water case.

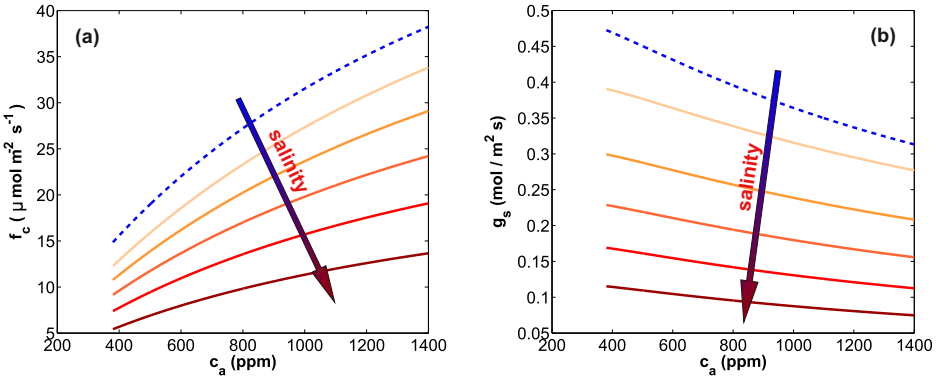

Figure 2.21: Effect of elvated ambient CO_2 concentration on photosynthesis (a) and stomatal conductance (b) for non stressed (dashed line) and salt stressed (solid line) cases, and for intermediate salinity levels.

Photosynthesis (f_c) increases with c_a (Figure 2.21 (a)), thus partially compensating for the adverse effects of salinity. As salinity increases, however, the sensitivity of the gas exchange rate to c_a decreases significantly. In fact, to offset salt stress, and obtain the same photosynthesis as under non-stressed conditions, an increase of over 1000 ppm of CO_2 concentration would be needed in the most severe salt stress case considered here. However, future smaller increases in atmospheric CO_2 may be sufficient to compensate less severe salt stress conditions.

Stomatal conductance, differently from f_c, decreases both in response to increased salinity and atmospheric CO_2 (eq. 2.14; see Figure 2.21 (b)). Thus, increased c_a may have the same consequences of salt stress on transpiration also in this case.

Given the uncertainties in the assumptions of the dependence of the parameters λ and a_1 on the salinity concentration Na, analyses are performed by removing these assumptions. To this end, the two contrasting cases of fresh water irrigation and salt stress conditions are considered (in which the salt-impacted values of the cost parameter λ and the photosynthetic efficiency a_1 are assumed on the basis of the model calibration described

in Section 2.3.2). The results (Figure 2.22 (a) and (b)) show the same behaviour of previous analyses.

Moreover, increased atmospheric CO_2 concentration alters the relative effects of salinity, changing the ratio between the two contrasting cases (salt-stressed over non-stressed) for both photosynthesis and stomatal conductance (Figures 2.22(c) and 2.22(d)). Here, the ratio between photosynthesis (or stomatal conductance) in the salt-stressed case and increasing c_a over the unstressed value at $c_{a,0} = 380$ ppm is shown. In Figure 2.22(c), as the ratio tends toward unity, the CO_2 effect balances the salt stress, indicating that salinity is mitigated by the increase of CO_2 concentration. In contrast, both elevated CO_2 and salinity decrease stomatal conductance and hence leaf transpiration.

2.4 Discussion

Salt stress causes both a reduction in plant growth (corresponding to reduced transpiration, as during drought), and a reduction in photosynthetic capacity, partly related to morphological changes (resulting in increased diffusive resistances in the leaf), and partly due to enzyme inhibition by excessive salt concentration (Munns, 2002; Munns & Tester, 2008). At the leaf level, these effects lead to decreased stomatal and mesophyll conductances and lowered photosynthetic efficiency (Ball & Farquhar, 1984; Longstreth et al., 1984; Downton et al., 1985; Bongi & Loreto, 1989; Brugnoli & Lauteri, 1991; Delfine et al., 1998, 1999; Centritto et al., 2003; Loreto et al., 2003; Parida et al., 2003; Flexas et al., 2004; Parida et al., 2004; Geissler et al., 2009). The proposed gas exchange model based on optimization theory is able to capture most of these observed patterns in the leaf CO_2 and water vapor fluxes with only two fitting parameters, the marginal water use efficiency λ and the photosynthetic capacity a_1. The former represents the cost of water losses through transpiration (Cowan & Farquhar, 1977) and thus regulates

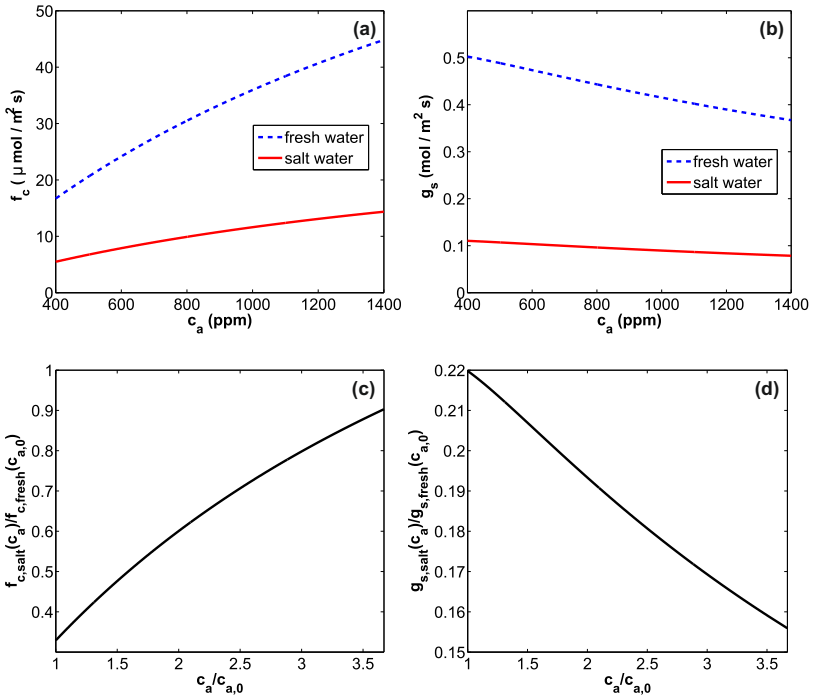

Figure 2.22: Effect of elevated atmospheric CO_2 concentration on photosynthesis (a) and stomatal conductance (b) for non stressed (dashed blue line) and salt stressed (solid red line) cases, for *O. europea*. Panels (c) and (d) show the ratio among salt-stressed and reference conditions as a function of normalized c_a. Note the near-constant ratios here for a 3.5 fold increase in atmospheric CO_2.

the sensitivity of stomata to the environment. An increase in salt stress increases the cost of water, λ, analogous to theoretical and experimental findings from drought stress studies (Makela et al., 1996; Manzoni et al., 2011). Plants in both experiments considered here were irrigated and hence do not suffer from soil moisture limitation *per se*. Hence, the increase in λ with salt stress represents a measure of leaf responses to adverse osmotic conditions. An increased salt concentration in the soil induces a restriction in transpiration that is beneficial to slow down further salt accumulation, and hence to prevent possible irreversible damages (at the expenses of lower carbon gains and plant growth).

Parameter a_1 reflects the intrinsic photosynthetic capacity of the leaf. For *O. europea*, Wullschleger (1993) reports a V_{cmax} of 8–23 μmol m^{-2} s^{-1}, much lower than 68–95 μmol m^{-2} s^{-1} reported for *S. oleracea* (both at 25°C). Consistent with this general pattern, our temperature-corrected estimates for a_1 are larger for spinach than for olive trees. For *O. europea*, $a_1 = 43$ μmol m^{-2} s^{-1}, an intermediate value between the lower estimates by Wullschleger (1993) and the higher by Díaz-Espejo et al. (2006) (50–90 μmol m^{-2} s^{-1}) and Nogués & Baker (2002) (150 μmol m^{-2} s^{-1}). These differences can be ascribed to different factors, ranging from growth conditions to leaf age. Light intensity also plays a role, as the values obtained from model calibration are lower if light limiting conditions are assumed. Moreover, the literature values of V_{cmax} do not take into account the effect of the mesophyll conductance, which is explicitly included in the model and hence the inference of a_1. If, for instance, g_m is assumed not to be limiting CO_2 exchange, then the calibrated values of a_1 decrease significantly. In this case, and for non stressed leaves, $a_{1,ns} \approx 25$ μmol m^{-2} s^{-1} for *O. europea* and $a_{1,ns} \approx 88$ μmol m^{-2} s^{-1} for *S. oleracea*, in line with the values reported by Wullschleger (1993). This consistency of a_1 with independent estimates when $g_m/g_s >> 1$ lends support to the robustness of the proposed model.

The fresh water/salt water comparisons further show that the photosynthetic capacity of the plant is directly impacted by increased salt stress, as evidenced by a (statistically significant) $30 - 40\%$ reduction in maximum carboxylation capacity. This shows that the reductions in photosynthetic rate observed under salt stress is not only due to a limitation of CO_2 diffusion (associated with reduced mesophyll and stomatal conductances), but also caused by a direct negative effect on the metabolic apparatus of the plant, consistent with Ball & Farquhar (1984); Seemann & Sharkey (1986); Bongi & Loreto (1989); Paranychianakisa & Chartzoulakisb (2005); Egea et al. (2011). Interestingly, the optimization framework also predicts a non-linear scaling between stomatal and mesophyll conductances (eq. (2.14)) as salinity effects become more severe - consistent with observations (Figure 2.19). Such a relationship, together with the reduced photosynthetic capacity, allows disentangling the diffusive and biochemical limitation to CO_2 uptake under salinity.

Overall, these modeling results (increased λ and decreased a_1) support the hypothesis that plant response to salinity and water stress are similar (Munns, 2002; Chaves et al., 2009; Lawlor & Tezara, 2009; Vico & Porporato, 2008). The initial response to stress (i.e., reduced g_s and leaf elongation) is analogous in saline and drought conditions. In the long-term, however, salt-specific effects linked to the toxic effect of salt arise (e.g. reduction in a_1 and mesophyll conductance). The osmotic stress induced by salinity reduces the water potential in the soils and thus plants tend to minimize the water loss by closing the stomata (Geissler et al., 2009), similar to drought responses.

An interesting extension of the present study is to explore the compound effect of salt stress and elevated CO_2 concentration in the atmosphere. In the halophyte *Aster tripolium* salinity reduced photosynthesis and stomatal conductance, although net photosynthesis was significantly ameliorated under elevated atmospheric CO_2 concentrations, while intercellular CO_2 concentra-

tion increased (Geissler et al., 2009). Similar positive effects of elevated CO_2 were found by Nicolas et al. (1993) in wheat, but no significant effect was observed by Melgar et al. (2008) in olive trees. Ainsworth & Rogers (2007) also report a reduction in stomatal conductance and an increased photosynthesis under elevated CO_2 concentration for both C_3 and C_4 species. These effects are confirmed by the model results here that quantify the atmospheric CO_2 concentration at which the photosynthetic reduction induced by salt stress may be offset.

Chapter 3

Effect of vegetation on sediment resuspension

3.1 Remote Sensing and Modelling of Suspended Sediment Concentration in Shallow Tidal Areas

In this Chapter the stabilizing effect of vegetation on sediment resuspension will be studied in a spatially distributed manner, by combining the results of remote sensing and mathematical modelling, with application to shallow coastal waters.

The geomorphodynamic evolution of shallow coastal areas, such as lagoons and estuaries, is largely controlled by the transport of sediment, organic matter, and other suspended or dissolved substances (Fagherazzi et al., 2004, 2007; Marani et al., 2007b; Perillo et al., 2009). The existence of such environments is crucially dependent on a subtle balance between sediment inflow and outflow, originated by wind-wave erosion and tidal currents, and relative sea level rise. Suspended particulate matter (SPM) distribution in space and time, in particular, plays a major role in erosion/deposition pro-

cesses and is thus a key property to be observed in search for the mechanisms controlling the morphodynamics of intertidal areas.

The possible interaction with bio-stabilization and bio-turbation processes, e.g. related to submerged vegetation and algae, is also a fundamental key element in determining the dynamics of a tidal area. Figure 3.1 shows some of the chief modes of interaction among submerged vegetation (macrophytes) and sediment dynamics (Madsen et al., 2001), yielding to two possible stable equilibria. A low-vegetation equilibrium (panel A) characterized by high current velocities, inducing a high sediment resuspension from the bottom and thus an increased water turbidity. This reduces the amount of light penetrating the water column, with a negative feedback on vegetation growth. The second equilibrium state (panel B) is a highly vegetated one. In this case the current velocities are attenuated, thereby leading to reduced sediment resuspension and clearer water. This allows a greater light penetration into the water column, which favors plant photosynthesis and development. This simple example clarifies the potential importance of vegetation in controlling sediment resuspension and morphological dynamics, thus suggesting the relevance of simultaneously studying the spatial distribution of SPM and submerged vegetation (Carr et al., 2010).

Ideally, observations of SPM concentration should have a high spatial and temporal resolution. In practice, while they can be acquired at a high temporal resolution (e.g. hourly), observation networks are typically sparse (spacings of several kilometers) compared with the scale of typical morphological features such as marshes and tidal flats (with sizes ranging from a few meters to kilometers). Remote sensing can be used to obtain information about several water quality parameters, including SPM concentration, and allows to overcome the spatial limitation of in situ probes.

SPM retrievals in lagoon and estuarine waters (Case II waters, Mobley (2004)) are particularly difficult to obtain, due to the presence of a variety of

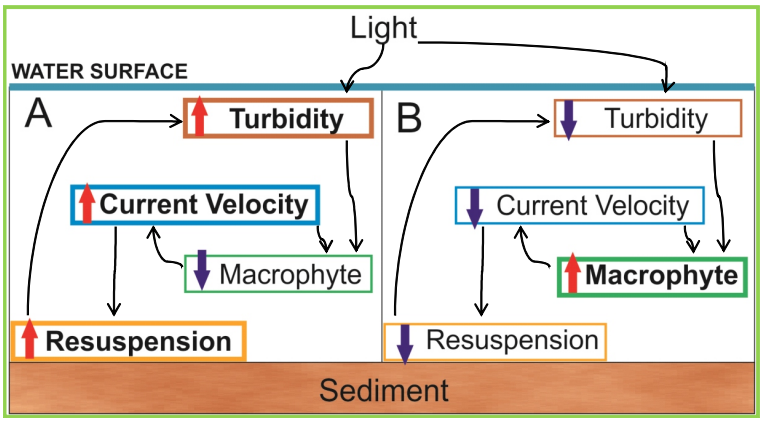

Figure 3.1: Schematization of water vegetation and sediment dynamics interactions. Panel (A) represents a configuration with sparse vegetation and high sediment resuspension and water turbidity. Panel (B) shows the scenario with high presence of vegetation, which slows down the current velocities and thus reduces water turbidity and light attenuation. (Adapted from Madsen et al. (2001))

suspended and dissolved materials and to the potentially large contribution of the bottom sediment to the detected remote sensing signal, which becloud the identification and accurate measurement of the contribution coming from sediments in the water column.

Most of the existing literature on the estimation of SPM concentration from remote sensing concerns oceanic or relatively deep marine coastal waters (Ferrari & Tassan, 1991; Babin et al., 2003a,b; Binding et al., 2005; Giardino et al., 2007) and, often, low-resolution sensors unsuitable for applications in estuaries and lagoons (e.g. Chen et al. (2007b)). Moreover, site-specific empirical approaches are widely used (Östlund et al., 2001; Zhang et al., 2002; Ekercin, 2007; Chen et al., 2007a). These approaches, which have the merit of demonstrating the existence of a clear and detectable relation between water composition and remote sensing observations and are certainly useful for specific study sites, are not suitable for general applications to estuarine/lagoon studies because they fundamentally depend on the specific data and conditions under which they are calibrated. This means

that any application to a new site or any change of sensor or resolution requires a new calibration, leaving little room for generalization.

A more general approach should be based on theoretical models of radiative transfer in turbid waters, which, with varying degrees of approximation, provide a representation which is consistent with the governing physical processes, possibly allowing insights in the processes themselves and applications to a wider range of conditions than afforded by empirical approaches (e.g. Dekker et al. (2001); Mobley (2004); Giardino et al. (2007); Brando et al. (2009)).

In this Chapter we will apply a theoretically- and physically-based approach using a simple radiative transfer model (Lee et al., 1998, 1999) to relate at-satellite radiance measurements and in situ turbidity observations with application to the Venice lagoon (Italy).

The SPM concentration maps retrieved from satellite images can be extremely useful in the validation of sediment transport models, which by definition involve the use of spatially-distributed parameterizations. Here the results obtained from remote sensing are used to assess the performance of a finite element model of sediment erosion, deposition, and transport in the Venice lagoon (Carniello et al., 2011b).

3.2 Methods

3.2.1 The Radiative Transfer Model

The remote sensing reflectance of a 'water pixel' is a function of the water depth, of the properties of the matter suspended in it, and of the optical properties of the bottom. In order to obtain a physically-based estimation of SPM concentration, a simple radiative transfer model (Lee et al., 1998, 1999) is used, which links the directional remote sensing reflectance in the nadir direction (at a fixed wavelength of interest, λ, which is omitted here

to simplify the notation) to the controlling physical factors. The below-surface remote sensing reflectance r_{rs} (sr^{-1}) is defined as the ratio between upwelling (directional) radiance and downwelling irradiance, and can be modeled as

$$r_{rs} = r_{rs}^{dp}\left[1 - e^{-\left(K_d + K_u^C\right)H}\right] + \frac{\rho_b}{\pi} e^{-\left(K_d + K_u^B\right)H}, \tag{3.1}$$

where:

-H = water depth (m);

-ρ_b = bottom albedo (assuming bottom as a Lambertian reflector);

-r_{rs}^{dp} = subsurface remote sensing reflectance for an infinitely deep water column $(1/\text{sr}) = (0,084 + 0,17u)u$ (Lee et al., 1999);

-$u = b_b/(a + b_b)$, with b_b backscattering coefficient $(1/m)$ and a absorption coefficient $(1/m)$;

-$K_d = D_d\alpha =$ downwelling diffusive attenuation coefficient;

-$K_u^C = D_u^C\alpha =$ upwelling diffusive attenuation coefficient due to the water column;

-$K_u^B = D_u^B\alpha =$ upwelling diffusive attenuation due to the bottom reflectance;

-$\alpha = a + b_b$;

-$D_d = 1/\cos\Theta_w$, Θ_w =subsurface solar zenith angle (rad);

-$D_u^C = 1,03(1 + 2,4u)^{0,5}$ (Lee et al., 1999);

-$D_u^B = 1,04(1 + 5,4u)^{0,5}$ (Lee et al., 1999).

r_{rs} is then linked to the above-surface remote sensing reflectance R_{rs} (sr^{-1}), defined as the ratio between water-leaving radiance and downwelling irradiance, by the following approximate relationship (Lee et al., 1999):

$$R_{rs} = \frac{0.5\, r_{rs}}{1 - 1.5\, r_{rs}}. \tag{3.2}$$

Eqs (3.1) and (3.2) together constitute a model relating the surface directional remote sensing reflectance R_{rs}, which can be obtained from remote sensing observations upon proper atmospheric correction, with the quantity

and type of matter suspended in the water column.

The absorption and backscattering coefficients involved in eq. (3.1) are influenced by suspended sediments (organic or inorganic), dissolved solids and are also dependent on the specific properties of the sediments (e.g. the grain size distribution). These coefficients may have a significant variation because of the specific properties of the sediments (e.g. the grain size distribution) and are in the following determined by calibration. However, physically meaningful values of these parameters fall within somewhat limited intervals, allowing additional constraints and control on the formulation of the model, as well as the possibility of assigning parameter values on the basis of sediment characteristics or by analogy with similar sites.

The influence of the different components of the total solids in the water column (suspended inorganic and organic matter, dissolved organic matter, etc.) on its optical properties strongly depends on the wavelength considered. Here we adopt, consistently with previous literature (e.g. Petzold (1972); Gallegos & Correl (1990); Ferrari & Tassan (1991); Li et al. (2003); Babin et al. (2003a,b); Binding et al. (2005); Bowers & Binding (2006)), the value of remote sensing reflectance at $\lambda = 650\ nm$, where the sensitivity to the suspended sediment concentration is high, while effects e.g. by chlorophyll and organic particles are limited (e.g. Mobley (2004)).

The total absorption coefficient, a, is expressed as the sum of the absorption coefficients of pure water a_w ($a_w(\lambda = 650\,nm) = 0.3594\ m^{-1}$, (Pope & Fry, 1997)), inorganic particles a_{NAP}, phytoplankton a_{ph}, and organic particles a_{CDOM}:

$$a = a_w + a_{NAP} + a_{ph} + a_{CDOM}. \tag{3.3}$$

a_{NAP} may be assumed to be a linear function of the SPM concentration (in g/m^3), as proposed in Babin et al. (2003b) for $\lambda = 443\,nm$:

$$a_{NAP}(\lambda = 443\,nm) = \gamma \cdot SPM. \tag{3.4}$$

Previous studies allow the computation of possible values for γ (e.g. parameter values given in Babin et al. (2003b) yield $\gamma = 0.041\, m^2/g$ in the northern Adriatic sea) but, because of its dependence on local sediment characteristics, γ is here determined by calibration. In what follows, the relation $a_{NAP}(\lambda) = a_{NAP}(\lambda = 443nm)0.75e^{-0.0128(\lambda-443)}$ (Babin et al., 2003b) to recover $a_{NAP}(\lambda = 650\, nm)$ will thus be used.

The phytoplankton absorption coefficient can be linearly related to the chlorophyll-a concentration, C_a, as $a_{ph}(\lambda = 650\, nm) = a^*_{ph} \cdot C_a$, with $a^*_{ph} = 0.0077\ m^2/mgChla$, the specific phytoplankton absorption coefficient (Gallegos & Correl, 1990). Knowledge of the chlorophyll-a concentration (e.g. from reflectance information in other spectral bands) can be used to eliminate C_a from the absorption model. In order to quantify the advantage of accounting for chlorophyll effects, chlorophyll concentrations observed simultaneously with SPM concentrations were used. However, the correction to the absorption term associated with measured chlorophyll concentrations was not significant for the estimation of SPM concentrations. Therefore, chlorophyll-a concentration is considered fixed to a nominal value in subsequent analyses ($3\, mg/l$, the summer average in the Venice lagoon).

Similarly, $a_{CDOM}(\lambda) = a_{CDOM}(\lambda = 375\, nm)e^{-0.0192(\lambda-375)}$ (Babin et al., 2003b) ($a_{CDOM}(\lambda = 375\, nm) = 1.25\, m^{-1}$ consistently with parameter values derived from Ferrari & Tassan (1991) for the Northern Adriatic sea). Tests with different assumptions for $a_{CDOM}(\lambda = 375\, nm)$ show little sensitivity on its specific value in a relatively large range.

The backscattering coefficient b_b is the fraction of the total scattering coefficient, b, determined by photons scattered at an angle greater than 90°. Here a fixed value of the ratio $b_b/b = 0.019$ is adopted, determined observationally (Petzold, 1972; Binding et al., 2005; Bowers & Binding, 2006). The total scattering coefficient b is expressed as the sum of contributions by pure water b_w, phytoplankton b_{ph}, and inorganic particles b_{NAP}:

$$b = b_w + b_{ph} + b_{NAP}. \tag{3.5}$$

Scattering by inorganic particles dominates other scattering sources, such that b_w and b_{ph} may be neglected with respect to b_{NAP} (Pope & Fry, 1997; Binding et al., 2005; Bowers & Binding, 2006). Following Babin et al. (2003a) it is:

$$b_{NAP}(\lambda = 650\,nm) = \eta \cdot SPM \tag{3.6}$$

(based on $b_{NAP}(\lambda = 650nm) = \eta_1 \cdot b_{NAP}(\lambda = 555\,nm)$ and $b_{NAP}(\lambda = 555\,nm) = \eta_2 \cdot SPM$, $\eta = \eta_1 \cdot \eta_2$).

η is here determined by calibration, due to its dependence on sediment properties. Previous studies (Babin et al., 2003a) allow the computation of the value $\eta = 0.405m^2/g$, which may be used as a term of comparison for calibration results.

The bottom albedo is a function of the type of bottom sediment and of the possible presence of vegetation or of benthic organisms. In the following, a sensitivity analysis of the SPM concentration retrieved by use of eq. (3.1) on the basis of values of ρ_b within a range consistent with observations is presented.

3.2.2 The Morphodynamic Model

The morphodynamic model consists of three modules: i) the hydrodynamic module, ii) the wind-wave module, and iii) the sediment transport and bed evolution module.

The hydrodynamic module solves the two-dimensional shallow water equations modified including a refined sub-grid modeling of the bathymetry to deal with flooding and drying processes in very irregular domains:

Table 3.1: List of Symbols for the radiative transfer model.

Symbol	Description	unit
r_{rs}	Subsurface remote-sensing reflectance	sr^{-1}
R_{rs}	Above-surface remote-sensing reflectance	sr^{-1}
ρ	Surface Reflectance	-
ρ_b	Bottom albedo	-
r_{rs}^{dp}	r_{rs} value for optically deep waters	sr^{-1}
K_d	Vertically averaged diffuse attenuation coefficient for downwelling irradiance	-
K_u^C	Vertically averaged diffuse attenuation coefficient for upwelling radiance from water-column scattering	-
K_u^B	Vertically averaged diffuse attenuation coefficient for upwelling radiance from bottom reflectance	-
θ_w	Subsurface solar zenith angle	rad
a_w	Absorption coefficient of pure water	m^{-1}
a_{NAP}	Absorption coefficient of non algal particles	m^{-1}
a_{ph}	Absorption coefficient of phytoplankton pigments	m^{-1}
a_{CDOM}	Absorption coefficient of yellow substances	m^{-1}
a	Total absorption coefficient: $a = a_w + a_{NAP} + a_{ph} + a_{CDOM}$	m^{-1}
b_b	Backscattering coefficient	m^{-1}
b_w	Scattering coefficient of pure water	m^{-1}
b_{ph}	Scattering coefficient of phytoplankton pigments	m^{-1}
b_{NAP}	Scattering coefficient of suspended particles	m^{-1}
b	Total scattering coefficient: $b = b_w + b_{ph} + b_{NAP}$	m^{-1}

$$\frac{\partial q_x}{\partial t} + \frac{\partial}{\partial x}\left(\frac{q_x^2}{Y}\right) + \frac{\partial}{\partial y}\left(\frac{q_x q_y}{Y}\right) - \left(\frac{\partial R_{xx}}{\partial x} + \frac{\partial R_{xy}}{\partial y}\right) + \frac{\tau_{bx}}{\rho} - \frac{\tau_{wx}}{\rho} + gY\frac{\partial h}{\partial x} = 0 \tag{3.7}$$

$$\frac{\partial q_y}{\partial t} + \frac{\partial}{\partial x}\left(\frac{q_x q_y}{Y}\right) + \frac{\partial}{\partial y}\left(\frac{q_y^2}{Y}\right) - \left(\frac{\partial R_{xy}}{\partial x} + \frac{\partial R_{yy}}{\partial y}\right) + \frac{\tau_{by}}{\rho} - \frac{\tau_{wy}}{\rho} + gY\frac{\partial h}{\partial y} = 0 \tag{3.8}$$

$$\eta\frac{\partial h}{\partial t} + \frac{\partial q_x}{\partial x} + \frac{\partial q_y}{\partial y} = 0, \tag{3.9}$$

where:

- t: time;
- h: water level;
- Y: effective water depth;
- $q = (q_x, q_y)$: depth integrated phase averaged velocity;
- R_{ij}: Reynolds stresses;
- $t_{b,curr} = (t_{bx}, t_{by})$: stress at the bottom produced by the tidal current;
- $t_{w,curr} = (t_{wx}, t_{wy})$: wind shear stress at the free surface;
- η: wetted area per unit surface;
- ρ: density of the fluid;
- g: gravitational constant.

The equations are solved using a semi-implicit staggered finite element method based on Galerkin's approach. The bottom topography is described using flat triangular elements with elevation equal to the averaged elevation in the element. Bottom roughness distribution is considered during the wetting and drying transient using the η function (see Defina (2000); D'Alpaos & Defina (2007) for a detailed description of the hydrodynamic model).

The hydrodynamic model yields water levels which are used by the wind-wave model to compute the wave group celerity and to assess the wave-processes affected by flow depth (e.g., energy dissipation by friction and

wave breaking).

The wind wave model is based on the solution of the wave action conservation equation:

$$\frac{\partial N}{\partial t} + \frac{\partial (N c_{gx})}{\partial x} + \frac{\partial (N c_{gy})}{\partial y} + \frac{\partial (N c_{\theta})}{\partial \theta} + \frac{\partial (N c_{\sigma})}{\partial \sigma} = \frac{S}{\sigma}, \tag{3.10}$$

where:

- $N = E/\sigma$, $E = gH^2/8$ =specific energy and σ =relative frequency;
- $c_g = 0.5\ c[1 + 2kY/senh(kY)]$ =group celerity;
- $c_\theta = d\theta/dt$;
- $c_\sigma = d\sigma/dt$.

Eq. (3.10) is parameterized following the approach proposed by Holthuijsen et al. (1989) modified as the spatial and temporal distribution of wave period is determined through an empirical correlation function relating the mean peak wave period to the local wind speed and water depth ($\frac{\partial (N c_\sigma)}{\partial \sigma} = 0$). The wave propagation direction is assumed coincident with the wind blowing direction ($\frac{\partial (N c_\theta)}{\partial \theta} = 0$). For a thorough description and application of the wind wave model coupled with the hydrodynamic model please refer to Carniello et al. (2005, 2011a).

The sediment transport model is based on the solution of the advection diffusion equation:

$$\frac{\partial C_i Y}{\partial t} + \nabla \mathbf{q} C_i - \nabla (\mathbf{D} Y \nabla C_i) = E_i - D_i \tag{3.11}$$

and the Exner equation:

$$(1 - \eta)\frac{dz_b}{dt} = (D_s + D_m) - (E_s + E_m), \tag{3.12}$$

where:

- i = s (non cohesive- sand); m (cohesive-mud);

- C: depth averaged sediment concentration;
- Y: effective water depth;
- $q = (q_x, q_y)$: depth integrated phase averaged velocity;
- $\mathbf{D}$: two-dimensional diffusion tensor;
- E: entrainment rate;
- D: deposition rate;
- z_b: bed elevation;
- n: bed porosity.

The diffusion term can be neglected compared to advection (e.g., Pritchard & Hogg (2003)), thus leading to $\nabla(\mathbf{D}Y\nabla C_i) = 0$. Entrainment and deposition rates, as well as critical shear stress, depend on the bottom cohesion evaluated by the model on the basis of the actual percentage of mud characterizing bottom bulk. Bed porosity n of the mixture is assumed to be constant in time and space; a well mixed active layer is present just below the bed surface (Hirano, 1971, 1972; Armanini & Silvio, 1988; Armanini, 1995).

The model considers the contemporary presence of two size-classes of sediments: bed composition is, in fact, schematized using non-cohesive sand and cohesive mud, composed by both clay and silt. Given an initial bed configuration, the bed evolution module reproduces the evolution of the bottom both in terms of bed elevation and bed composition, as a consequence of different sand/mud deposition and erosion rates. The sediment transport module and the bottom evolution module are presented and discussed in detail in Carniello et al. (2008, 2011b).

The stabilizing effect on sediment resuspension played by benthic vegetation is accounted for in the model by introducing a "resuspension coefficient" which can vary from 0 (no resuspension) to 1 as a function of the vegetation type and density.

Spatial non-uniformity of wind climate over large basins may have a non-negligible impact on the description of wind wave field and, therefore, on wave induced sediment resuspension. Accordingly, the hydrodynamic and wind wave model take into account the spatial variability of the wind field which is determined through a suitable interpolation procedure performed on the available wind data using the Cressman method (Brocchini et al., 1995; Cressman, 1959), which is a standard and long-used technique in meteorological data interpolation.

3.2.3 Study Site and In Situ Observations

The Venice lagoon (Fig. 3.2) has an area of about 550 km^2, a mean water depth of about 1.1 m, and is characterized by a tidal range of about 1.3 m, with a main periodicity of about 12 hours.

Water quality and sediment transport are very important issues in the Venice lagoon due to the high water residence times, particularly in the inner parts of the lagoon, and to the large net outgoing sediment flux associated with a diffuse erosion of tidal morphologies (Fagherazzi et al., 2007; Marani et al., 2007b).

Many studies and field campaigns have shown that the Venice lagoon is subject to an erosive trend, with a net loss fine sediments (e.g., Day et al. (1999); D'Alpaos & Martini (2003); Defina et al. (2007); Carniello et al. (2009); Molinaroli et al. (2009)). Nevertheless the estimation of the net amount of fine sediments re-suspended within the lagoon and actually flowing out to the sea is a quite difficult task with great impact on the ongoing restoration activities which have been ongoing since the last few years/decades. The erosive trend which the lagoon has been experiencing since the beginning of the last century can be ascribed to different causes among which: i) The diversion of the big rivers by the "Serenissima Repubblica di Venezia" (the former Venetian state); ii) The construction of

long jetties at the three inlets at the end of the nineteenth century, which promoted a strongly non-symmetrical hydrodynamic behavior between flood and ebb, favoring sediment ejection out of the lagoon toward the see (e.g. D'Alpaos & Martini (2003); Martini et al. (2004); Tambroni & Seminara (2006)).

A network of multi-parametric probes (currently 10, see Figure 3.2 - LT stations) monitors with a half-hourly temporal resolution several key water quality parameters, among which are turbidity and chlorophyll-a concentration (the network is managed by the Venice Water Authority, see `http://www.magisacque.it/sama/sama_monitoraggi1.htm`). Water turbidity is measured through a backscattering optical probe (Seapoint turbidity meter, operating at 880 nm) and is expressed in Formazine Turbidity Units (FTU), which may be directly related to the suspended sediment concentration (Old et al., 2001). Pressure measurements at the probe allow the determination of the local instantaneous water depth. In fact, because the tidal amplitude is comparable to the mean water depth, the local instantaneous water depth varies significantly over time and this must be properly accounted for in the radiative modelling and SPM concentration retrieval scheme.

Wind speed and direction as well as the tidal oscillation are also measured with a half-hourly temporal resolution at several stations within the lagoon and this type of data have been used as boundary conditions to perform the numerical simulations. In particular the spatial and temporal evolution of the wind field over the lagoon is determined on the basis of the data collected at the wind stations shown in Figure 3.2, while tidal levels measured at the CNR platform (W5 station in Figure 3.2) has been imposed at the seaward limit of the computational domain.

Figure 3.2 also shows the area of the lagoon colonized by phanerogams (mainly *zostera marina* and *cymodocea nodosa*) as indicated by in situ map-

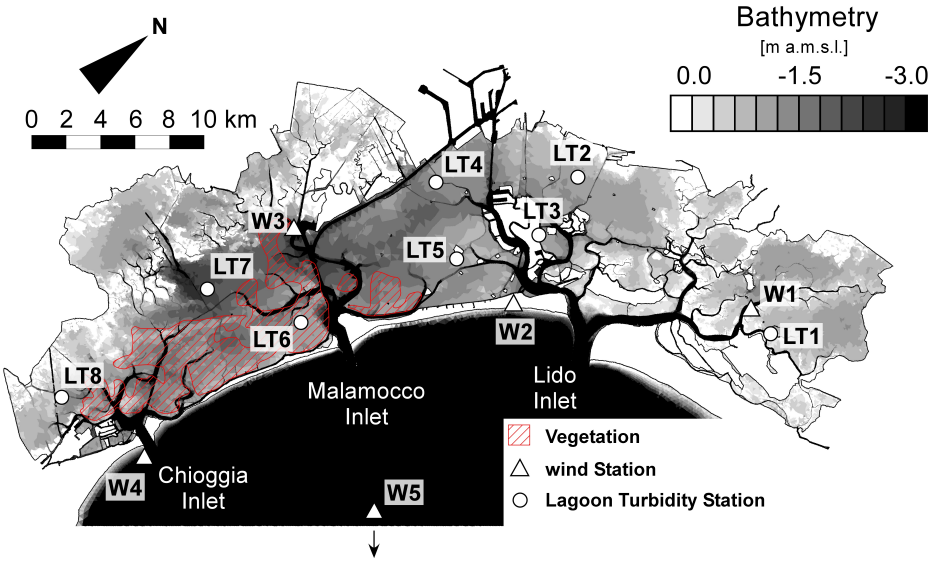

Figure 3.2: Map of the study site (Venice lagoon) with the in situ observation stations. Areas colonized by submerged vegetation are also shown (red hatch).

ping for 2004 (MAV, 2004). The two plant species are both well rooted in the soil, as shown in Figure 3.3.

It is worth noting that vegetation extent and density vary seasonally and for this reason, in order to correctly reproduce its stabilizing effect, it would be necessary to map the actual vegetation extent at the time of satellite acquisitions.

3.3 Results

3.3.1 Radiative transfer model calibration and validation

A set of 13 multispectral satellite acquisitions was used, with concurrent field observations, for the calibration and validation of the radiative transfer model described in Section 3.2.1. Only cloud-free acquisitions were selected in order to minimize uncertainties due to possibly heterogeneous atmospheric conditions. Data from different sensors are used in order to

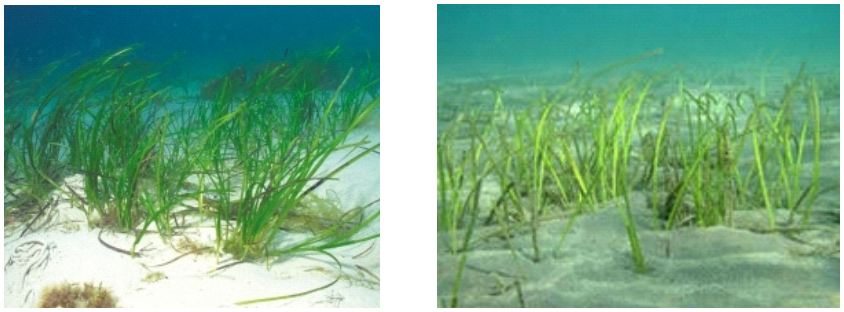

(a) (b)

Figure 3.3: Representation of the two most common plant species in the Venice lagoon: *zostera marina* (a) and *cymodocea nodosa* (b).

explore the possible impacts of specific sensor characteristics and spatial resolution (pixel size from 10 to 30 m). In particular, the data used are from the Landsat TM5 (2 images), Landsat ETM7 (2 images), ASTER (8 images) and ALOS AVNIR (1 image) sensors. These are all nadir-viewing sensors, with a narrow field of view (FOV) (FOV=5° for ASTER and ALOS, FOV=15° for Landsat), consistently with the narrow field of view assumption embedded in the radiative transfer model for the water column. The key technical characteristics of the satellite sensors/data involved in the study are summarized in Table 3.2.

Resolution is an important issue when comparing remote sensing data from different sensors (which provide an integral measure of surface optical properties) and in situ point observations. However, the distribution of SPM concentration is generated by the interaction of wind waves with the bottom sediment and is modulated by the lagoon morphology. The typical spatial correlation scales of wind fields and of the bathymetry of the tidal flats where the turbidity sensors are located are larger than the resolutions of the data considered here and the suspended sediment concentration may thus be assumed to be homogeneous within each pixel. Hence, it is reasonable to 'mix' remote sensing data with the different resolutions considered here,

and to compare the information retrieved with point in situ observations.

In order to retrieve the at-surface reflectance information, the remote sensing data have been radiometrically calibrated and atmospherically corrected by use of MODTRAN 4.1 (as implemented in ATCOR 2/3, see Richter (2009)). The radiometric calibration, ie. the conversion of digital numbers into radiances, was performed using image-specific information provided in each image metafile. MODTRAN allows the determination of the downwelling spectral irradiance and of the at-surface upwelling spectral radiance in the nadir direction from measured radiances (all sensors used are nadir-viewing and the in-scene variation of the view angle has been neglected), the observation geometry for each image (sun azimuth and elevation), and the atmospheric parameters, thereby allowing the estimation of the spectral directional reflectance for the nadir direction, $\widehat{R}_{rs}$. Atmospheric properties were defined in terms of aerosol type, water vapour and visibility. The specification of the aerosol type determines the absorption and scattering properties of the particles and the wavelength dependence of the optical properties. It is assumed here the *maritime* aerosol type (see Richter (2009); Cattrall & Thome (2003)), which produced the best match with available reference spectra. The water vapour content has been estimated on the basis of season (*midlatitude summer* or *winter* according to the acquisition period, see Richter (2009) for definitions). The visibility, assumed to be constant within each scene, was computed from the aerosol optical thickness at 550 nm obtained from a CIMEL CE-318-2 sun photometer from the AERONET network (`http://aeronet.gsfc.nasa.gov`). The computed visibility values range between 30 km and 70 Km.

The images have finally been georeferenced with a typical RMSE smaller than 1 pixel size and a maximum RMSE smaller than 1.5 pixel size, thus ensuring an accurate matching between remote sensing and field observations.

The value of the nadir directional reflectance at the surface retrieved

Table 3.2: Technical characteristics of the satellite sensors/data used in the study.

Sensor	Spectral band used (μm)	Pixel size (m)	Number of images
LANDSAT 5TM	B3 0.63 – 0.69	30	2
LANDSAT 7ETM	B3 0.63 – 0.69	30	2
ASTER VNIR	B2 0.63 – 0.69	15	8
ALOS AVNIR2	B3 0.61 – 0.69	10	1

from remote sensing, $\widehat{R}_{rs}$, may now be used on the left-hand side of eq. (3.2), which allows, upon consideration of eq. (3.1) and proper calibration, the estimation of SPM, the only remaining unknown.

After geocoding, the remote sensing reflectance values relative to the pixel containing each observation station was extracted and paired to the measurement performed at the time closest to the acquisition time. The data selection procedure and the variable number of stations active at any time resulted in a data set consisting of 53 data pairs, to be used for calibration and validation.

Observations of bottom reflectance ρ_b (mean of $0.027\,sr^{-1}$ at $\lambda = 644nm$), were available from just one site in the lagoon, within a shallow area with silty-sand bottom sediment (MAV, 2004). Bottom reflectance estimates were derived from simultaneous upwelling and downwelling radiance and irradiance observations (SeaPRISM radiometer, see Zibordi et al. (2004)). Data were collected with an azimuth angle of 90° with respect to the sun plane, and with a nadir view angle of 40° (S95 protocol (Mueller & Austin, 1995)).

A possible limitation to the application of eq. (3.1) to the retrieval of SPM concentration lies in the term on the right-hand-side of eq. (3.1) involving the bottom albedo, ρ_b. This term tends to become important when the water depth is low and/or when the turbidity is low. ρ_b is not usually known in a spatially-distributed manner and may be time-dependent (e.g. due to vegetation, algal, and microphytobenthos dynamics). Attempts can be made to estimate the bottom reflectance from remote sensing data col-

lected under clear-water conditions. However, it is in practice impossible to identify situations in which SPM is nearly zero everywhere. This circumstance makes the estimation of ρ_b rather uncertain, because relatively small changes in the assumed SPM, particularly when the concentration is low, can induce significant differences in the estimated values. In the following we will thus use a single bottom reflectance value derived from the point observations described above and, in order to limit the inaccuracies involved in this assumption, the conditions under which the specific value assumed significantly affects the retrieved SPM concentration will be identified.

Once the bottom reflectance has been specified, eq. (3.1) only contains the unknown SPM concentration and the yet-undetermined parameters describing absorption and scattering processes as a function of SPM (eqs. 3.4 and 3.6). Because of their impact on the computed reflectance and their potential dependence on site-specific sediment properties, such as the grain size distribution, they are here calibrated on the basis of the available field observations rather than to use generic literature values. The estimation of SPM concentration thus first requires the calibration of the parameters γ and η in eq. (3.4) and eq. (3.6) respectively, using the concurrent remote sensing and in situ observations available.

A calibration procedure requires the minimization of a scalar error defining the departure of the model from observations in the plane (SPM, R_{rs}). Because both the observed SPM and $\widehat{R}_{rs}$ values are affected by relevant observation errors, a reasonable definition of distance between the model curve and the data points is the sum of the distances between curve and experimental points in the direction orthogonal to the curve itself. This involves using an Orthogonal Distance Regression (ODR, see Boggs et al. (1989, 1992); Zwolak et al. (2007)). However, there is some degree of subjectivity as to how the distance components along the two axes (SPM and R_{rs}, which have different units and represent different physical quantities) should

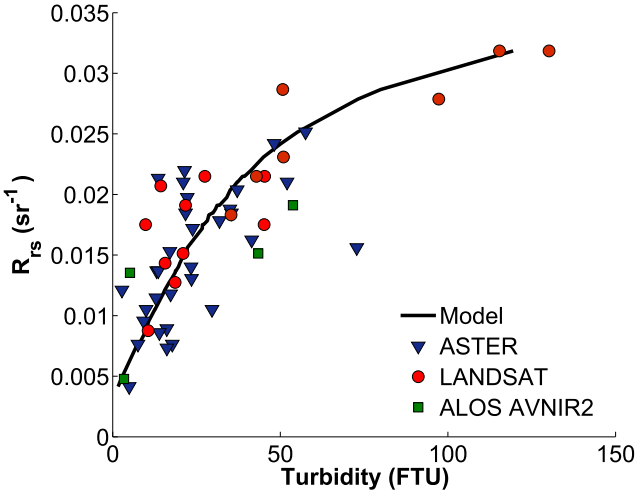

Figure 3.4: Calibration of the relation $R_{rs(SPM;H)}$ of the full set of 53 observations.

be rescaled in order to compute the point-to-curve distance. In particular, rescaling the observed reflectance and SPM values to the $[0, 1]$ interval, typical in the ODR literature, is not necessarily justified. In fact, because the interest is in estimating the SPM concentration, a second reasonable choice is minimizing the Root Mean Square Error (RMSE) in the direction of the SPM-axis. The implementation of both procedures gives that the results are similar and that the minimization of distances in the SPM direction produces smaller prediction errors in the validation phase. Only the results from the latter procedure will be described in what follows. The minimization of RMSE in the SPM direction produces the results represented in Fig. 3.4, with parameters $\eta = 0.4695\, m^2/g$ and $\gamma = 0.2044\, m^2/g$. It is important to emphasize here that Fig. 3.4 provides, for the sake of a more effective illustration, a cross-sectional representation in the (SPM, R_{rs}) plane of a relationship involving three quantities SPM, R_{rs}, and H. In fact, reflectance is a function of both SPM concentration and water depth, as seen in eqs (3.1) and (3.2).

After calibration of the absorption and backscattering parameters of

the retrieval procedure, the sensitivity of the retrieval scheme to different assumptions for the bottom reflectance value is addressed now. As noted above, the bottom sediment reflectance (at the chosen wavelength $\lambda = 644\,nm$) is here assumed to be $\rho_b = 0.027$ $\pi = 0.08$ (assuming the bottom sediment is a lambertian reflector), based on in situ observations.

Observed reflectance values in the literature range from 0.04 to 0.22 for silt and from 0.38 to 0.53 for sandy sediments (Durand et al., 2000; Albert & Mobley, 2003; Mobley, 2004). Because of the typically silty nature of the bottom sediment in the Venice lagoon, the possible values explored here lie in the range $0.04-0.25$ and allow to determine under what conditions important variations in the estimated SPM concentrations arise. It is seen (Figure 3.5), that variations in ρ_b induce differences in the retrieved values of SPM concentrations for relatively small water depths and turbidity. In particular, for a depth of 1.3 m, the range of bottom sediment reflectance values considered produces maximum deviations in the retrieved SPM concentration of about 15 FTU. Estimates of SPM concentration for intermediate values of SPM are moderately unaffected by the uncertainty in the bottom sediment reflectance (e.g. for $SPM = 20$ FTU the maximum deviation in the retrieved SPM concentration is about 30% depending on the assumed bottom reflectance). For high SPM concentrations the influence of the bottom reflectance vanishes.

In the following, the data corresponding to a water depth smaller than 1.3 m will thus be excluded from the calibration/validation process. For these locations the contribution of the bottom reflectance to the total reflectance would be greater than 10 % (for a reference SPM concentration of 20 FTU).

Validation is a fundamental phase in the development of an estimation procedure in order to provide an evaluation of the overall reliability of the retrieval scheme and a characterization of the uncertainty which should be associated with the estimated values. The model performance must be eval-

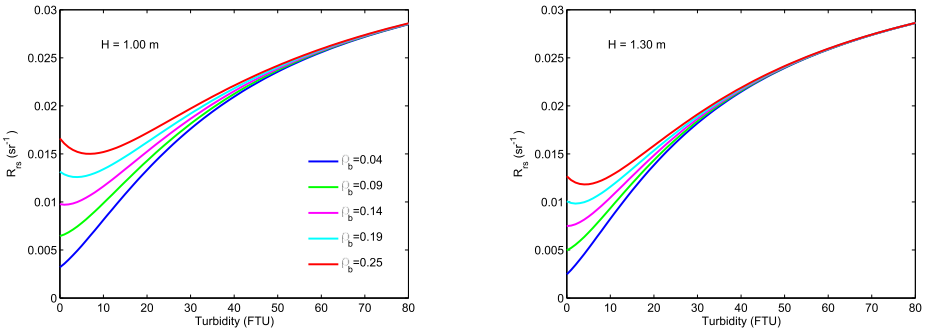

(a) (b)

(c)

Figure 3.5: Sensitivity of the model to different bottom reflectance values for different water depths: (a) $1\,m$, (b) $1.3\,m$ and (c) $2\,m$. The sensitivity of the retrieved SPM concentration values on the bottom albedo decreases rapidly with depth, such that its contribution to the total reflectance is down to about 10 % for $H = 1.3\,m$ a reference SPM concentration of 20 FTU.

uated on independent observations, i.e. observations which have not been used in the calibration phase. In order to obtain such an independent evaluation of the estimation error (i.e. the sum of errors i) to iii) discussed in Section 3.1), a leave-one-out cross-validation procedure (Wilks, 2006) has been adopted. In this procedure all but one observed (SPM, R_{rs}) pairs are used to calibrate the parameters of the retrieval model. An estimation error (observed SPM - estimated SPM) is then computed from the excluded (SPM, R_{rs}) pair. The procedure is repeated by excluding, in turn, all N available pairs ($N = 53$ in this case). The scatterplot comparing estimated and observed turbidity values from the leave-one-out procedure (Figure 3.6) shows the absence of a significant estimation bias (the average estimation error is about -1.1 FTU) and the relatively modest scatter between predicted and observed values (the error standard deviation is 14.3 FTU).

A cross-validation procedure was also applied to the estimation model obtained from the ODR regression scheme described above. The results yield an average estimation error of -24.0 FTU and a standard deviation of 79.6 FTU, showing that indeed the minimization of errors along the 'turbidity axis' provides more accurate SPM concentration predictions.

Leave-one-out cross-validation is useful to provide an overall assessment of the model accuracy. However, it does not allow an evaluation of the dependence of the estimation error on the turbidity value.

Previous contributions to the literature concerning SPM retrieval methods from remote sensing usually lack an assessment of the uncertainties involved in the estimation of suspended sediment concentration (or, more generally, of the water quality parameters of interest). This information, on the contrary, is extremely important when estimates are to be compared with in situ observations or with results from numerical models. The main sources of uncertainty in an algorithm for the retrieval of SPM concentration from remote sensing (but generalizations to other water parameters

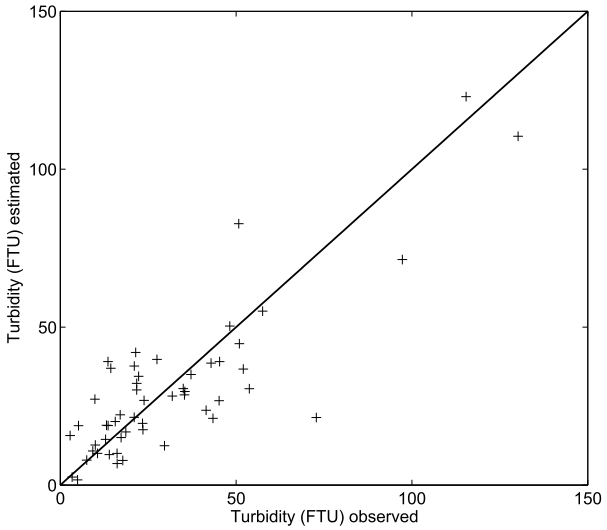

Figure 3.6: Scatterplot of estimated and observed turbidity values obtained from the leave-one-out procedure.

are quite straightforward) can be identified as i) uncertainties in the measurement of at-sensor radiances (the 'input' of the retrieval algorithm), ii) uncertainties in the model structure (e.g. due to simplifying assumptions and/or neglected processes), and iii) uncertainties in the determination of the parameters appearing in the model. Interestingly, even though statistical methods allowing a formal quantification of uncertainty are widely used in other disciplines (e.g. Montanari (2007)), they are seldom applied to remote sensing retrieval methods.

The quantitative assessment of the total estimation uncertainty (sum of i) through iii)) has been addressed through cross-validation, while the error induced in SPM concentration retrievals by the uncertain determination of model parameters (source iii)), often the dominant contribution to the overall uncertainty, will be now evaluated. This latter quantification is obtained by estimating the probability distribution of model parameters and of the associated uncertainty in SPM concentration retrievals using a non parametric

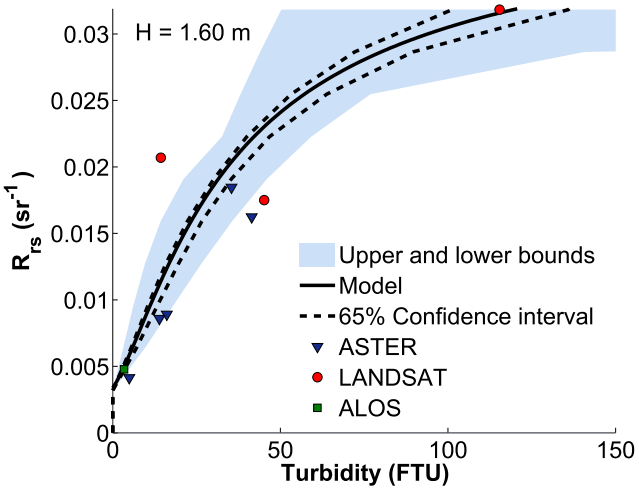

Figure 3.7: Determination of the confidence intervals for estimated turbidity values obtained from the bootstrap procedure. The dashed lines bound the 65 % confidence intervals. Only point observations for depths in the range 1.5-1.7 m are reported for comparison.

bootstrap method (Efron, 1979), in which the observed set of (SPM, R_{rs}) pairs is re-sampled with re-substitution (i.e. a pair that has been extracted is available for possible subsequent sampling). In the present case the observed set was resampled 10000 times, a number determined by making sure that a further increase in the number of pairs considered does not produce appreciably different results. This procedure essentially constructs a large number of samples from the same empirical distribution. The model is then calibrated on each of the re-sampled (SPM, R_{rs}) sets to obtain a sample of (10000) parameter values and a set of corresponding curves (which yield the shaded area in Figure 3.7).

Figure 3.8 represents the estimated probability density functions of the estimators of γ and η, obtained with the bootstrap method. The standard deviation is $0.062\,m^2/g$ for γ and $0.081\,m^2/g$ for η. For both the estimators, the mean value of the distribution is very close to the values obtained in the calibration using all the 53 experimental values. In the case of γ the mean

value of the distribution is $0.188\,m^2/g$, while calibration on the entire experimental dataset gives $0.204\,m^2/g$. For η, the mean value of the distribution is $0.446\,m^2/g$ and the result of model calibration is $0.469\,m^2/g$. This is a further confirmation of the robustness of the model calibration. Furthermore, the literature value for the backscattering coefficient ($\eta = 0.405\,m^2/g$ (Babin et al., 2003a)) also falls well within a standard deviation from the estimation mean. As for the absorption coefficient, the calibrated value is greater than literature values from comparable sites ($\gamma = 0.041\,m^2/g$ (Babin et al., 2003b)). However, the literature value taken here as a term of comparison corresponds to a secondary relative maximum in the estimated probability density function of this parameter.

The confidence intervals for SPM estimates are then obtained by the percentile method, by identifying the empirical 17.5% and 82.5% quantiles as a function of reflectance, as shown by the dashed lines in Figure 3.7. These confidence intervals have been calculated by inverting the model (3.1) for each pair of the bootstrap-estimated parameters. Due to the important influence of water depth this procedure was repeated for different values of H of applicative interest. Figure 3.7 shows a sample result for $H = 1.60\ m$. As discussed above, upper and lower bounds in figure 3.7 express the uncertainty induced in SPM concentration estimates by the uncertainty in parameter estimation as characterized by the different samples originated by the bootstrap procedure. It is important to note that other factors contribute to the observed differences between measured and estimated SPM concentrations. In particular, turbidimetric observations are also affected by significant uncertainty, which explains the spread of observational points beyond the bounds defined by parameter uncertainty.

Results for other values of the water depth are all very similar as indicated by the standard deviation values listed in Table 3.3 for a wide set reflectance and depth values. It can be noticed that the estimation standard

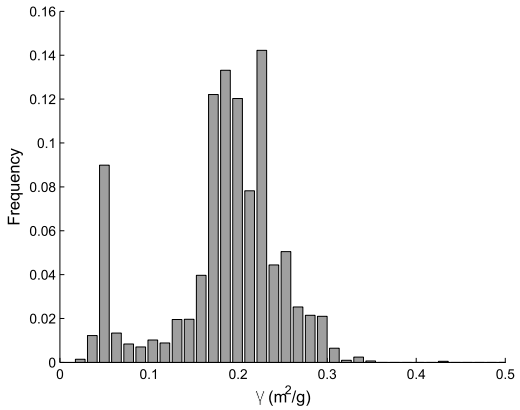

(a) Absorption

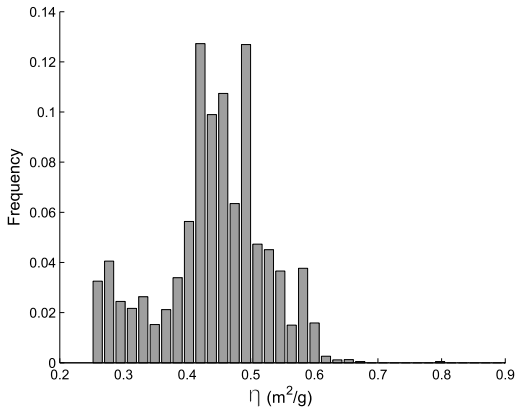

(b) Backscattering

Figure 3.8: Frequency distributions of the calibrated parameters obtained via bootstrap. The standard deviations are 0.062 m^2/g for γ and 0.081 m^2/g for η and the calibrated values lie close to the mean.

Table 3.3: Standard deviation of estimated turbidity via bootstrap (FTU), for different reflectance and depth values.

R_{rs}:	0	0.003	0.006	0.010	0.013	
h=1.30 m	$6.32E-12$	$1.52E-11$	0.79	1.68	2.33	
h=1.60 m	$2.00E-11$	$1.43E-10$	1.00	1.76	2.33	
h=1.90 m	$1.70E-12$	0.21	1.12	1.80	2.33	
h=10 m	$4.86E-09$	0.71	1.33	1.85	2.28	
R_{rs}:	0.016	0.019	0.022	0.025	0.029	0.032
h=1.30 m	2.82	3.17	3.63	5.31	11.24	34.02
h=1.60 m	2.76	3.07	3.56	5.43	11.57	34.35
h=1.90 m	2.72	3.01	3.54	5.53	11.76	34.51
h=10 m	2.61	2.90	3.54	5.69	11.97	34.66

deviation increases with reflectance (Table 3.3) and with turbidity (Figure 3.7).

3.3.2 Sediment Transport Model Output

In the northern part of the Adriatic Sea, and in the Venice lagoon in particular, a quite frequent meteorological condition is characterized by Scirocco wind, blowing from South-East and producing wind-driven water level set up which, combined with low atmospheric pressure, determines the well known high water conditions flooding the city of Venice. However, the most intense, morphologically significant wind is Bora blowing from North-East and generating the highest waves within the lagoon. These two meteorological conditions, and the case of Bora wind in particular, have been therefore considered in the numerical simulations performed by Carniello et al. (2011b) in order to test and calibrate the sediment transport model through the comparison with turbidity data collected within the lagoon by multi-parametric probes (LT stations in Figure 3.2).

As an example, Figure 3.9 shows the comparison of measured to computed suspended sediment concentrations at the LT6 station during the

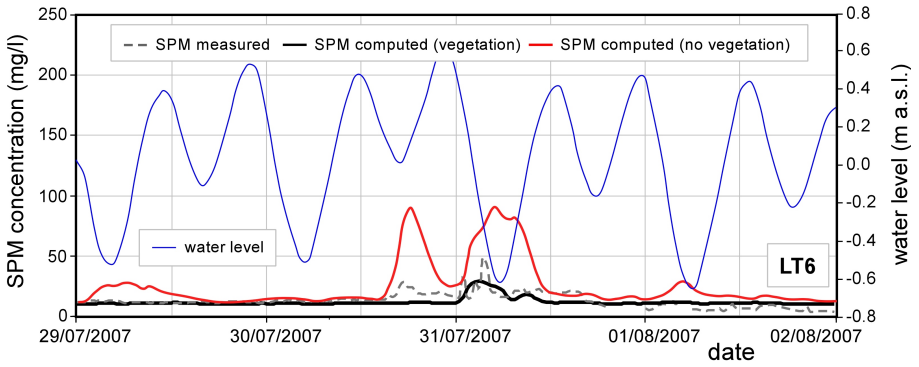

Figure 3.9: SPM concentration in LT6 station: comparison between observations (dashed) and model output without considering (black) and considering (red) the effect of vegetation. Water level oscillation is also shown (blue).

quite intense Bora event occurred in August 2007, characterized by wind speed up to 20 m/s. It is worth noting that LT6 station is the only one, among the available stations, which is located within the area colonized by benthic vegetation (see Figure 3.2). In spite of the intense windy condition actually forcing the lagoon, the suspended sediment concentration measured at the LT6 station is quite low and it is correctly reproduced by the model when the stabilizing effect of vegetation is accounted for assuming that vegetation density is high enough to completely prevent resuspension (i.e. the "resuspension coefficient" is set to zero). The same simulation has been performed by neglecting the presence of vegetation, the computed suspended sediment concentration turning out to be much higher than the measured one. The crucial role of vegetation in stabilizing the bottom sediment is thus confirmed.

3.3.3 Comparison between remote sensing- and model- retrieved maps

The calibrated and validated radiative transfer model was used to produce maps of turbidity for the satellite images available. The water depth, nec-

essary for the SPM concentration retrieval in eq. (3.1), was obtained from the hydrodynamic model.

Figure 3.10 shows a sample turbidity map produced using the ASTER data acquired on 24 June 2007. This information is complemented by the distribution of estimation accuracy (Figure 3.11), as represented by the estimation error standard deviation, which allows an immediate appreciation of the areas in which estimates are most reliable. The error standard deviation is quite small in the central and southern part of the Venice lagoon (values are between 0.2 and 3 FTU), while the maximum values (about 34 FTU) are observed in the northern and landward parts of the lagoon.

Turbidity values are, as expected, lower in the central part of the Lagoon, characterized by deeper waters, and in the main channels. This feature is consistently observed in all the acquisitions analyzed, as shown in Figure 3.12, which shows the spatial distribution of mean turbidity as computed from the set of images available. It is interesting to note that the particularly low turbidity values observed in the southern part of the lagoon may be connected to the presence of bottom vegetation. The red line in Figure 3.12 bounds the area where phanerogams occur (mainly *zostera marina* and *cymodocea nodosa*) as indicated by in situ mapping for 2004 (MAV, 2004)). It is seen that most of the areas with low average turbidity are indeed colonized by bottom vegetation, providing compelling evidence of the stabilizing effect exerted by macrophytes in tidal areas.

The SPM maps obtained from remote sensing images have been then compared to the results of the sediment transport model (Volpe et al., 2011a).

Fig. 3.13 shows a sample comparison among map produced using the Landsat data acquired on 8 December 2001 (a) and the results of the sediment transport model (b and c). Fig. 3.13(b) shows the results of the sediment transport model when no bottom vegetation is considered. In this

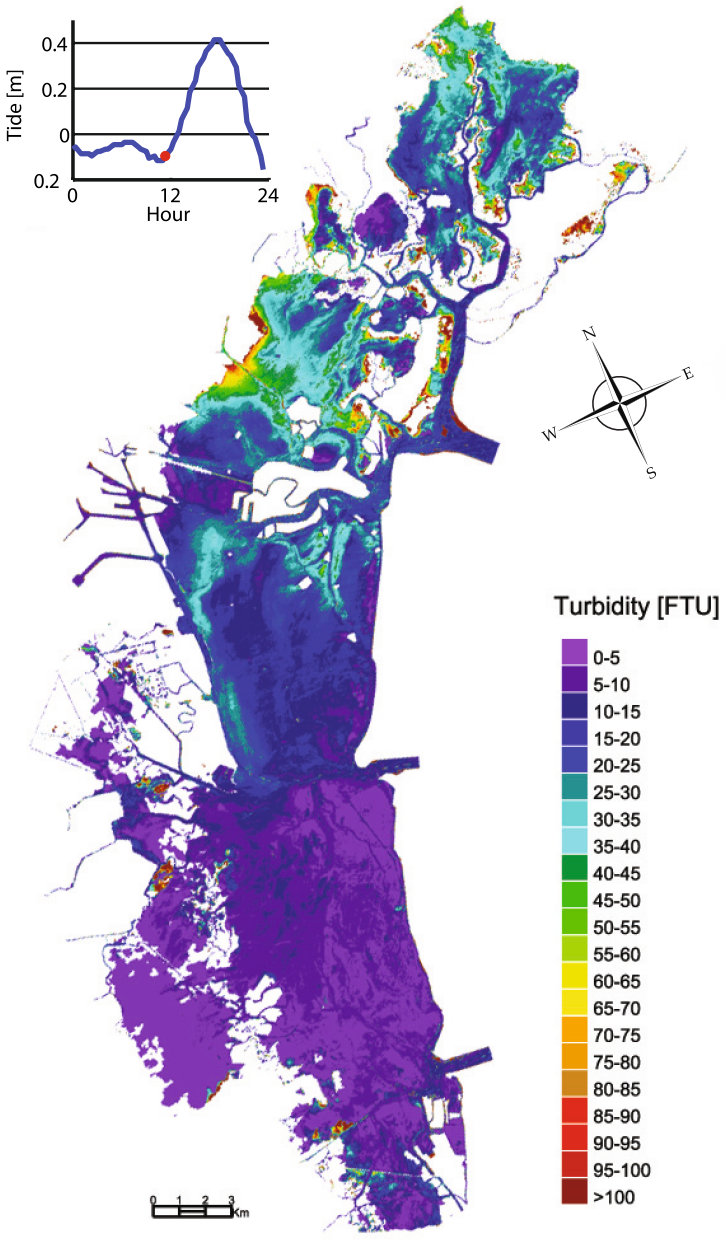

Figure 3.10: Map of estimated turbidity for the ASTER image acquired on 24 June 2007. The inset shows the day tidal oscillation and the tidal level at the moment of acquisition.

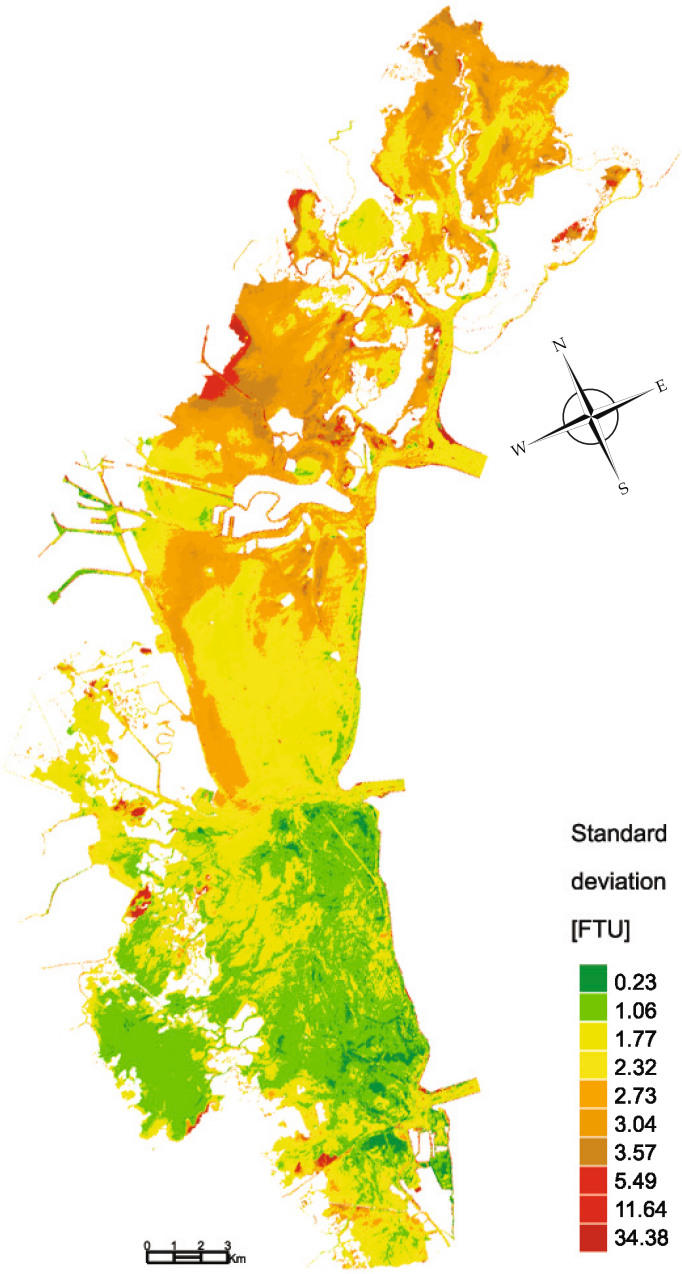

Figure 3.11: Map of the estimation error standard deviation for the ASTER image acquired on 24 June 2007 computed on the basis of the values in Table 3.3.

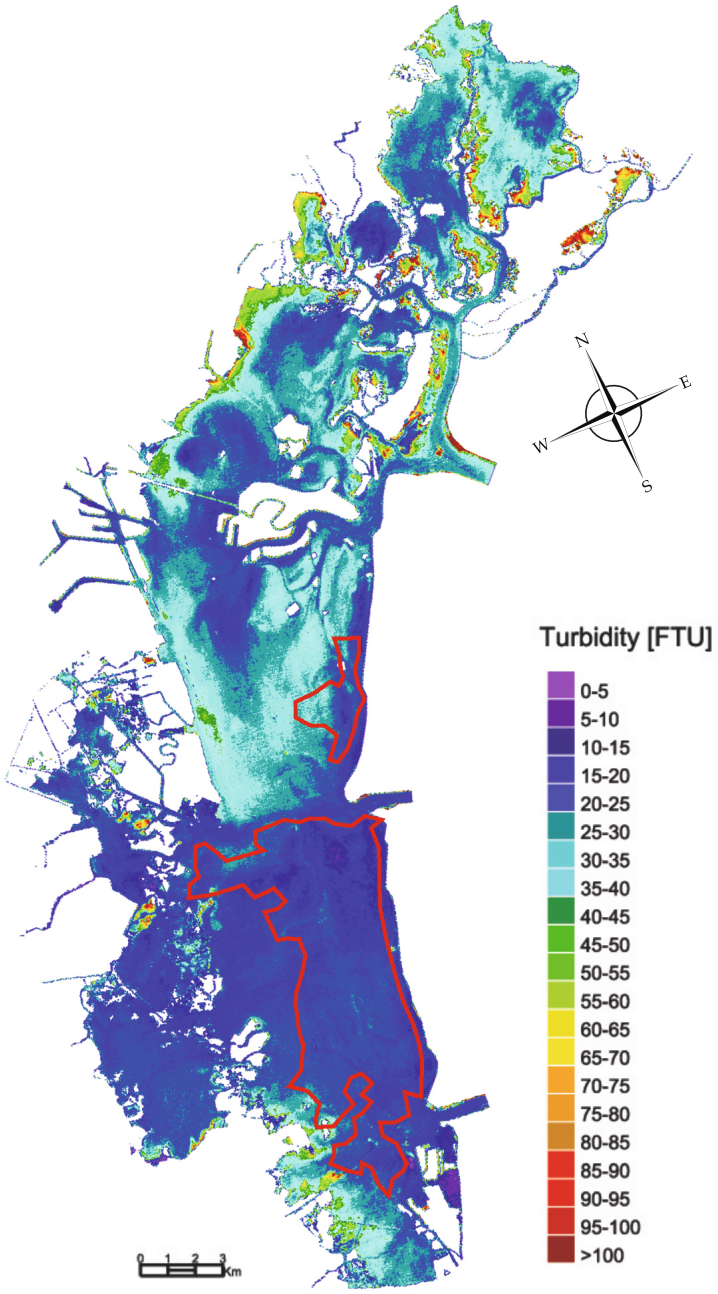

Figure 3.12: Map of mean turbidity as computed from the set of available images. The red shape represents the area where macrophytes plants are present.

first case, a marked difference can be noticed with the satellite image map in the southern part of the lagoon, where the model clearly overestimates the SPM concentration. This overestimation is common in all the events considered in the study: all the satellite retrievals indicate low turbidity values in the south-eastern part of the lagoon, where, on the contrary, the results from the model give relatively high concentrations.

In the northern part of the lagoon, a disagreement is detected where water depth is very low: in these areas the turbidity value retrieved from remote sensing is probably affected by the bottom reflectance signal. It is worth to recall here that the accuracy of the remote sensing retrieval scheme declines with water depth and for low SPM concentrations (Volpe et al., 2011c).

In the central and southern part of the lagoon, where water depth is greater, the estimates from remote sensing are to be considered reliable. A very good agreement can be noticed with the model output of SPM concentration patterns in the central part but, as noticed above, the model overestimates observations in the south-eastern part between the Chioggia and the Malamocco inlets.

Figure 3.13(c) shows the result of the model when a reduction factor is considered for the sediment resuspension. The reduction factor was applied in the model for the portion of the domain within the red dashed area in Figure 3.2: this area corresponds to the zones where phanerogams were observed during a field campaign conducted throughout a year in 2004 (MAV, 2004). It is interesting that most of the areas with low average turbidity detected from remote sensing and overestimated by the numerical model are indeed colonized by bottom vegetation, providing compelling evidence of the stabilizing effect exerted by macrophytes in tidal areas.

The agreement between modelled and satellite-retrieved SPM concentration is now much more satisfactory, giving evidence that the effect of

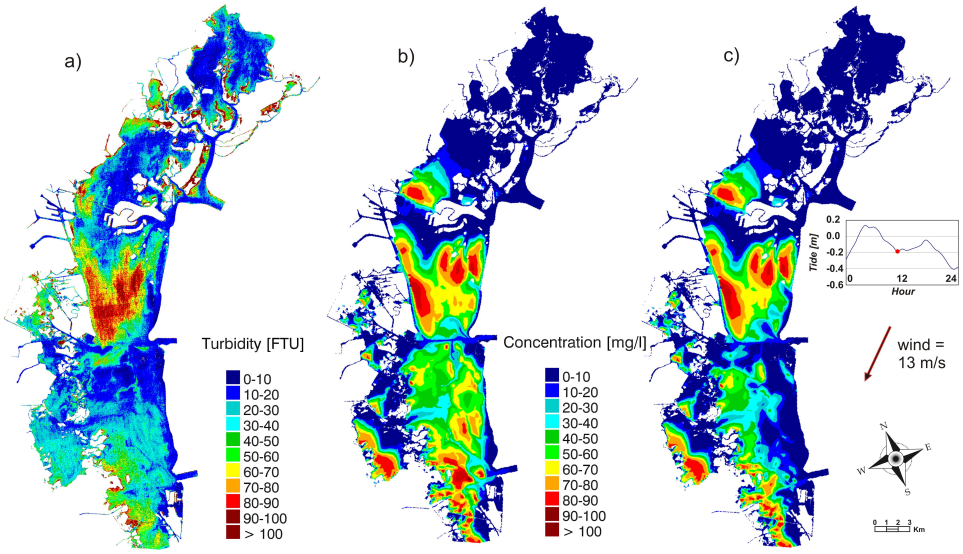

Figure 3.13: Comparison between SPM concentration maps retrieved from Landsat satellite image on December 8, 2001 (a) and modelled concentration without vegetation effects (b) and considering vegetation (c).

submerged vegetation cannot be neglected in modelling the sediment transport in shallow areas.

Figure 3.14 shows the same comparisons giving the same results for another acquisition.

3.4 Discussion

The SPM concentration retrieval algorithm from remote sensing data applied in this Chapter performs well according to the leave-one-out cross-validation procedure applied, with negligible bias and an overall error standard deviation of about 14 FTU. The formal bootstrap method applied allowed the determination of estimation confidence intervals quantifying the uncertainty associated with model parameters. The confidence interval defined is, as expected, wider for larger FTU values.

The statistical distributions of absorption and back-scattering parame-

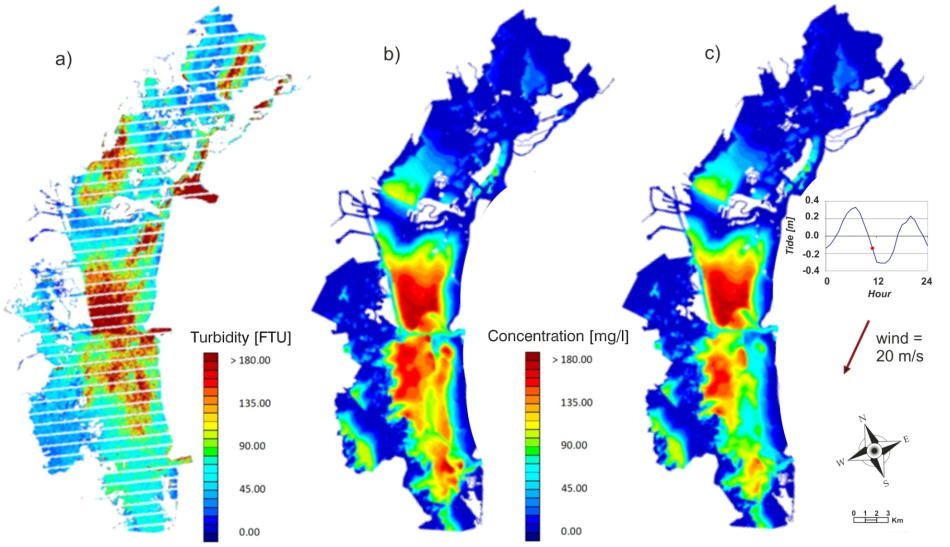

Figure 3.14: Comparison between SPM concentration maps retrieved from Landsat satellite image on December 11, 2005 (a) and modelled concentration without vegetation effects (b) and considering vegetation (c).

ters obtained from the bootstrap procedure yields coefficients which are coherent with those from the existing literature on coastal areas in the Adriatic sea. This is not an obvious result, as the optical properties of suspended sediments depend (at least) on the grain size distribution, which is expected to be significantly different in lagoons (where fines are typically abundant) with respect to coastal seas.

A distinct advantage of the proposed methodology, making use of a bootstrap technique, is the possibility to produce sediment concentration maps along with the associated uncertainty maps. This immediately allows the identification of the areas where remote sensing estimates may be considered to be reliable.

The inversion of the radiative transfer model allows to conclude that the bottom albedo does not significantly affect the SPM concentration estimates for the turbidity values of typical interest in sediment transport studies, i.e. for moderate to large turbidity values and greater water depths. This is for

example important when attempting to identify erosion hotspots and areas where sediment fluxes are relatively large, thus giving the largest contribution to the overall sediment budget.

The retrieval method was here developed and applied on the basis of satellite observations from different sensors. The sensors explored here yield retrievals which are quite consistent, implying that the atmospheric correction scheme applied allows an accurate determination of surface reflectance. The possibility of using different platforms with homogeneous results significantly indicates that monitoring and analysis procedures based on remote sensing can exploit the full range of existing sensors. While satellite data allow one to draw from a large existing database of past observations, interesting applications of the proposed algorithm can be envisioned using airborne and proximal sensors. Airborne sensors can be used to perform targeted and high-resolution surveys during intense re-suspension events, which play a dominant role in determining the morphodynamic evolution of estuaries and lagoons. Proximal sensors, e.g. mounted on fixed and tall structures, could be used to provide a continuous monitoring of suspended sediment in areas of particular interest (e.g. tidal inlets, where the overall sediment budget can be computed), with accuracies rivaling those obtainable from turbidity sensors (particularly if uncalibrated) and acoustic devices (e.g. ADCP's) and with a much wider areal coverage. In these settings the method developed here to assess the uncertainty associated with the estimations is of particular importance, in order to provide a measure of the accuracy with which the sediment budget can be described.

The algorithms for the estimation of the suspended sediment concentration and of the associated uncertainty are thus shown to allow reliable and repeatable SPM concentration estimates even in shallow intertidal areas, where remote sensing methods were previously applied with limited success and where alternative methods of observation can only provide point

measurements of limited use in closing the sediment budget.

The results highlight the importance of benthic vegetation in the stabilization of the bottom sediment in shallow waters. The concurrent use of remote sensing retrievals of SPM concentrations and of a finite element model of suspended sediment dynamics showed that an improved agreement between the two can only be obtained if benthic vegetation is assumed to exert a significant stabilization effects over large spatial scales. This finding allows one to conclude that biostabilization processes, typically addressed in the laboratory or at limited field scales (e.g. Madsen et al. (2001)), are extremely important at the scale of the entire system, with implications for its global erosional/depositional trends. The results show, in a spatially explicit context, the key importance of the interaction between submerged vegetation and sediment dynamics with consequences for the strength of the positive feedbacks suggested to exist between biostabilization and light penetration (Carr et al., 2010).

This work also emphasizes the importance of the spatially-distributed validation of numerical models, which can be performed with the aid of remote sensing techniques. The analyses performed strongly suggest that large errors can be produced when just point observations are used for the calibration/validation procedures, particularly due to the highly heterogeneous physical and bio-geomorphological properties of intertidal areas.

Further improvements may be expected if remote sensing is used to retrieve a wider variety of water quality properties beside SPM, allowing to impose stronger constraints on hydrodynamic and transport models.

Conclusions and Perspectives

The multi-layer root-water-uptake model developed is coherent with field measurements of soil moisture and plant transpiration, and it reproduces hydraulic lift mechanism without any *a priori* assumptions or empirical parameters, but just based on continuity equation of water flow in the soil-plant-atmosphere pathway. The approach employed allows to directly take into account stress factors such as water or salt stress, which affect the water potential in the soil. Some climate change scenarios have been explored, by increasing the ambient CO_2 concentration and air temperature. The results show that evapotranspiration increases with temperature but decreases with CO_2, photosynthesis significantly increases under high CO_2, while very negligible effects are shown for hydraulic lift. Three root distribution functions are compared and the constant distribution results the more efficient in maximizing evapotranspiration with respect to the linear and the exponential ones.

Salinity is a well known stress factor in coastal areas and it affects not only the osmotic potential in the soil, but also plant photosynthesis through stomatal limitation and metabolic impairment. A model for leaf gas exchange based on the maximization of the carbon gain subject to a limitation of the water loss is extended to include the effects of salt stress. The revised optimality model explicitly includes the mesophyll conductance and its dependence on water salinity. The optimization problem is solved numerically for a non-linear biochemical demand function, and analytically for

a linearized biochemical demand function. Both models reproduced well gas exchange measurements collected for olive trees and spinach plants in fresh water and in salt stressed conditions. As a result of salt stress, the maximum carboxylation capacity was reduced by $30 - 40\%$, while the parameter indicating the cost of water (or marginal water use efficiency) increased. Hence, reductions in photosynthetic rates observed under increased salt stress are not only due to a limitation of CO_2 diffusion, but also caused by a direct salinity effect on the metabolic apparatus of the plant. The model scenarios simulating the compound effect of salinity stress and increasing atmospheric CO_2 concentration showed that the reduction in stomatal conductance and the increase of photosynthesis under elevated CO_2 concentration are slightly affected by salinty stress.

As a future application, the proposed leaf level approach can be readily incorporated into physically based models of the soil-plant-atmosphere system to assess how saline conditions and elevated atmospheric CO_2 jointly impact transpiration and photosynthesis.

Finally, the consistency between remotely-sensed and modelled suspended sediment concentration distributions, and their coherence with known features in the Venice lagoon point to the important role played by benthic vegetation in the stabilization of the bottom sediment at the scale of the entire system suggesting that biostabilization plays a major control of the overall bio-geomorphic evolution of coastal areas.

Bibliography

Abdul-Jabbar, A., Lugg, D., Sammis, T., & Gay, L. (1984). A field study of plant resistance to water flow in alfalfa. *Agronomy Journal*, 76, 765–769.

Ainsworth, A. & Rogers, A. (2007). The response of photosynthesis and stomatal conductance to rising [CO_2]: mechanisms and environmental interactions. *Plant, Cell and Environment*, 30, 258–270.

Albert, A. & Mobley, C. (2003). An analytical model for subsurface irradiance and remote sensing reflectance in deep and shallow case-2 waters. *Optical Society of America*, 11(22).

Armanini, A. (1995). Non-uniform sediment transport: dynamics of the active layer. *Journal of Hydraulic Research*, 33(5), 611–622.

Armanini, A. & Silvio, G. D. (1988). A one-dimensional model for the transport of a sediment mixture in non-equilibrium conditions. *Journal of Hydraulic Research*, 26(3), 275–292.

Arneth, A., Lloyd, J., Santruckova, H., Bird, M., Grigoryev, S., Kalaschnikov, N., Gleixner, G., & Schulze, E. (2002). Response of central *Siberian Scots* pine to soil water deficit and long-termtrends in atmospheric CO_2 concentration. *Global Biogeochemical Cycles*, 16, 1005–1016.

Babin, M., Morel, A., Fournier-Sicre, V., Fell, F., & Stramski, D. (2003a). Light scattering properties of marine particles in coastal and open ocean

waters as related to the particle mass concentration. *Limnology and Oceanography*, 48(2), 843–859.

Babin, M., Stramski, D., Ferrari, G., Claustre, H., Bricaud, A., Obolensky, G., & Hoepffner, N. (2003b). Variations in the light absorption coefficients of phytoplankton, nonalgal particles, and dissolved organic matter in coastal waters around Europe. *Journal of Geophysical Research*, 108(C7).

Ball, M. & Farquhar, G. (1984). Photosynthetic and stomatal responses of two mangrove species, *Aegiceras corniculatum* and *Avicennia marina*, to long term salinity and humidity conditions. *Plant Physiology*, 74, 1–6.

Berninger, F. & Hari, P. (1993). Optimal regulation of gas-exchange evidence from field data. *Annals of Botany*, 71, 135–140.

Binding, C., Bowers, D., & Mitchelson-Jacob, E. (2005). Estimating suspended sediment concentrations from ocean colour measurements in moderately turbid waters: the impact of variable particle scattering properties. *Remote Sensing of Environment*, 94, 373–383.

Boer, H. D., Lammertsma, E., Wagner-Cremer, F., Dilcher, D., Wassen, M., & Dekker, S. (2011). Climate forcing due to optimization of maximal leaf conductance in subtropical vegetation under rising CO_2. *Proceedings of the National Academy of Sciences*, 108(10), 4041–4046.

Boggs, P., Byrd, R., Rogers, J., & Schnabel, R. (1992). *User's reference Guide for ODRPACK Version 2.01: Software for Weighted Orthogonal Distance Regression.* Technical report, U.S. Department of Commerce, National Institute of Standards and Technology, Gaithersburg, MD 20899.

Boggs, P., Donaldson, J., Byrd, R., & Schnabel, R. (1989). ALGORITHM 676 - ODRPACK: Software for Weighted Orthogonal Distance Regression. *ACM Transactions on Mathematical Software*, 15(4), 348–364.

Bongi, G. & Loreto, F. (1989). Gas-exchange properties of salt-stressed olive (*Olea europea L.*) leaves. *Plant Physiology*, 90, 1408–1416.

Bowers, D. & Binding, C. (2006). The optical properties of mineral suspended particles: A review and synthesis. *Estuarine, Coastal and Shelf Science*, 67, 219–130.

Brady, N. & Weil, R. (2002). *The Nature and Properties of Soils*. Technical report, Upper Saddle River, New Jersey, Prentice Hall.

Brando, V., Anstee, J., Wettle, M., Dekker, A., Phinn, S., & Roelfsema, C. (2009). A physics based retrieval and quality assessment of bathymetry from suboptimal hyperspectral data. *Remote Sensing of Environment*, 113, 755–770.

Braud, I., Dantas-Antonino, A., Vauclin, M., Thony, J., & Ruelle, P. (1995). A simple soil-plant-atmosphere transfer model (SiSPAT) development and field verification. *Journal of Hydrology*, 166, 213–250.

Braud, I., Varado, N., & Olioso, A. (2005). Comparison of root water uptake modules using either the surface energy balance or potential transpiration. *Journal of Hydrology*, 301, 267–286.

Brocchini, M., Wurtele, M., Umgiesser, G., & Zecchetto, S. (1995). Calculation of a mass-consistent two-dimensional wind-field with divergence control. *Journal Of Applied Meteorology*, 34(11), 2543–2555.

Brugnoli, E. & Lauteri, M. (1991). Effects of salinity on stomatal conductance, photosynthetic capacity, and carbon isotope discrimination of salt-tolerant (*Gossypium hirsutum L.*) and salt-sensitive (*Phaseolus vulgaris L.*) C3 non-halophytes. *Plant Physiology*, 95, 628–635.

Buckley, T., Mott, K., & Farquhar, G. (2003). A hydromechanical and

biochemical model of stomatal conductance. *Plant, Cell and Environment*, 26, 1767–1785.

Calatayud, A., Iglesias, D., Taln, M., & Barreno, E. (2003). Effects of 2-month ozone exposure in spinach leaves on photosynthesis, antioxidant systems and lipid peroxidation. *Plant Physiology and Biochemistry*, 41, 839–845.

Caldwell, M., Dawson, T., & Richards, J. (1998). Hydraulic lift: consequences of water efflux from the roots of plants. *Oecologia*, 113, 151–161.

Camin, F., Bontempo, L., Ziller, L., Piangiolino, C., & Morchio, G. (2010). Stable isotope ratios of carbon and hydrogen to distinguish olive oil from shark squalene-squalane. *Rapid Communications in Mass Spectrometry*, 24, 1810–1816.

Campbell, G. & Norman, J. (1998). *An introduction to environmental biophysics*. 2nd edn. New York, NY: Springer-Verlag.

Carniello, L., D'Alpaos, A., & Defina, A. (2011a). Modeling wind-waves and tidal flows in shallow microtidal basins. *Estuarine Coastal and Shelf Science*, doi:10.1016/j.ecss. 2011.01.001.

Carniello, L., Defina, A., , & D'Alpaos, L. (2008). Un modello di trasporto solido in sospensione per miscele bigranulari: prime applicazioni alla laguna di venezia. *Atti del XXXI Convegno di Idraulica e Costruzioni Idrauliche, Perugia, Morlacchi Editore*, pag 204.

Carniello, L., Defina, A., , & D'Alpaos, L. (2009). Morphological evolution of the venice lagoon: evidence from the past and trend for the future. *Journal of Geophysical Research - Earth Surface*, 114, F04002, doi:10.1029/2008JF001157.

Carniello, L., Defina, A., & D'Alpaos, A. (2011b). Sand-mud sediment transport induced by tidal currents and wind waves in shallow microtidal basins. *Submitted*.

Carniello, L., Defina, A., Fagherazzi, S., & D'Alpaos, L. (2005). A combined wind wave−tidal model for the Venice lagoon. *Journal of Geophysical Research*, 110, F04007, doi:10.1029/2004JF000232.

Carr, J., D'Odorico, P., McGlathery, K., & Wiberg, P. (2010). Stability and bistability of seagrass ecosystems in shallow coastal lagoons: Role of feedbacks with sediment resuspension and light attenuation. *Journal of Geophysical Research*, 115, G03011, doi:10.1029/2009JG001103.

Cattrall, C. & Thome, K. J. (2003). Exploitation of MODTRAN 4 capabilities to predict at-sensor radiance. *Optical Spectroscopic Techniques and Instrumentation for Atmospheric and Space Research*, 5157, 98–106.

Centritto, M., Loreto, F., & Chartzoulakis, K. (2003). The use of low [CO_2] to estimate diffusional and non-diffusional limitations of photosynthetic capacity of salt-stressed olive saplings. *Plant, Cell and Environment*, 26, 585–594.

Chaves, M., Flexas, J., & Pinheiro, C. (2009). Photosynthesis under drought and salt stress: regulation mechanisms from whole plant to cell. *Annals of Botany*, 103, 551–560.

Chen, Q., Zhang, Y., & Hallikainen, M. (2007a). Water quality monitoring using remote sensing in support of the EU water framework directive (WFD): A case study in the Gulf of Finland. *Environmental Monitoring Assessment*, 124, 157–166.

Chen, Z., Hu, C., & Muller-Karger, F. (2007b). Monitoring turbidity in Tampa Bay using MODIS/Aqua 250-m imagery. *Remote Sensing of Environment*, 109, 207–220.

Clapp, R. & Hornberger, G. (1978). Empirical equations for some soil hydraulic properties. *Water Resources Research*, 14, 601–4.

Coleman, T. & Li, Y. (1994). On the convergence of reflective newton methods for large-scale nonlinear minimization subject to bounds. *Mathematical Programming*, 67, 2, 189–224.

Coleman, T. & Li, Y. (1996). An interior, trust region approach for nonlinear minimization subject to bounds. *SIAM Journal on Optimization*, 6, 418–445.

Collatz, G., Ball, J., Grivet, C., & Berry, J. (1991). Physiological and environmental-regulation of stomatal conductance, photosynthesis and transpiration: a model that includes a laminar boundary-layer. *Agricultural and Forest Meteorology*, 54, 107–136.

Collins, D. & Bras, R. (2007). Plant rooting strategies in water-limited ecosystems. *Water Resources Research*, 43, W06407, doi:10.1029/2006WR005541.

Cowan, I. & Farquhar, G. (1977). Stomatal function in relation to leaf metabolism and environment. *In: Integration of activity in the higher plant. Symposia of Society of Experimental Biology. Cambridge: Cambridge University Press*, 31, 471–505.

Cressman, G. (1959). An operational objective analysis system. *Monthly Weather Review*, 87, 367–374.

D'Alpaos, L. & Defina, A. (2007). Mathematical modeling of tidal hydrodynamics in shallow lagoons: A review of open issues and applications to the venice lagoon. *Computers and Geosciences*, 33, 476–496, doi:10.1016/j.cageo.2006.07.009.

D'Alpaos, L. & Martini, L. (2003). *The influence of inlet configuration on sediment loss in the Venice Lagoon.* Technical report, Proc. of Flooding and Environmental Challenges for Venice and its Lagoon: State of Knowledge, Cambridge.

Daly, E., Porporato, A., & Rodriguez-Iturbe, I. (2004). Coupled dynamics of photosynthesis, transpiration, and soil water balance. part I: Upscaling from hourly to daily level. *Journal of Hydrometeorology*, 5, 546–558.

Dawson, T. (1993). Hydraulic lift and water use by plants: implications for water balance, performance, and plantplant interactions. *Oecologia*, 95, 565–574.

Day, J., Rybczyk, J., Scarton, F., Rismondo, A., Are, D., & Cecconi, G. (1999). Soil accretionary dynamics, sea-level rise and the survival of wetlands in venice lagoon: A field and modelling approach. *Estuarine Coastal and. Shelf Science*, 49 (5), 607–628.

Defina, A. (2000). Two-dimensional shallow water equations for partially dry areas. *Water Resources Research*, 36, 3251–3264.

Defina, A., Carniello, L., Fagherazzi, S., & D'Alpaos, L. (2007). Self organization of shallow basins in tidal flats and salt marshes. *Journal of Geophysical Research - Earth Surface*, 112(F3), doi:10.1029/2006JF000550.

Dekker, A., Vos, R., & Peters, S. (2001). Comparison of remote sensing data, model results and in situ data for total suspended matter (TSM) in the southern Frisian lakes. *The Science of the Total Environment*, 268, 197–214.

Delfine, S., Alvino, A., Villani, M., & Loreto, F. (1999). Restrictions to carbon dioxide conductance and photosynthesis in spinach leaves recovering from salt stress. *Plant Physiology*, 119, 395–402.

Delfine, S., Alvino, A., Zacchini, M., & Loreto, F. (1998). Consequences of salt stress on conductance to CO2 diffusion, rubisco characteristics and anatomy of spinach leaves. *Australian Journal of Plant Physiology*, 25, 395–402.

Dewar, R. (2002). The BallBerryLeuning and TardieuDavies stomatal models: synthesis and extension within a spatially aggregated picture of guard cell function. *Plant, Cell and Environment*, 25, 1383–1398.

Díaz-Espejo, A., Walcroft, A., Fernández, J., Hafidi, B., Palomo, M., & Girón, I. (2006). Modeling photosynthesis in olive leaves under drought conditions. *Tree Physiology*, 26, 1445–1456.

Domec, J., King, J., Noormets, A., Treasure, E., Gavazzi, M., Sun, G., & McNulty, S. (2010). Hydraulic redistribution of soil water by roots affects whole-stand evapotranspiration and net ecosystem carbon exchange. *New Phytologist*, 187, 171–183.

Doussan, C., Pierret, A., Garrigues, E., & Pagés, L. (2006). Water uptake by plant roots: II - Modeling of water transfer in the soil root-system with explicit account of flow within the root system - Comparison with experiments. *Plant and Soil*, 283, 99–117.

Downton, W., Grant, W., & Robinson, S. (1985). Photosynthetic and stomatal responses of spinach leaves to salt stress. *Plant Physiology*, 77, 85–88.

Durand, D., Bijaoui, J., & Cauneau, F. (2000). Optical remote sensing of shallow-water environmental parameters: A feasibility study. *Remote Sensing of Environment*, 73, 152–161.

Efron, B. (1979). Bootstrap methods: another look at the Jackknife. *The Annals of Statistics*, 7(1), 1–26.

Egea, G., Verhoef, A., & Vidale, P. (2011). Towards an improved and more flexible representation of water stress in coupled photosynthesis-stomatal conductance models. *Agricultural and Forest Meteorology*, 151, 1370–1384.

Ekercin, S. (2007). Water Quality Retrievals from High Resolution Ikonos Multispectral Imagery: A Case Study in Istanbul, Turkey. *Water, Air & Soil Pollution*, 183, 239–251.

Ellsworth, D., Thomas, R., Crous, K., Palmroth, S., Ward, E., Maier, C., Delucia, E., & Oren, R. (2011). Elevated CO2 effects on photosynthetic responses to light and [CO2] over ten years: A synthesis from Duke FACE. *Global Change Biology*, (pp. in press).

Fagherazzi, S., Marani, M., & Blum, L. (2004). *Ecogeomorphology of Tidal Marshes*. American Geophysical Union, Coastal and Estuarine Monograph Series, Washington (Ed.).

Fagherazzi, S., Palermo, C., Rulli, M. C., Carniello, L., & Defina, A. (2007). Wind waves in shallow microtidal basins and the dynamic equilibrium of tidal flats. *Journal of Geophysical Research*, 112(F02024).

FAO (2005). *20 things to know about the impact of salt water on agricultural land in ACEH province*. Technical report, FAO Field Guide, Food and Agricultural Organization, `http://www.fao.org/ag/tsunami/docs/saltwater-guide.pdf`.

Farquhar, G., Caemmerer, S., & Berry, J. (1980). A biochemical-model of photosynthetic CO_2 assimilation in leaves of C-3 species. *Planta*, 149, 78–90.

Feddes, R., Hoff, H., Bruen, M., Dawson, T., de Rosnay, P., Dirmeyer, P., Jackson, R., Kabat, P., Kleidon, A., Lilly, A., & Pitmank, A. (2001). Modeling root water uptake in hydrological and climate models. *Bulletin of the American Meteorological Society*, 82(12), 2797–2809.

Feddes, R., Kowalik, P., & Zaradny, H. (1978). *Simulation of Field Water Use and Crop Yield*. Simulation Monograph. Pudoc, Wageningen, The Netherlands.

Feddes, R. & Raats, P. (2004). Parameterizing the soilwater-plant root system. In d. R. G. Feddes R.A. & van Dam J.C. (Eds.) (Eds.), *Unsaturated-zone Modeling: Progress, Challenges, Applications* chapter 4, (pp. 95–141). *http* : $//library.wur.nl/frontis/unsaturated/toc_unsaturated.html$: Wageningen UR Frontis Series.

Ferrari, G. & Tassan, S. (1991). On the accuracy of determining light absorption by yellow substances through measurements of induced fluorescence. *Limnology and Oceanography*, 36(4), 777–786.

Fisher, J., DeBiase, T., Qi, Y., Xu, M., & Goldstein, A. (2005). Evapotranspiration models compared on a sierra nevada forest ecosystem. *Environmental Modelling & Software*, 20, 783–796.

Flexas, J., Bota, J., Loreto, F., Cornic, G., & Sharkey, T. (2004). Diffusive and metabolic limitations to photosynthesis under drought and salinity in C3 plants. *Plant Biology*, 6, 1–11.

Gallegos, C. & Correl, D. (1990). Modeling spectral diffuse attenuation, absorption and scattering coefficients in a turbid estuary. *Limnology and Oceanography*, 35(7), 1486–1502.

Gambolati, G. (2002). *Lezioni di Metodi Numerici per Ingegneria e Scienze Applicate*. Edizioni Libreria Cortina Padova.

Gardner, W. (1965). Dynamic aspects of soil-water availability to plants. *Annual Review of Plant Physiology*, 16, 323–342.

Gedan, K. B., Silliman, B., & Bertness, M. (2009). Centuries of human-driven change in salt marsh ecosystems. *Annual Review of Marine Science*, 41, 1–117, 10.1146/annurev.marine.010908.163930.

Geissler, N., Hussin, S., & Koyro, H. (2009). Elevated atmospheric CO_2 concentration ameliorates effects of NaCl salinity on photosynthesis and leaf structure of Aster tripolium L. *Journal of Experimental Botany*, 60(1), 137–151.

Giardino, C., Brando, V. E., Dekker, A. G., Strmbeck, N., & Candiani, G. (2007). Assessment of water quality in Lake Garda (Italy) using Hyperion. *Remote Sensing of Environment*, 109, 183–195.

Givnish, T. & Vermeij, G. (1976). Sizes and shapes of liane leaves. *The American Naturalist*, 110, 743–778.

Gran, M., Carrera, J., Massana, J., Saaltink, M., Olivella, S., Ayora, C., & Lloret, A. (2011). Dynamics of water vapor flux and water separation processes during evaporation from a salty dry soil. *Journal of Hydrology*, 396, 215–220.

Guswa, A., Celia, M., & Rodriguez-Iturbe, I. (2002). Models of soil moisture dynamics in ecohydrology: A comparative study. *Water Resources Research*, 38(9), doi:10.1029/2001WR000826.

Hao, X., Zhang, R., & Kravchenko, A. (2005). Effects of root density distribution models on root water uptake and water flow under irrigation. *Soil Science*, 170, 167–174.

Hari, P., Mäkelä, A., Berninger, F., & Pohja, T. (1999). Field evidence for the optimality hypothesis of gas exchange in plants. *Australian Journal of Plant Physiology*, 26, 239–244.

Hari, P., Mäkelä, A., Korpilahti, E., & Holmberg, M. (1986). Optimal control of gas exchange. *Tree Physiology*, 32, 169–176.

Hari, P., Mäkelä, A., & Pohja, T. (2000). Surprising implications of the optimality hypothesis of stomatal regulation gain support in a field test. *Australian Journal of Plant Physiology*, 27, 77–80.

Harley, P., Loreto, F., Marco, G. D., & Sharkey, T. (1992). Theoretical considerations when estimating the mesophyll conductance to CO_2 flux by analysis of the response of photosynthesis to CO_2. *Plant Physiology*, 98, 1429–1436.

Hirano, M. (1971). River bed degradation with armouring. *Transactions Japan Society of Civil Engineers*, 3, 194–195.

Hirano, M. (1972). Studies on variation and equilibrium state of a river bed composed of non-uniform material. *Transactions Japan Society of Civil Engineers*, 4, 128–129.

Holthuijsen, L., Booij, N., & Grant, W. (1989). A prediction model for stationary, short-crested waves in shallow water with ambient currents. *Coastal Engineering*, 13, 23–54.

Homaee, M., Dirksen, C., & Feddes, R. (2002a). Simulation of root water uptake I. Non-uniform transient salinity stress using different macroscopic reduction functions. *Agricultural Water Management*, 57, 89–109.

Homaee, M., Feddes, R., & Dirksen, C. (2002b). Simulation of root water uptake. II. Non-uniform transient water stress using different reduction functions. *Agricultural Water Management*, 57, 111–126.

Homaee, M., Feddes, R., & Dirksen, C. (2002c). Simulation of root water uptake III. Non-uniform transient combined salinity and water stress. *Agricultural Water Management*, 57, 127–144.

Homaee, M. & Schmidhalter, U. (2008). Water integration by plants root under non-uniform soil salinity. *Irrigation Science*, 27, 83–95.

Hoogland, J., Feddes, R., & Belmans, C. (1981). Root water uptake model depending on soil water pressure head and maximum extraction rate. *Acta Horticulturae*, 36, 119–123.

Jackson, R., Canadell, J., Ehleringer, J., Mooney, H., Sala, O., & Schulze, E. (1996). A global analysis of root distributions for terrestrial biomes. *Oecologia*, 108, 389–411.

Jarvis, P. (1976). The interpretation of the variations in leaf water potential and stomatal conductance found in canopies in the field. *Philosophical Transactions of the Royal Society of London. Series B, Biological Sciences*, 273, 593–610.

Katul, G., Ellsworth, D., & Lai, C. (2000). Modeling assimilation and intercellular CO2 from measured conductance: A synthesis of approaches. *Plant, Cell, and Environment*, 23, 1313–1328.

Katul, G., Manzoni, S., Palmroth, S., & Oren, R. (2010). A stomatal optimization theory to describe the effects of atmospheric CO_2 on leaf photosynthesis and transpiration. *Annals of Botany*, 105, 431–442.

Katul, G., Palmroth, S., & Oren, R. (2009). Leaf stomatal responses to vapour pressure deficit under current and CO2-enriched atmosphere explained by the economics of gas exchange. *Plant, Cell and Environment*, 32, 968–979.

Lagarias, J., Reeds, J. A., Wright, M., & Wright, P. (1998). Convergence properties of the nelder-mead simplex method in low dimensions. *SIAM Journal of Optimization*, 9, 1, 112–147.

Lai, C. & Katul, G. (2000). The dynamic role of root-water uptake in coupling potential to actual transpiration. *Advances in Water Resources*, 23, 247–439.

Laio, F. (2006). A vertically extended stochastic model of soil moisture in the root zone. *Water Resources Research*, 42, W02406,doi:10.1029/2005WR004502.

Laio, F., D'Odorico, P., & Ridolfi, L. (2006). An analytical model to relate the vertical root distribution to climate and soil properties. *Geophysical Research Letters*, 33(18), L18401, doi:10.1029/2006GL027331.

Larcher, W. (2003). *Physiological plant ecology - Ecophysiology and Stress Physiology of Functional Groups*. Berlin: Springer, 513 pp., 4th edn.

Lawlor, D. & Tezara, W. (2009). Causes of decreased photosynthetic rate and metabolic capacity in water-deficient leaf cells: a critical evaluation of mechanisms and integration of processes. *Annals of Botany*, 103, 561–579, doi:10.1093/aob/mcn244.

Lee, Z. P., Carder, K. L., Mobley, C. D., Steward, R. G., & Patch, J. S. (1998). Hyperspectral remote sensing for shallow waters: 1. A semianalytical model. *Applied Optics*, 37(27).

Lee, Z. P., Carder, K. L., Mobley, C. D., Steward, R. G., & Patch, J. S. (1999). Hyperspectral remote sensing for shallow waters: 2. Deriving bottom depths and water properties by ptimization. *Applied Optics*, 38(18).

Leuning, R. (1995). A critical-appraisal of a combined stomatal-photosynthesis model for C3 plants. *Plant, Cell and Environment*, 18, 339–355.

Li, K., Jong, R. D., & Boisvert, J. (2001). An exponential root-water-uptake

model with water stress compensation. *Journal of Hydrology*, 252, 189–204.

Li, R., Kaufman, Y., Gao, B., & Davis, C. (2003). Remote sensing of suspended sediments and shallow coastal waters. *IEEE Transaction on Geoscience and Remote Sensing*, 41(3), 559–566.

Lloyd, J. & Farquhar, G. (1994). ^{13}C discrimination during CO_2 assimilation by the terrestrial biosphere. *Oecologia*, 99, 201–215.

Longstreth, D., Bolaños, J., & Smith, J. (1984). Salinity effects on photosynthesis and growth in *Alternanthera philoxeroides* (mart.) griseb. *Plant Physiology*, 75(4), 1044–1047.

Loreto, F., Centritto, M., & Chartzoulakis, K. (2003). Photosynthetic limitations in olive cultivars with different sensitivity to salt stress. *Plant, Cell and Environment*, 26, 595–601.

Loreto, F., Harley, P., Marco, G. D., & Sharkey, T. (1992). Estimation of mesophyll conductance to CO_2 flux by three different methods. *Plant Physiology*, 98, 1437–1443.

Lunin, J. & Gallatin, M. (1965). Zonal salination of root in relation to plant growth. *Soil Science Society of America Proceedings*, 31, 608–612.

Maas, E. & Hoffman, G. (1977). Crop salt tolerance - current assessment. *ASCE Journal of the Irrigation and Drainage Division*, 103, 115–134.

Madsen, J., Chambers, P., James, W., Koch, E., & Westlake, D. (2001). The interaction between water movement, sediment dynamics and submersed macrophytes. *Hydrobiologia*, 444, 71–84.

Makela, A., Berninger, F., & Hari, P. (1996). Optimal control of gas exchange during drought: theoretical analysis. *Annals of Botany*, 77, 461–467.

Manzoni, S., Vico, G., Katul, G., Fay, P., Polley, W., Palmroth, S., & Porporato, A. (2011). Optimizing stomatal conductance for maximum carbon gain under water stress: a meta-analysis across plant functional types and climates. *Funtional Ecology*, 25(3), 456–467, doi: 10.1111/j.1365–2435.2010.01822.x.

Marani, M., D'Alpaos, A., Lanzoni, S., Carniello, L., & Rinaldo, A. (2007a). Biologically-controlled multiple equilibria of tidal landforms and the fate of the venice lagoon. *Geophysical Research Letters*, 34, L11402, doi:10.1029/2007GL030178.

Marani, M., D'Alpaos, A., Lanzoni, S., Carniello, L., & Rinaldo, A. (2007b). Biologically-controlled multiple equilibria of tidal landforms and the fate of the Venice lagoon. *Geophysical Research Letters*, 34(L11402).

Martini, P., Carniello, L., & Avanzi, C. (2004). Two dimensional modelling of flood flows and suspended sediment transport: the case of Brenta river, Veneto (Italy). *Natural Hazards and Earth System Sciences*, 4, 165–181.

MAV (2004). *Monitoraggio dell'Ecosistema Lagunare (MELa2) - 2° stralcio triennale. Linea A: "Rilievo delle fanerogame marine in Laguna di Venezia con taratura di un sistema di telerilevamento e completamento delle conoscenze sulle macroalghe". Rapporto di 2° anno sui risultati della mappatura*. Technical report, Consorzio Venezia Nuova. Esecutore SELC.

Melgar, J., Syvertsen, J., & García-Sánchez, F. (2008). Can elevated CO_2 improve salt tolerance in olive trees? *Journal of Plant Physiology*, 165, 631–640.

Mendel, M., Hergarten, S., & Neugebauer, H. (2002). On a better understanding of hydraulic lift: a numerical study. *Water Resource Research*, 38, 1183.

Mobley, C. D. (2004). *Light and water - Radiative transfer in natural waters*. CD Edition.

Molinaroli, E., Guerzoni, S., Sarretta, A., Masiol, M., & Pistolato, M. (2009). Thirty-year changes (1970 to 2000) in bathymetry and sediment texture recorded in the lagoon of Venice sub-basins, Italy. *Marine Geology*, 258, 115–125, doi:10.1016/j.margeo. 2008.12.001.

Montanari, A. (2007). What do we mean by 'uncertainty'? The need for a consistent wording about uncertainty assessment in hydrology. *Hydrological Processes*, 21, 841–845.

Mueller, J. L. & Austin, R. W. (1995). Ocean optics protocols for SeaWiFS validation, Revision 1. *NASA Goddard Space Flight Center, Greenbelt, MD, NASA Tech. Memo. TM-1995-104 566, ser. SeaWiFS Technical Report Series*, 25, 98–106.

Munns, R. (2002). Comparative physiology of salt and water stress. *Plant, Cell and Environment*, 25, 239–250.

Munns, R. & Tester, M. (2008). Mechanisms of salinity tolerance. *Annual Review of Plant Biology*, 59, 651–681.

Nicolas, M., Munns, R., Samarakoon, A., & Gifford, R. (1993). Elevated CO_2 improves the growth of wheat under salinity. *Australian Journal of Plant Physiology*, 20, 349–360.

Nishida, K. & Shiozawa, S. (2010). Modeling and experimental determination of salt accumulation induced by root water uptake. *Soil Science Society of America Journal*, 74, 774–786.

Nogués, S. & Baker, N. (2002). Effects of drought on photosynthesis in Mediterranean plants grown under enhanced UV-B radiation. *Journal of Experimental Botany*, 51(348), 1309–1317.

Novick, K., Stoy, P., Katul, G., Ellsworth, D., Siqueira, M., J.Juang, & Oren, R. (2004). Carbon dioxide and water vapor exchange in a warm temperate grassland. *Oecologia*, 138, 259–274.

Old, G., Leeks, G., Cooper, D., McNeil, D., & Smith, P. (2001). *Two technological advances in continuous monitoring of suspended sediment transport and particle characteristics.* Technical report, Centre for Ecology and Hydrology, Maclean Building, Crowmarsh Gifford, Wallingford, Oxon, OX10 8BB, UK.

Östlund, C., Flinka, P., Strömbeck, N., Pierson, D., & Lindell, T. (2001). Mapping of the water quality of Lake Erken, Sweden, from Imaging Spectrometry and Landsat Thematic Mapper. *The Science of the Total Environment*, 268, 139–154.

Paranychianakisa, N. & Chartzoulakisb, K. (2005). Irrigation of mediterranean crops with saline water: from physiology to management practices. *Agriculture, Ecosystems and Environment*, 106, 171–187.

Parida, A., Das, A., & Mittra, B. (2003). Effects of nacl stress on the structure, pigment complex composition, and photosynthetic activity of mangrove *Bruguiera parviflora* chloroplasts. *Photosynthetica*, 41(2), 191–200.

Parida, A., Das, A., & Mittra, B. (2004). Effects of salt on growth, ion accumulation, photosynthesis and leaf anatomy of the mangrove, *Bruguiera parviflora*. *Trees*, 18, 167–174.

Perillo, G., Wolanski, E., Cahoon, D., & Brinson, M. (2009). *Coastal Wetlands.* Elsevier (Ed.).

Petzold, T. (1972). Volume scattering coefficients for selected oceanic waters. In J. E. Tyler (Ed.), *Light in the Sea* (pp. 150–174). Dowden and Hutchinson and Ross, Stroudsberg.

Pope, R. & Fry, E. (1997). Absorption spectrum (380-700 nm) of pure water. II. Integrating cavity measurements. *Applied Optics*, 36, 8710–8723.

Porporato, A., Daly, E., & Rodriguez-Iturbe, I. (2004). Soil water balance and ecosystem response to climate change. *The American Naturalist*, 164(5), 625–632.

Porporato, A., Laio, F., Ridolfi, L., , & Rodriguez-Iturbe, I. (2001). Plants in water-controlled ecosystems: Active role in hydrologic processes and response to water stress: III. Vegetation water stress. *Advances in Water Resources*, 24(7), 725–744.

Pritchard, D. & Hogg, A. (2003). Cross-shore sediment transport and the equilibrium morphology of mudflats under tidal currents. *Journal of Geophysical Research - Oceans*, 108(3313 DOI: 10.1029/2002JC001570).

Richards, J. & Caldwell, M. (1987). Hydraulic lift: substantial nocturnal water transport between soil layers by artemisia tridentata roots. *Oecologia*, 73, 486–489.

Richter, R. (2009). *Atmospheric/topographic correction for satellite imagery: ATCOR-2/3 User Guide.* Technical report, DLR - German Aerospace Center - Remote Sensing Data Center, D- 82234 Wessling, Germany DLR-IB 565-01/09.

Rodriguez-Iturbe, I. & Porporato, A. (2005). Ecohydrology of water-controlled ecosystems. *Cambridge Univ. Press, New York.*

Rodriguez-Iturbe, I., Porporato, A., Laio, F., , & Ridolfi, L. (2001). Plants in water-controlled ecosystems: Active role in hydrologic processes and response to water stress: I. scope and general outline. *Advances in Water Resources*, 24(7), 695–705.

Runyan, C. & D'Odorico, P. (2010). Ecohydrological feedbacks between salt accumulation and vegetation dynamics: Role of vegetation-groundwater interactions. *Water Resources Research*, 46, W11561, doi:10.1029/2010WR009464.

Schenk, H. & Jackson, R. (2002). The global biogeography of roots. *Ecological Monographs*, 72(3), 311–328.

Schnarrenberger, C., Groβ, D., Burkhard, C., & Herbert, M. (1980). Cell organdies from Crassulacean Acid Metabolism (CAM) plants II. Compartmentation of enzymes of the Crassulacean Acid Metabolism. *Planta*, 147, 477–484.

Seemann, J. & Sharkey, T. (1986). Salinity and nitrogen effects on photosynthesis, ribulose-1,5-bisphosphate carboxylase and metabolite pool size in *Phaseolus vulgaris L. Plant Physiology*, 82, 555–560.

Siqueira, M., Katul, G., & Porporato, A. (2008). Onset of water stress, hysteresis in plant conductance, and hydraulic lift: Scaling soil water dynamics from millimeters to meters. *Water Resources Research*, 44, W01432, doi:10.1029/2007WR006094.

Siqueira, M., Katul, G., & Porporato, A. (2009). Soil moisture feedbacks on convection triggers: the role of soil-plant hydrodynamics. *Journal of Hydrometeorology*, 10, 96–112.

Skaggs, T., VanGenuchten, M., Shouse, P., & Poss, J. (2006). Macroscopic approaches to root water uptake as a function of water and salinity stress. *Agricultural Water Management*, 86, 140–149.

Sperry, J., Adler, F., Campbell, G., & Comstock, J. (1998). Limitation of plant water use by rhizosphere and xylem conductance: results from a model. *Plant, Cell and Environment*, 21, 347–359.

Tambroni, N. & Seminara, G. (2006). Are inlets responsible for the morphological degradation of venice lagoon? *Journal of Geophysical Research*, 111, F03013, doi:10.1029/2005 JF000334.

Tyree, M. (2003). Hydraulic properties of roots. *Ecological Studies*, 168, 125–150.

VanGenuchten, M. (1987). A numerical model for water and solute movement in and below the root zone. *Research Report, U.S. Salinity Laboratory, USDA, ARS, Riverside, CA*.

Varado, N., Braud, I., & Ross, P. (2006). Development and assessment of an efficient vadose zone module solving the 1D Richards equation and including root extraction by plants. *Journal of Hydrology*, 323, 258–275.

Vico, G. & Porporato, A. (2008). Modelling C3 and C4 photosynthesis under water-stressed conditions. *Plant Soil*, 313, 187–203, DOI 10.1007/s11104–008–9691–4.

Volpe, V., Carniello, L., Defina, A., Marani, M., D'Alpaos, A., & Silvestri, S. (2011a). Remote sensing and modelling of suspended sediment concentration in shallow tidal areas. *River, Coastal and Estuarine Morphodynamics: RCEM2011*.

Volpe, V., Manzoni, S., Marani, M., & Katul, G. (2011b). Leaf conductance and carbon gain under salt stressed conditions. *Journal of Geophysical Research*, 116, G04035,, doi:10.1029/2011JG001848.

Volpe, V., Silvestri, S., & Marani, M. (2011c). Remote sensing retrieval of suspended sediment concentration in shallow waters. *Remote Sensing of Environment*, 115, 44–54.

Wilks, D. (2006). International geophysics series. In A. Press (Ed.), *Statistical Methods in the Atmospheric Sciences* (pp. 215–217). Elsevier.

Wullschleger, S. (1993). Biochemical limitations to carbon assimilation in C_3 plants - A retrospective analysis of the A/C_i curves from 109 species. *Journal of Experimental Botany*, 44(262), 907–920.

Yamori, W., Noguchi, K., & Terashima, I. (2005). Temperature acclimation of photosynthesis in spinach leaves: analyses of photosynthetic components and temperature dependencies of photosynthetic partial reactions. *Plant, Cell and Environment*, 28, 536–547.

Yeo, A., Caporn, S., & Flowers, T. (1985). The effect of salinity upon photosynthesis in rice (*Oryza sativa L.*): Gas exchange by individual leaves in relation to their salt content *Phaseolus vulgaris L. Journal of Experimental Botany*, 36, 1240–1248.

Zhang, Y., Pulliainen, J., Koponen, S., & Hallikainen, M. (2002). Application of an empirical neural network to surface water quality estimation in the Gulf of Finland using combined optical data and microwave data. *Remote Sensing of Environment*, 81, 327–336.

Zibordi, G., Mélin, F., Hooker, S. B., D'Alimonte, D., & Holben, B. (2004). An autonomous above-water system for the validation of ocean color radiance data. *IEEE Transactions on Geoscience and Remote Sensing*, 42(2), 98–106.

Zwolak, J., Boggs, P., & Watson, L. (2007). Algorithm 869: ODRPACK95: A Weighted Orthogonal Distance Regression Code with Bound Constraints. *ACM Transactions on Mathematical Software*, 33(4), Article 27.